Analytic and Numerical Study of Current-Driven Drift Waves and Microturbulence in Fusion Energy Devices

PPPL
PRINCETON
PLASMA PHYSICS
LABORATORY

Nadine Maria Kremer

Ulm University

ulm university universität ulm

A thesis submitted for the degree of
Diplom-Physikerin, Diplom-Wirtschaftsphysikerin

Advisor: Prof. G. W. Hammett

January 2012

1. Reviewer: Prof. Frank Jenko

2. Reviewer: Prof. Joachim Ankerhold

Abstract

Within this thesis, the impact of current-driven drift waves and microturbulence in fusion energy devices is studied. The analytic study is based on a model that contains fluid ions and a simplified kinetic description of electrons.

To examine numerically the impact of an electron current on drift waves, a program was written in Mathematica. It provides the calculation of the real and imaginary parts of the drift wave frequency and the diffusion, based on the mixing length approximation. The model used to describe the drift waves considers a plane plasma slab geometry and contains kinetic ions, kinetic electrons and an additional ion polarization term. The plasma dispersion function is approximated by a four-pole approximation. After the discussion of the functionality of the program, numerical studies of growth rates, frequencies and diffusion are provided.

The prediction, based on the analytic study of the destabilizing influence of an electron current on drift waves, is verified by numerical results. The diffusion generated by the current-driven drift wave, is predicted by this model to be potentially significant in some parameter regimes relevant to the Alcator C-Mod experiment, leading to the suggestion that current-driven drift waves should be included in full gyrokinetic codes.

Zusammenfassung

Im Rahmen der vorliegenden Arbeit wird der Einfluss von stromgetriebenen Driftwellen (CDDWs) und Mikroturbulenzen in Fusionsanlagen untersucht. Die analytische Untersuchung basiert auf einem Modell, das Ionen als kalte Flüssigkeit und Elektronen kinetisch beschreibt.

Um den Einfluss eines parallelen Elektronenstroms auf Driftwellen numerisch zu untersuchen, wurde ein auf Mathematica basierendes Programm entwickelt, das die Berechnung von Real- und Imaginärteil der Frequenz, wie auch der Diffusion erlaubt. Das der numerischen Betrachtung zugrunde liegende Modell basiert auf kinetischen Ionen und kinetischen Elektronen, ergänzt durch einen Term, der die Polarisationsdrift der Ionen berücksichtigt. Die Plasmadispersionsfunktion wird durch eine Vierpolnäherung beschrieben.

Die auf der analytischen Untersuchung basierende Vorhersage der destabilisierenden Wirkung eines Elektronenstroms auf Driftwellen konnte im Rahmen der numerischen Analyse bestätigt werden. Die durch CDDWs verursachte Diffusion ist möglicherweise in einigen für das Alcator C-Mod-Experiment relevanten Parameterbereichen von Bedeutung. Daher wird empfohlen, CDDWs zur weiteren Analyse in gyrokinetische Codes zu integrieren.

Contents

List of Tables

List of Figures

Listings

Acronyms

CDDW current-driven drift wave.

ETG electron temperaturere gradient.

FLR finite Larmor radius.

ITG ion temperature gradient.

MHD magnetohydrodynamic.

NSTX national spherical torus experiment.

PDF probability density function.

SOL scape-off-layer.

TEM trapped electron mode.

1

Introduction

Considering matter as conglomerate of neutral atoms and molecules, there are three common states: solid, fluid and gaseous. Dependent on pressure and temperature, matter cross over from one state to another. Increasing the temperature in the gaseous state results finally in an ionization of the gas molecules. This state is essentially affected by the long-range Coulomb forces between the charged particles, while the ionized gas is neutral in sum.

Beside the usual collision processes, collective phenomena arise causing new interesting effects. This special state was first called a “plasma” by Langmuir in 1928 as he wrote “we shall use the name plasma to describe this region containing balanced charges of ions and electrons” [30]. Plasma is also labeled as the fourth state of matter, following the named three states, while simultaneously stressing the fundamental new characteristics of plasma.

Besides the wide actual application spectrum, for example in material science for surface treatment, plasma is our great hope for solving the future energy problems of the earth.

1.1 Fusion

The sun is the archetype of all fusion energy devices that try to mimic the sun's power on earth. The source of the sun's energy, which provides all life on earth, is fusion: Combining of lighter elements into heavier ones, while setting free energy. In the sun the proton-proton cycle dominates:

$$\begin{aligned} H_1^1 + \ H_1^1 &\rightarrow \ H_1^2 + e^+ + \nu_e \ , \\ H_1^2 + \ H_1^1 &\rightarrow \ He_2^3 + \gamma \ , \\ He_2^3 + \ He_2^3 &\rightarrow \ He_2^4 + 2H_1^1 \ . \end{aligned}$$

Hydrogen is burned into helium [40]. Since the mass balance is broken in these reactions, the mass converts to energy according to

$$E = mc^2 \ . \tag{1.1}$$

Equation 1.1 states the equivalence of mass m and energy E. The proportionality factor $c \approx 3 \cdot 10^8 m/s$ is the speed of light. As c^2 is a high number, a small amount of mass contains huge energy. The difference between the sum of all masses of the nucleons and the actual smaller mass of the atom nucleus is the mass deficit, connected with the binding energy through the Einstein-relation (1.1).

Figure 1.1 shows the binding energy per nucleon versus the atomic mass number. The maximal binding energy is reached at the atomic mass number of 56, which is iron. For heavier nuclides the energy sinks, caused by the increasing amount of protons and their rejecting Coulomb force. For all nuclides lighter than iron, the strong interaction outweighs the Coulomb force. Thus there are two ways of gaining energy through nuclear power: fission of heavier nucleus and fusion of lighter ones.

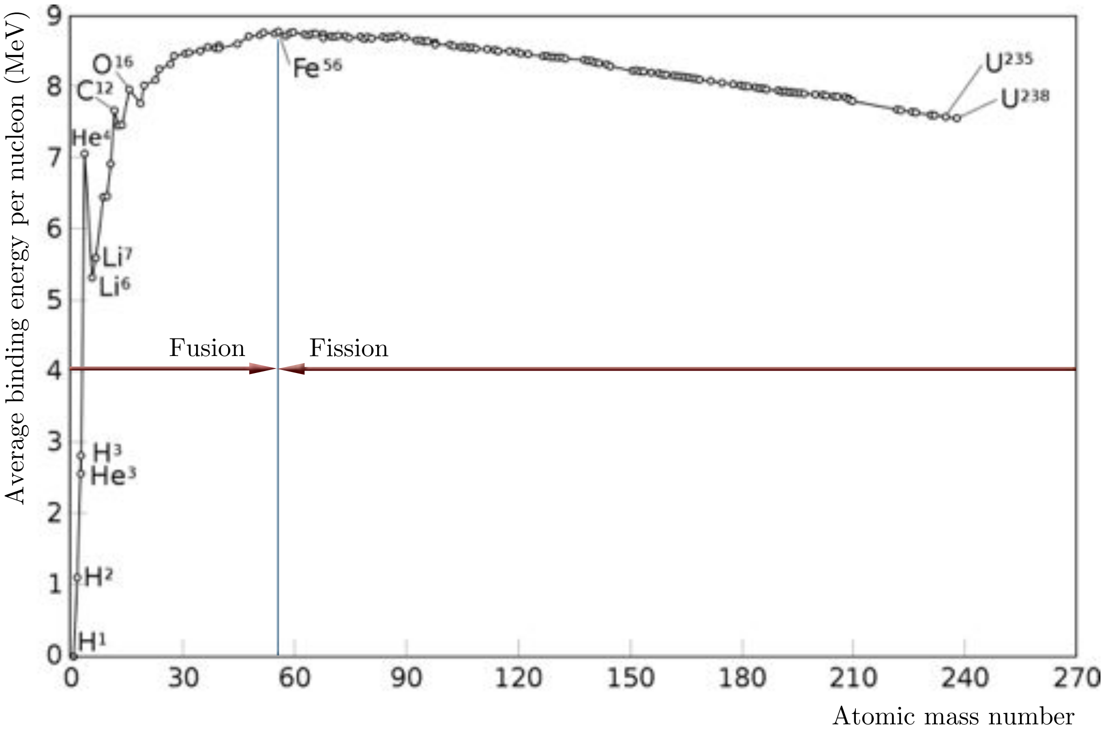

Figure 1.1: Binding energy curve - Average binding energy versus atomic mass number. Energy can be gained by fission of heavier nuclei or fusion of lighter ones, whereas the maximum binding energy is reached for iron. Data from [37].

For terrestrial applications, the fusion of two isotopes of hydrogen H_1^1, deuterium ($D = H_1^2$) with tritium ($T = H_1^3$), is promising, producing $17.6 MeV$ of energy

$$D + T \rightarrow {}^4He + n \qquad\qquad (\Delta E = 17.6 MeV) \ .$$

The energy ΔE is distributed between the α-particle, ${}^4He$, with $3.5 MeV$ and the neutron. Both deuterium and tritium can be gained easily in most places on earth. Deuterium is part of every hydrogen-compound and hence, as an easily extractable part of sea water, a virtually infinite source of energy. Tritium is radioactive (β-emitter) with a half-life of 12.5 years. It can be produced out of lithium with the help of neutrons via the following process, supplemented by neutron multipliers like beryllium or lead:

$$\begin{aligned} n + {}^6Li &\rightarrow T + {}^4He && (\Delta E = 4.78 MeV) \ , \\ n + {}^7Li &\rightarrow T + {}^4He + n && (\Delta E = -2.47 MeV) \ . \end{aligned} \tag{1.2}$$

As the first reaction has a large cross section for slow and the second for fast neutrons, these reactions can be achieved in a lithium blanket in a fusion energy supply as illustrated in figure 1.2. Lithium is a wide-spread resource, found in the earth's crust and sea water. Thus with the second ingredient breeding on site, this kind of energy source, assuming the needed technical knowledge, may be used world wide without the need of importing expensive resources for permanent operation [44].

For most experimental fusion devices, another reaction is used:

$$\begin{aligned} D + D &\rightarrow T + H && (\Delta E = 4 MeV) \ , \\ D + D &\rightarrow {}^3He + n && (\Delta E = 3.25 MeV) \ . \end{aligned}$$

No tritium has to be generated for this reaction, which has two huge advantages for testing purposes. First, without tritium there are fewer radioactive materials, allowing technicians to make adjustments of the inner parts without risking their health. The second advantage are the lower costs, tritium is expensive compared to deuterium, and cannot be bred by experimental devices at present.

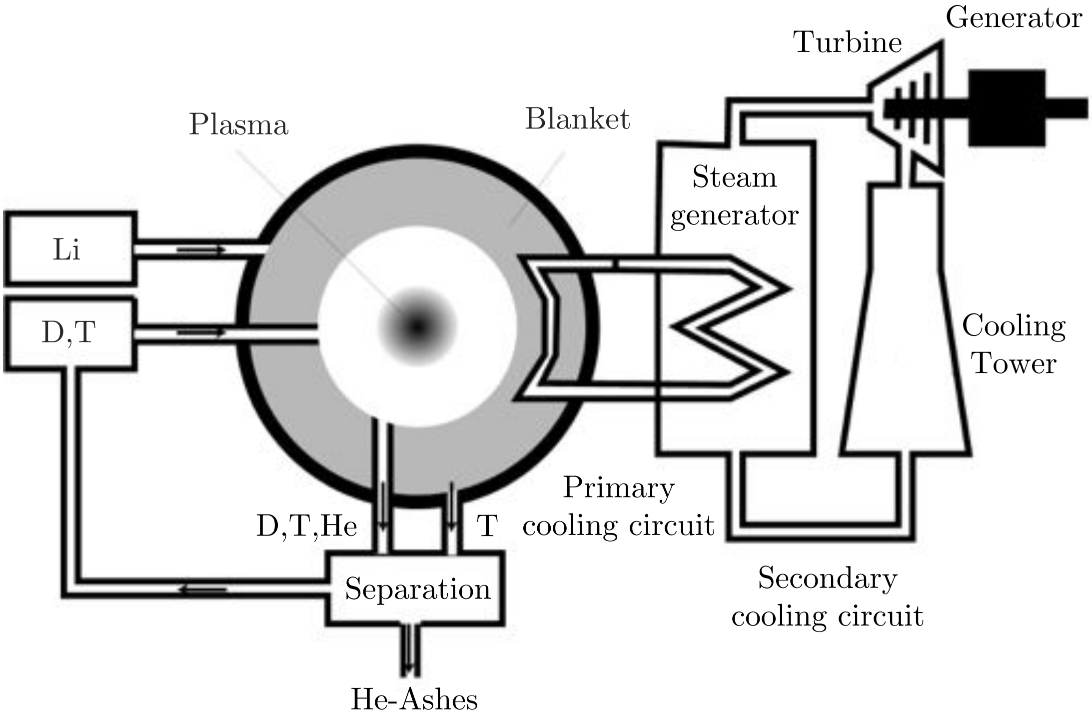

Figure 1.2: Fusion power plant - deuterium and tritium are filled into the reactor and fuse to α-particles and neutrons. The generated neutrons produce new tritium in the lithium blanket. The resulting heat drives a turbine, which generates power (taken from Ref. [11]).

Figure 1.2 shows a prototype of a fusion reactor. Deuterium and tritium are fed into the plasma chamber, where they fuse. The generated α-particles heat the plasma and the neutrons escape to the walls, where they react with the lithium to tritium according to (1.2) or being decelerated by the walls. The produced heat is led away, driving a turbine and thus producing power.

There are different concepts for how to prevent the hot plasma from hitting the wall, amongst others magnetic and inertial confinement. The plasma chamber for inertial confinement is the reaction chamber, while for magnetic confinement, it is for example the tokamak (see section 2.5.1).

1.1.1 Lawson Criterion

Fusion research is aimed at producing a plasma, generating more energy than needed to create and maintain it. The quantity $Q = P_{Fusion}/P_{ext}$, the ratio of the power contained in fusion products to the power needed to heat the plasma, measures the fusion performance of a power plant. $Q = 1$ is called the break-even, the moment that more energy is gained than invested. Ignition corresponds to $Q = \infty$ and a plasma burns for about $Q > 5$. While for an efficient power plant at least $Q \sim 15$ is necessary, for ITER $Q > 10$ is intended.

Lawson's original paper [31] considers both an ignition criterion for a steady state system and a simpler engineering net gain criterion for a driven cyclical system. According to the last-mentioned, a net energy is gained, if

$$\eta(R + 1) > 1,$$

where $R = E_{out}/E_{in}$ and η is the efficiency of transformation of the energy, released from the reaction into heating of the walls, further to electrical, mechanical or chemical energy. For a driven cyclical system,

$$R = \frac{\tau P_R}{\tau P_B + 3nkT} \ ,$$

with the fusion reaction power P_R and the radiated power per unit volume P_B. R is a function of the temperature T, density n and the confinement time τ. [31]

These are the three critical quantities to be optimized. The temperature T has to be high enough for fusion to take place, which for a deuterium-tritium plasma is about $10 - 30$ keV. Assuming $\eta = 1/3$, the original guess of Lawson,

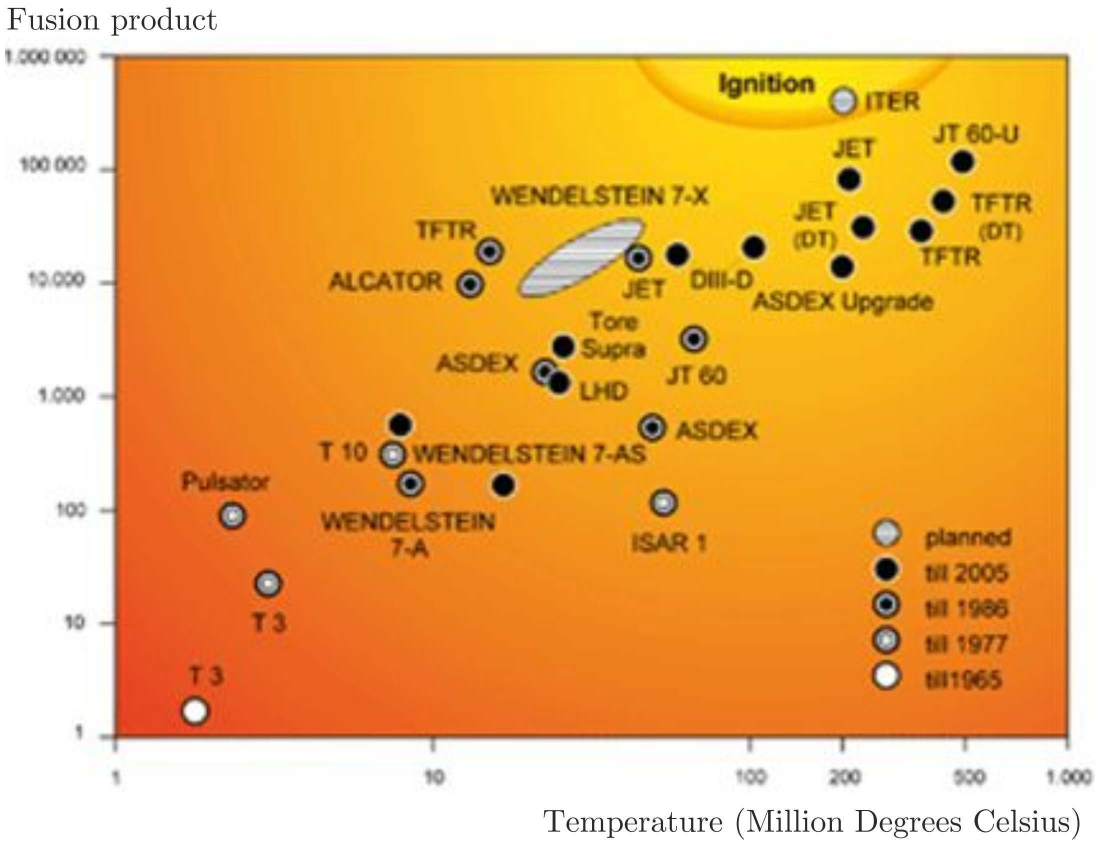

Figure 1.3: Fusion product - This figure shows the progress made in fusion research. While JET is closest to the ignition condition at this time, ITER is believed to operate slightly beyond the threshold of ignition (taken from Ref. [35]).

power is gained for $n\tau_E > 10^{20}\mathrm{m}^{-3}$. [4]

For a typical plasma density of 10^{20} m^{-3} and a confinement time of $1 - 2$ s a surplus of energy is possible. There are more modern ways of determining the optimal values of confinement time, density and temperature, the triple product $nT\tau_E$. Again calculated for a deuterium-tritium plasma the triple product becomes $nT\tau_E > 10^{21}$ keV s/m^{-3}. Figure 1.3 illustrates the triple product, also called fusion product. The minimum of the fusion product is also sometimes called the Lawson criterion.

1.1.2 Inertial Fusion Energy

As pointed out in the last section, the plasma has to be trapped long enough with a high enough pressure to ensure sufficient fusion reactions to produce energy. There are some ideas for realizing a long enough confinement time, using either inertial or magnetic confinement. Since this work is based on experiments in a tokamak, magnetic fusion will be explained in detail in section 2.

The principle for inertial fusion is to bring the density to a very high level, which allows a very short confinement time. The deuterium-tritium mixture is packed in a small pellet, which is compressed until explosion. The explosion time is actually the confinement time, however it is not anymore a confinement in a conventional meaning. The compression is done by either a laser or a particle beam. Due to Rayleigh-Taylor instabilities, a spherical irradiation is crucial.

There are two main principles for compression: via the direct or indirect drive. In direct drive, the laser hits the pellet directly, while in indirect drive the beams are first absorbed on the walls, which heat up, in order to irradiate the pellet more uniformly, as depicted in figure 1.4.

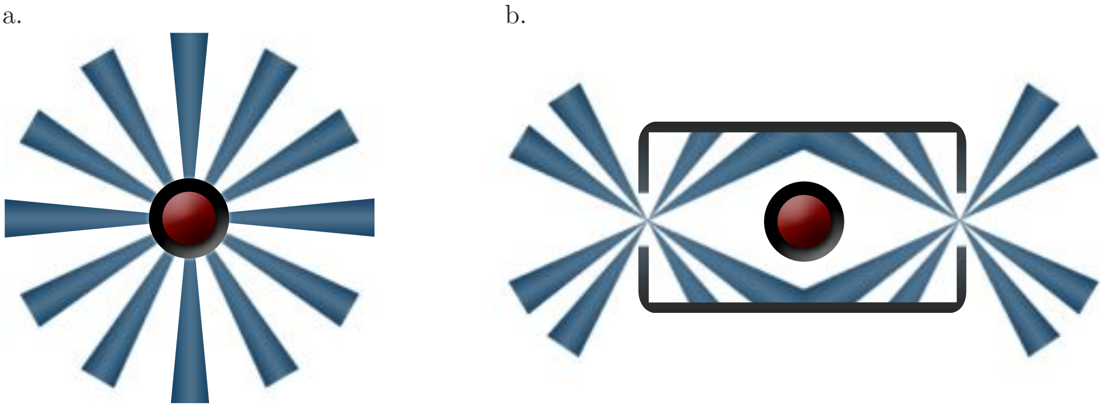

Figure 1.4: Inertia fusion - The laser (blue) is directed to the pellet (red, with black blanket). a. Direct drive: the laser hits the pellet directly. b. Indirect drive: the beams are first absorbed on the walls, which heat up in order to irradiate the pellet more uniformly (adapted from Ref. [10]).

1.2 Scope of the Project

This thesis was inspired by the work of L. Lin, M. Porkolab at al. In their 2009 paper titled, “Studies of turbulence and transport in Alcator C-Mod ohmic plasmas with phase contrast imaging and comparisons with gyrokinetic simulations” [33], turbulence and thermal transport in Alcator C-Mod ohmic plasmas were determined through numerical and experimental studies. A key question investigated in this paper is the change of plasma behavior between “Neo-Alcator” and “saturated ohmic” regime. “Neo-Alcator”, also called the “linear ohmic” regime, describes the range in which confinement time is proportional to the density, $\tau_E \propto \bar{n}_e$. An increase of the density leads to the saturated ohmic regime, in which the confinement time has a weak dependency of the density. As shown in figure 1.5 for the Alcator C-Mod case, for $\bar{n}_e < 0.7 \cdot 10^{20}\ m^{-3}$ there is a linear dependency and the confinement time is saturated for $\bar{n}_e > 0.8 \cdot 10^{20}\ m^{-3}$.

For high densities it was possible to show, that - as assumed - the instability is driven primarily by the ion temperature gradient (ITG). Turbulent wave propagation in the ion diamagnetic direction, as expected for ITG turbulence, was

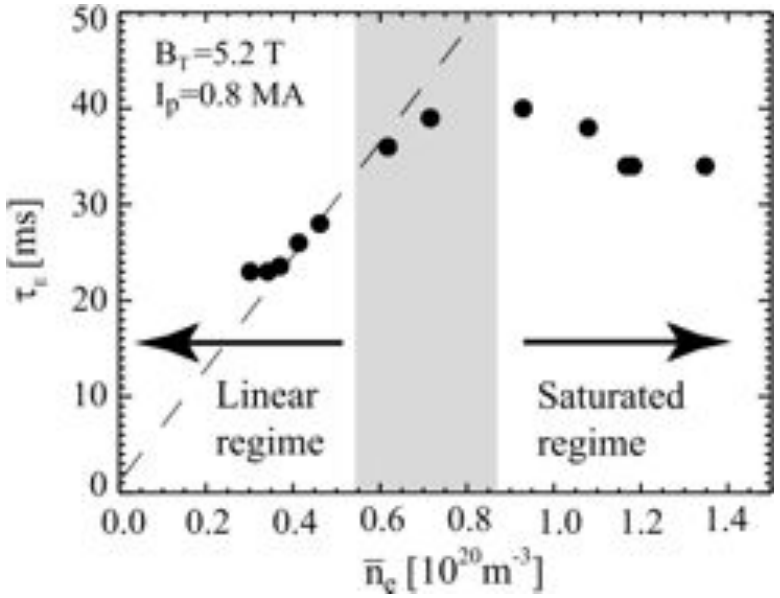

Figure 1.5: Linear and saturated ohmic regime and the transition-zone - The energy confinement time τ_E is plotted versus the line-average density $\bar{n}_e$ for Alcator C-Mod Parameter (taken from Ref. [33]).

also measured. In the saturated regime, the simulated predictions of GYRO fits within the experimental uncertainty to the experimental results, which is ±60% for the case of the absolute fluctuation wave number spectrum. For the thermal diffusivities for electrons, χ_e, ions, χ_i and the effective thermal diffusivity, $\chi_{eff} \sim (\chi_e + \chi_i)/2$, agreement could be reached after reduction of the normalized ion temperature gradient $a/L_{T,i}$ by 20%, which is as well within the experimental error. For the saturated regime, the predictions of GYRO are acceptable, though they found discrepancies in the linear regime.

In the linear regime, where the density is lower, the electron transport exceeds the transport of the ions, $\chi_e \gg \chi_i$, according to experimental results. Though GYRO simulations of long wavelength turbulence predicts $\chi_i > \chi_e$, the effective thermal diffusivity agrees with the experiments after reduction of the ITG by 20%. For the given parameters, trapped electron modes (TEMs) and electromagnetic effects could be excluded as source of the high electron transport.

As possible explanations, they suggested the possibility of influences of shorter wavelength turbulence (electron temperaturere gradient (ETG) turbulence), turbulent energy exchange or electron drift velocity. Simulations for short wavelength turbulence up to $k_y\rho_s \sim 4$ were done, so simulations with $k_y\rho_s > 4$ are required to perhaps explain the electron transport.

Another possible explanation could be the existence of electron drift velocity connected with "ohmic toroidal plasma current", which could drive electron drift waves. Since the electron drift velocity is very small in the standard gyrokinetic ordering, it is neglected in existing gyrokinetic turbulence codes. However, for the Alcator C-Mod experiments at low densities this drift velocity could be non-negligible compared to the electron thermal velocity and even exceed the ion sound speed [33]. This idea was the starting point for this thesis, which will evaluate the influence of the current-driven drift wave based on the described transport problem.

2

Magnetic Confinement Fusion

In this chapter the most basic concepts for plasma description will be introduced. Starting with the motion of single particles in magnetic fields and the resulting drifts, the kinetic model of plasmas is sketched. Coming from this microscopic picture, the fluid description of plasmas is outlined. All these concepts will play an important role in modeling drift wave behavior in chapter 3.

2.1 Single Particle Motion in Magnetic Fields

Consider the plasma as a conglomerate of negatively and positively charged particles, each moving with a different velocity $\mathbf{v}$ through a uniform magnetic field $\mathbf{B}$. Because of their charge, the Lorentz force (2.1) acts on each particle,

$$\mathbf{F}_L = q\left(\mathbf{E} + \frac{1}{c}\mathbf{v} \times \mathbf{B}\right) \ , \tag{2.1}$$

where c is the speed of light, q the charge and $\mathbf{v} = \mathit{const.}$ the velocity of the particle.

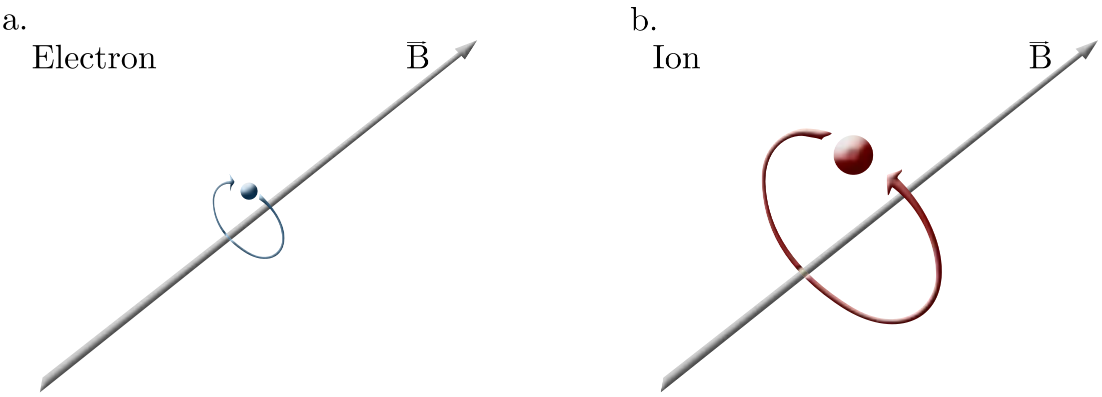

Figure 2.1: Gyration - Charged particles describe a circle around magnetic field lines due to the Lorentz force. The direction of the gyration depends on the charge. a. Gyration of negative charged particle, b. Gyration of positive charged particle.

Defining the coordinate system so that $\mathbf{B} = B\hat{\mathbf{z}}$, the force in absence of an electric field $\mathbf{E}$ becomes

$$\mathbf{F} = \frac{qB}{c}\begin{pmatrix} v_y \\ -v_x \\ 0 \end{pmatrix} . \tag{2.2}$$

The force $\mathbf{F}$ is purely perpendicular to the magnetic field. Differentiating the equation of motion $\mathbf{F} = m\mathbf{a} = m\dot{\mathbf{v}}$ with respect to time,

$$\ddot{\mathbf{v}} = \frac{qB}{mc}\begin{pmatrix} \dot{v}_y \\ -\dot{v}_x \\ 0 \end{pmatrix} ,$$

and inserting the original equations (2.2) gives

$$\ddot{\mathbf{v}}_\perp = -\left(\frac{qB}{mc}\right)^2 \mathbf{v}_\perp \ , \tag{2.3}$$

$$\ddot{v}_z = 0 \ ,$$

where $\mathbf{v}_\perp = v_x\hat{\mathbf{e}}_x + v_y\hat{\mathbf{e}}_y$. Because of the perpendicular nature of the force, the particle moves parallel to the magnetic field with constant velocity of $v_{z,0}$,

$$z(t) = z_0 + v_{z,0}t \ .$$

Equation (2.3) for the perpendicular velocity consists of two decoupled second order differential equations of the form $\ddot{\xi} = -\Omega^2\xi$. The solution is an oscillation with frequency Ω, $\xi(t) = A\cos(\Omega t) + B\sin(\Omega t)$. Comparing with (2.3), the frequency for the perpendicular motion is

$$\Omega_c = \frac{qB}{mc}$$

and the solutions for the perpendicular velocity components of (2.3) are

$$v_x(t) = v_{x1}\cos(\Omega_c t) + v_{x2}\sin(\Omega_c t) \ , \tag{2.4}$$

$$v_y(t) = v_{y1}\cos(\Omega_c t) + v_{y2}\sin(\Omega_c t) \ . \tag{2.5}$$

Consider $\dot{v}_x = \Omega_c v_y$ from (2.2), and insert the solution (2.4) for v_x, the velocity in y-direction becomes

$$v_y(t) = v_{x2}\cos(\Omega_c t) - v_{x1}\sin(\Omega_c t) \ .$$

This implies $v_{y1} = v_{x2}$ and $v_{y2} = -v_{x1}$. Assuming the initial conditions $\mathbf{v}(t = 0) = v_{x,0}\hat{\mathbf{x}} + v_{y,0}\hat{\mathbf{y}}$ and $\mathbf{x}(t = 0) = x_0\hat{\mathbf{x}} + y_0\hat{\mathbf{y}}$, (2.4) and (2.5) give the conditions $v_{x,0} = v_{x1}$ and $v_{y,0} = v_{y1}$. Integration of (2.4) and (2.5) with respect to time and using the boundary conditions, gives the equations of the particle's position in a straight magnetic field:

$$\begin{aligned}
x(t) &= x_0 + \frac{1}{\Omega_c}\left(v_{x,0}\sin(\Omega_c t) + v_{y,0}[1 - \cos(\Omega_c t)]\right) \ , \\
y(t) &= y_0 + \frac{1}{\Omega_c}\left(v_{y,0}\sin(\Omega_c t) - v_{x,0}[1 - \cos(\Omega_c t)]\right) \ , \\
z(t) &= z_0 + v_{z,0}t \ .
\end{aligned}$$

The so described particle propagates in a circle on the perpendicular plane around the magnetic field line, which is called the gyration motion, illustrated in figure 2.1. Due to the initial parallel velocity, these equations describe a helical motion as shown in figure 2.2. The magnetic field has no influence on the parallel motion.

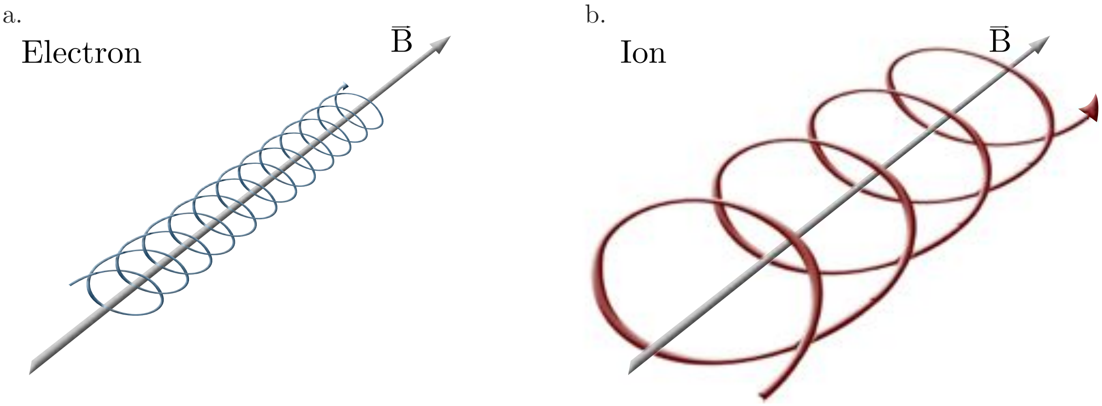

Figure 2.2: Helix - Charged particles with a velocity component parallel to the magnetic field propagate in form of a helix around the magnetic field.

The perpendicular velocity $v_\perp = \sqrt{v_{x,0}^2 + v_{y,0}^2}$ together with the strength of the magnetic field determine the radius of the gyration, also called gyro- or Larmor-radius

$$\rho_L = \frac{v_\perp}{\Omega_c} \ . \tag{2.6}$$

The oscillation frequency Ω_c is also called the gyro-frequency. Ions and electrons gyrate in opposite directions due to the charge dependency of Ω_c. Electrons describe a right-hand screw, while ions propagate left-handedly. For a deuterium plasma the mass ratio between electrons and ions is $\frac{m_i}{m_e} \sim 3669$. Since $\Omega_c \sim 1/m$, the electrons gyrate much faster than the ions with $\Omega_{c,e} \sim 3669\Omega_{c,i}$ and the electrons' gyro-radius is small compared to the ions', $\rho_e \sim \rho_i/60$. In addition, the dependency on charge and mass increases Ω_c linearly with the magnetic field, which results in a decrease of the radius.

In many cases it is convenient to describe the particle motion as a superposition of the motion of the center of the gyration, the guiding center, and the gyration around it. Neglecting the fast electron gyration for example clarifies the physics behind the guiding center drifts. The drift kinetic theory takes advantage of this. This guiding center drift depends on the characteristics of the particle: charge, mass and energy, but also on external factors such as gradients or additional fields. In the next section some important particle drifts for the understanding of drift waves are described in detail.

2.2 Particle Drifts

Ions and electrons as charged particles experience forces in electric and magnetic fields. In this chapter the most important particle drifts for understanding the drift wave, covered in section 3.1, will be introduced. All drifts covered here are valid in the lowest order of the ratio of gyroradius to the background variation scale.

2.2.1 $\mathbf{E} \times \mathbf{B}$ - Drift

In presence of an additional field causing the force $\mathbf{F}_{ext}$, the particle drifts perpendicular to that field and the magnetic field with the drift velocity

$$\mathbf{v}_D = \frac{c}{q} \frac{\mathbf{F}_{ext} \times \mathbf{B}}{B^2} \ . \tag{2.7}$$

To derive (2.7), one starts with the equation of motion,

$$m\dot{\mathbf{v}} = \frac{q}{c}\mathbf{v} \times \mathbf{B} + \mathbf{F}_{ext} \ ,$$

and defines with $\mathbf{B} = B\hat{\mathbf{b}}$

$$\mathbf{u} \equiv \mathbf{v} - \frac{c}{qB}\mathbf{F}_{ext} \times \hat{\mathbf{b}} \ .$$

Since $\dot{\mathbf{u}} = \dot{\mathbf{v}}$,

$$\begin{aligned} m\dot{\mathbf{u}} =& \mathbf{F}_{ext} + \frac{qB}{c}\mathbf{u} \times \hat{\mathbf{b}} + (\mathbf{F}_{ext} \times \hat{\mathbf{b}}) \times \hat{\mathbf{b}} \\ =& \frac{qB}{c}\mathbf{u} \times \hat{\mathbf{b}} + (\hat{\mathbf{b}} \cdot \mathbf{F}_{ext})\hat{\mathbf{b}} \ , \end{aligned}$$

resulting in a velocity perpendicular and parallel to the magnetic field. Shifting back to the original frame, the drift velocity (2.7) is gained.

All particle drifts described below may be considered special cases of this force's drift. Assume the force in (2.7) originates from an electric field with the corresponding force

$$\mathbf{F}_e = q\mathbf{E} \ .$$

As shown in figure 2.3 a. the magnetic field remains pointing in $\hat{z}$-direction and the electric field points in $\hat{x}$-direction. In a purely **B**-field, a single positively charged ion will gyrate around the magnetic field line describing a concentric circle around the origin. An additional electric field causes an acceleration of the ion along **E**.

Simplifying the circle into a square with sides parallel to the axes, the ion is accelerated while moving in positive $\hat{\mathbf{x}}$-direction, and decelerated in the reverse **E**-direction. These acceleration and deceleration result in different velocities and thus the gyration radius (2.6) is greater on one half of the circle than on the other, as depicted in figure 2.3 a. Thus the electric field combined with the magnetic field causes a perpendicular net drift of the ions, as depicted in figure 2.3 b.

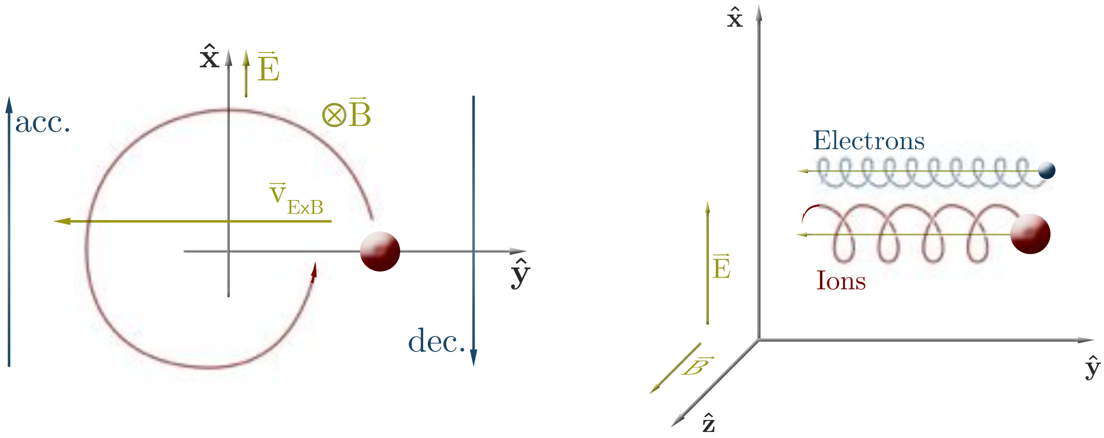

Figure 2.3: E × B - drift - An electric field perpendicular to the magnetic field causes a charge-independent perpendicular drift. a. The ion is accelerated parallel to **E** and decelerated antiparallel, resulting in a greater radius on the upper half-circle and a reduced radius on the lower side. This leads to an **E** × **B** - drift in $-\hat{\mathbf{y}}$ - direction (b.).

The **E** × **B** - drift velocity becomes

$$\mathbf{v}_E = \frac{c}{B}\mathbf{E} \times \hat{\mathbf{b}} \ .$$

This drift is independent of the particles' charge, ions and electrons drift in the same direction with the identical velocity, thus the net current is zero.

2.2.2 Polarization - Drift

In all real devices, for many reasons, time-varying electric fields are present, which cause additional effects. In section 2.2.1 it is described how the acceleration and deceleration of the particle parallel and antiparallel to the electric field with $|a_{acc}| = |a_{dec}|$ causes the **E** × **B** - drift. Assuming a time-dependent electric field, the absolute values of the acceleration and deceleration differs, $|a_{acc}| \neq |a_{dec}|$. Thus an additional drift component in the direction of the time variation of the electric field arises,

$$\mathbf{v}_p = \frac{c}{B}\frac{1}{\Omega_c} d_t \mathbf{E} \ . \tag{2.8}$$

This drift velocity is inversely proportional to the gyration frequency Ω_c and thus dependent on mass and charge of the particle. Negative electrons drift in the opposite direction of positive ions, causing a separation of charge. Therefore this drift is called “polarization drift” causing a net current. Expressing the polarization drift (2.8) in form of the $\mathbf{E} \times \mathbf{B}$ - drift points out the differences in the magnitude:

$$\mathbf{v}_p = \frac{c}{B}\frac{1}{\Omega_c} d_t \mathbf{E} = \frac{1}{\Omega_c} \hat{\mathbf{b}} \times d_t \mathbf{v}_E \ . \tag{2.9}$$

Since $v_p \sim \frac{\omega}{\Omega_c} v_E$, the polarization drift is second order of $1/\Omega_c$ and small compared to the $\mathbf{E} \times \mathbf{B}$ - drift. For electrons usually this drift may be neglected since $\mathbf{v}_p \sim \frac{1}{\Omega_c}$.

2.2.3 Diamagnetic Velocity

In contrast to the previously discussed drifts, the diamagnetic velocity is actually no gyrocenter drift. However, in some literature it is called “diamagnetic drift”. As depicted in figure 2.4, an inhomogeneous distribution of guiding centers caused by a density gradient produces a net electric current through superposition of the ring currents. Assuming a temperature gradient instead of a density gradient, the particles’ gyroradius $\rho \approx \sqrt{T}$ is changed, causing the same effect as a density gradient. Thus in general the diamagnetic velocity is caused by the pressure gradient $\nabla p = \nabla(nT)$. The name “diamagnetic velocity” originates from the fact that the diamagnetic current

$$\mathbf{j}_* = -\frac{c}{B} \nabla p \times \hat{\mathbf{b}}$$

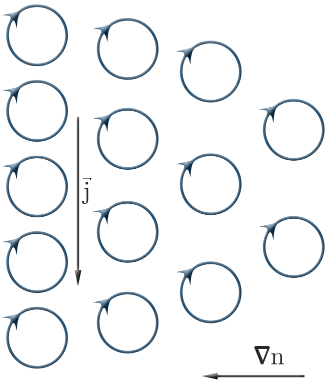

Figure 2.4: Diamagnetic velocity - A density gradient produces a diamagnetic current **j**.

generally reduces the magnetic field inside the plasma. The diamagnetic velocity for a straight magnetic field in the **ẑ**-direction with a constant temperature T and density gradient in the **x̂**-direction becomes

$$\mathbf{v}_* = \frac{cT}{qB}\frac{d_x n}{n}\hat{\mathbf{y}} \ . \tag{2.10}$$

In the following sections equation 2.10 with $q = -e$ is denoted as the "electron diamagnetic velocity," v_{de}.

2.2.4 Drifts in non-uniform magnetic fields

Besides the covered $\mathbf{E} \times \mathbf{B}$ - and polarization-drifts, there are other drifts that generally influence the way particles move in fusion devices. Above, the magnetic field was assumed to be temporally and spatially constant and straight in $\hat{z}$-direction. Similar to the way the time-varying electric field caused polarization drift, a softening of these restrictions on the magnetic field results in additional drifts. The ∇B-drift arises due to a gradient in the magnetic field strength, while a curvature of $\mathbf{B}$ results in the so-called curvature drift. Assuming a magnetic field, characterized by both gradient and curvature, the resulting particle drift becomes [3, 20]

$$\mathbf{v} = \mathbf{v}_c + \mathbf{v}_{\nabla B} = \frac{cmv_\parallel^2}{qB^2}\frac{\mathbf{R}_c \times \mathbf{B}}{R_c^2} + \frac{cv_\perp^2}{2\Omega_c}\frac{\mathbf{B} \times \nabla B}{B^3} \, .$$

$\mathbf{R}_c = -((\hat{\mathbf{b}} \cdot \nabla)\hat{\mathbf{b}})/(|(\hat{\mathbf{b}} \cdot \nabla)\hat{\mathbf{b}}|^2)$ is the vector radius of the curvature as illustrated in figure 2.5 a. It is defined to be perpendicular to $\hat{\mathbf{b}}$.

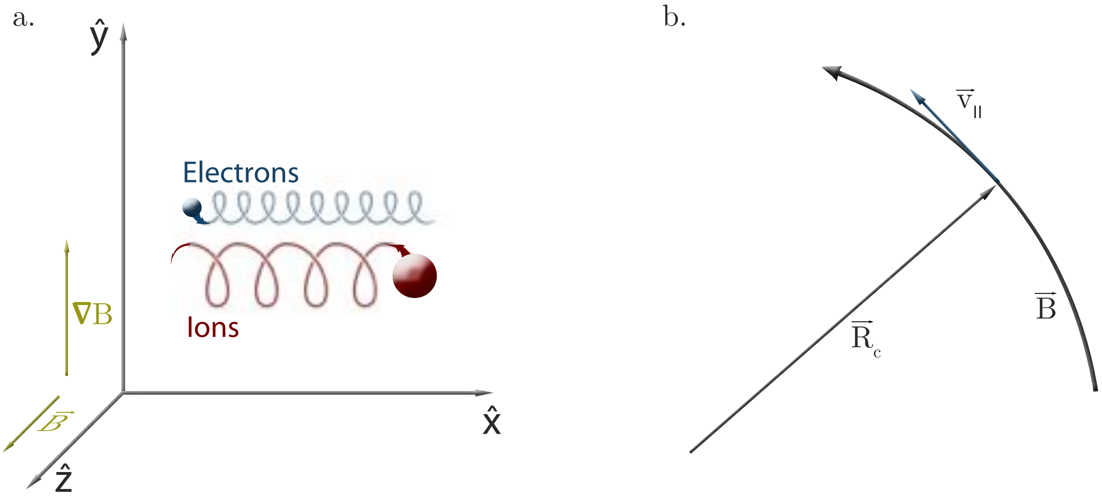

Figure 2.5: ∇B and curvature drift - a. A gradient in the magnetic field causes a drift with direction depending on the particle's charge. b. Definition of the curvature vector $\mathbf{R}_c$.

After illustrating some of the most important particle drifts, the next sections discuss concepts of plasma descriptions that avoid calculating equations of motion for each single particle.

2.3 Microscopic Picture - The Kinetic Theory

In the last chapter the motion of a single particle in a given external field was considered, neglecting the influence of the particle on the field. Since there are many particles in a plasma, each of them giving rise to currents and space charges, which influence the fields, a single particle description is impractical. Additionally the impact of thermal motion leading to collisions has to be taken into account.

There are different approaches to describing a plasma as a superposition of all particles with the mentioned effects. Each of them can be traced back to one of these two basic concepts: the microscopic and the macroscopic description. The microscopic description deals with the particles themselves and is outlined in this section.

As in every gas, there are generally two problems to deal with. First, there are too many particles: the number of particles is in the order of $N_A \approx 10^{23}$. Even if one could know the equation of motion of every particle, it is impossible to solve this system of equations, even with present-day computers - besides the huge number of equations, they are all coupled to each other. The second issue to deal with are the unknown initial conditions. The particles' positions and velocities at a given time are not measurable. For these reasons, as for all gases, there is a strong need for a statistical description, the kinetic theory.

Define a distribution function for N particles

$$F(x_1, y_1, z_1, x_2, y_2, z_2, ..., x_N, y_N, z_N, v_{1,x}, v_{1,y}, v_{1,z}, ..., v_{N,x}, v_{N,y}, v_{N,z}, t) \ ,$$

giving the possibility that particle 1 is at $(x_1, y_1, z_1, v_{1,x}, v_{1,y}, v_{1,z})$ at a time t, particle 2 at $(x_1, y_1, z_1, v_{N,x}, v_{N,y}, v_{N,z})$ and so on. Provided that each particle has f degrees of freedom, all N particles combined have $2Nf$ degrees of freedom. Therefore this distribution function F is settled in a $2Nf$- dimensional space, called the Γ-space. [7]

To receive an one-particle distribution function for the i-th particle F_i, F is integrated over all remaining particles' positions and velocities. This distribution function F_i gives the possibility that particle i is at $(x_i, y_i, z_i, v_{i,x}, v_{i,y}, v_{i,z})$ at the time t in the six- ($2f$-) dimensional μ-space. In a collision-free, low β[1]-plasma,

---

[1] β decribes the ratio of plasma pressure to magnetic field pressure.

it is possible to neglect the particle interaction, so that $f_i = f_j$. As the particles cannot be distinguished, indices are dropped and

$$f(x, y, z, v_x, v_y, v_z)dx\ dy\ dz\ dv_x\ dv_y\ dv_z$$

becomes the number of particles between x and $x + dx$, y and $y + dy$,z and $z + dz$, v_x and $v_x + dv_x$, v_y and $v_y + dv_y$, and between v_z and $v_z + dv_z$ at a time t [7]. The equation of motion for f is the Boltzmann-equation, which in plasma physics in the collisionless limit is also called the Vlasov-equation,

$$\frac{df}{dt} = \frac{\partial f}{\partial t} + \mathbf{u} \cdot \nabla f + \frac{q}{m}\left(\mathbf{E} + \frac{1}{c}(\mathbf{u} \times \mathbf{B})\right) \cdot \nabla_u f = 0\ . \tag{2.11}$$

In section 3.2.2 the drift kinetic equation for electrons is derived based on the concept given in this section.

2.4 Macroscopic Picture - The Fluid Description

In many cases a full kinetic description contains too much information for solving the actual problem. It has been shown that modeling of plasmas as one or more fluids delivers a deep insight into many plasma physical questions. By averaging, the kinetic quantities and equations can be transferred into macroscopic quantities and the fluid equations.

The macroscopic quantities are obtained via calculation of the moments of the probability density function. As first moment, the density is calculated via

$$n(\mathbf{x}, t) = \int f(\mathbf{x}, \mathbf{v}, t) d^3v\ .$$

The other macroscopic quantities are achieved via

$$\begin{aligned}\langle g(\mathbf{x},t)\rangle &= \frac{\int g(\mathbf{x},\mathbf{v},t)f(\mathbf{x},\mathbf{v},t)d^3v}{\int f(\mathbf{x},\mathbf{v},t)d^3v} \\ &= \frac{\int g(\mathbf{x},\mathbf{v},t)f(\mathbf{x},\mathbf{v},t)d^3v}{n(\mathbf{x},t)} \ .\end{aligned}$$

The function $g(\mathbf{x},\mathbf{v},t)$ is to be chosen dependent on the calculated macroscopic quantity. The momentum can be calculated by setting $\mathbf{g} = m\mathbf{v}$ and the energy by using $g = mv^2/2$. [48]

The fluid equations are calculated by averaging over the Vlasov equation (2.11). The first fluid equation is the continuity equation, it describes the temporal evolution of the particle density n:

$$\partial_t n + \nabla \cdot (n\mathbf{u}) = S \ , \tag{2.12}$$

where the bulk velocity $\mathbf{u}$ is defined as

$$\mathbf{u}(\mathbf{x},t) = \langle \mathbf{v} \rangle = \frac{\int \mathbf{v} f(\mathbf{x},\mathbf{v},t)d^3v}{n(\mathbf{x},t)}$$

and S contains sources and sinks. In (2.12), the partial differentiation $\partial/\partial t$ is shortened to ∂_t. The second fluid equation is the momentum balance equation [19]. In its most used standard form it reads

$$mn\left(\partial_t \mathbf{u} + (\mathbf{u}\cdot\nabla)\mathbf{u}\right) = n\mathbf{F}_L - \nabla\cdot\mathbf{P} - mS\mathbf{u} \ , \tag{2.13}$$

where $\mathbf{P}$ is the pressure tensor, defined by

$$P_{ij} = mn(\langle v_i v_j \rangle - u_i u_j),$$

and the Lorentz-force

$$\mathbf{F}_L = q\left(\mathbf{E} + \frac{\mathbf{u}\times\mathbf{B}}{c}\right) \ .$$

The content of the outer bracket on the left hand site of equation 2.13 can be written in short form as the total derivative d_t:

$$d_t = \partial_t + \mathbf{u} \cdot \nabla \ .$$

Fluid equations are a non-closed system of equations. After the first two, a hierarchy of higher-order equations follows, each containing a quantity defined by the next order equation. Therefore, every fluid model requires an appropriate number of equations and a closing assumption to determine the final variable. This task is often referred to as a "closure problem". In chapter 3 a fluid model is used to describe ions in order to achieve a drift wave model.

2.5 Fusion Energy Devices

As stated in chapter 1, the main goal of fusion energy is to ensure the earth's energy supply with a minimum of environmental impact. Two concepts for fusion energy, based on magnetic confinements, are described in the following sections: tokamaks and stellarators. In section 2.1 it was shown that charged particles cannot be trapped along a magnetic field. The obvious solution is to wrap the magnetic field line into a torus: this is the basis for all magnetic fusion energy devices.

2.5.1 Tokamak

One possibility to confine the plasma is a tokamak, which was invented in Russia 1952. A tokamak is a torus-shaped chamber with magnetic coils to confine the plasma. A strong toroidal magnetic field B_ϕ contains the high temperature plasma within the torus. Unfortunately due to the curved magnetic field the ions will drift downwards leading to a charge imbalance. This drives an outward pointed $\mathbf{E} \times \mathbf{B}$ - drift, as depicted in figure 2.6 a.

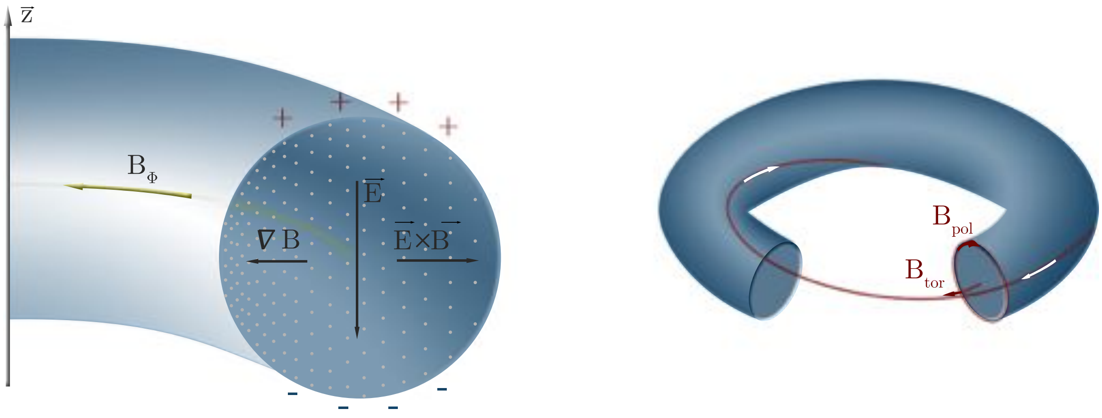

Figure 2.6: Torus - a. Due to the torus geometry ∇B- and curvature drifts occur. Ions drift downwards, an electric field is produced and the particles drift outwards due to $\mathbf{E} \times \mathbf{B}$ - drift. b. The induced plasma current results in a twisting of the magnetic field lines in a torus.

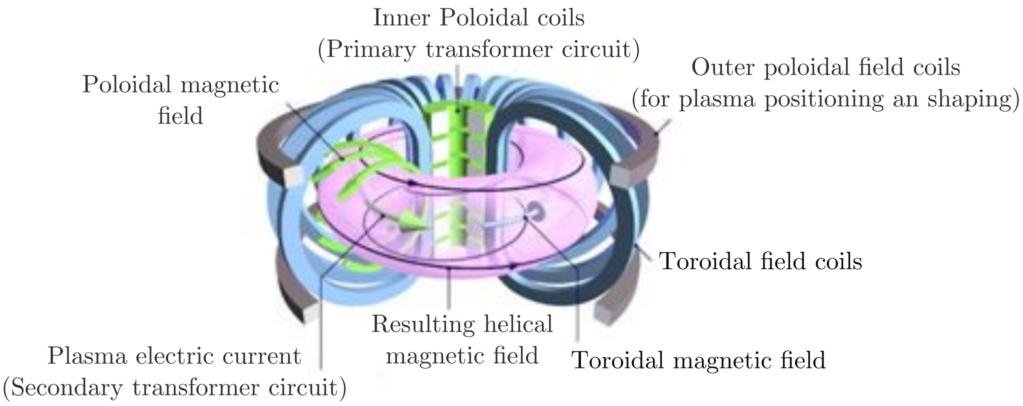

Figure 2.7: Tokamak - Sketch of coils and magnetic fields of the Joined European Tokamak JET (taken from Ref. [1]).

Thus the particles will rapidly drift outwards, hitting the wall and making fusion impossible. An additional weaker poloidal magnetic field is used to twist the magnetic field lines, resulting in nested surfaces that keep the particles trapped. To generate this poloidal field, a toroidal plasma current is induced by a primary winding, employing the plasma itself as secondary winding of a transformer. The plasma current is induced by changing of the magnetic flux B, which is perpendicular to the torus and located in its center. This additional magnetic field as well as the resulting twisted field lines are illustrated in figure 2.6 b.; the whole configuration in shown in figure 2.7.

The deuterium and tritium ions are trapped long enough in the resulting nested surfaces and will, provided with enough energy to overcome their Coulomb barrier, fuse and free energy. As one tries to improve the β-limit, it turns out that the optimal cross-section is non-circular [15]. As a consequence, most modern-day tokamaks are characterized by a shape combining elongation and triangularity as illustrated in figure 2.8 c.

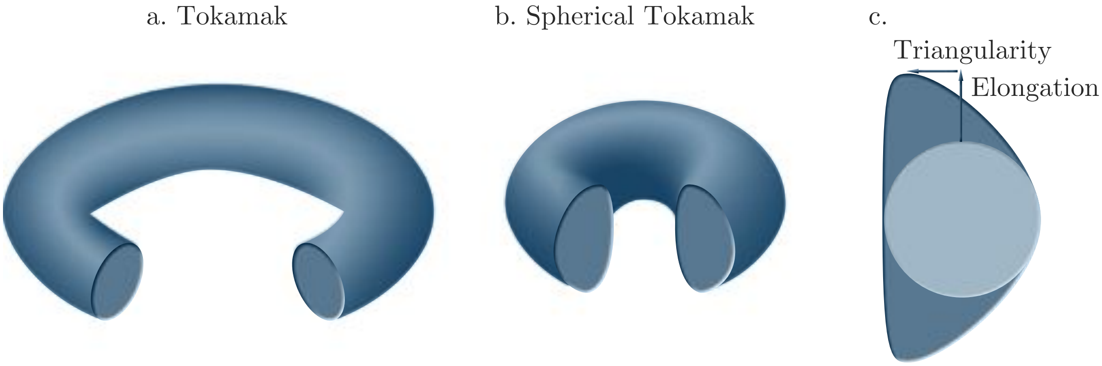

Figure 2.8: Tokamak and spherical tokamak - a. Classical tokamak, b. spherical tokamak, c. both can be characterized by triangularity and elongation.

Still, not all problems are cured: the outside of the tokamak is called the “bad curvature region”, because instabilities are more prevalent. The inner side is the “good curvature region”, since analysis shows that modes are more stable there. As the twisting of the magnetic field brings the particles from the bad back to the good curvature region, one tries to avoid the bad curvature side, which leads to a new concept, the spherical torus. Its shape is illustrated in figure 2.8 b. As depicted in figure 2.9 b., the particle’s trajectory is more in the good curvature than in the outside region. The spherical torus has improved confinement and pressure limits, but the disadvantage is less room in the center for coils, making the use of superconducting magnets impossible [16].

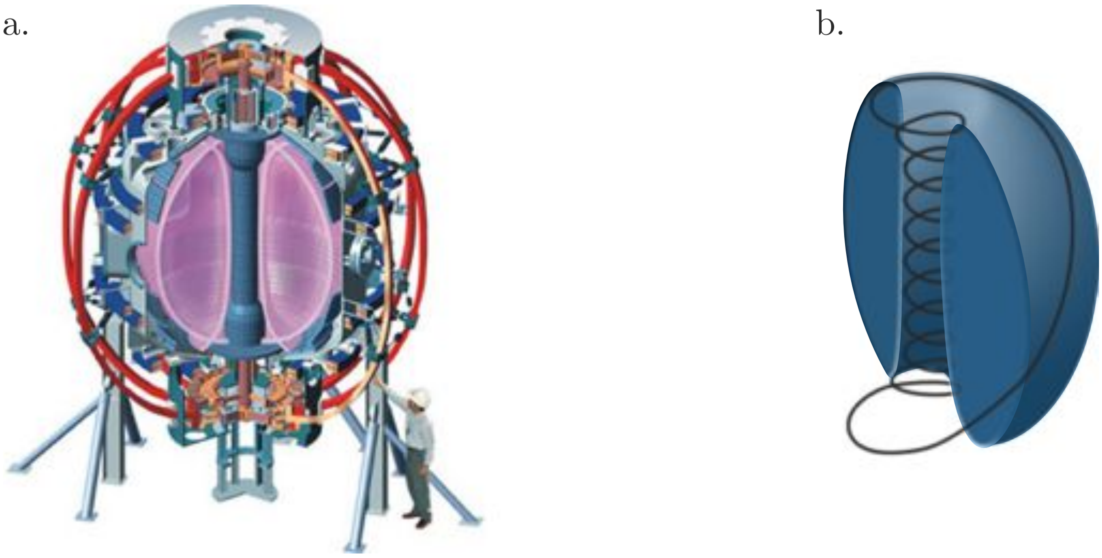

Figure 2.9: Spherical tokamak - a. Schematic sketch of the NSTX magnetic fusion device (taken from Ref. [42]). b. Magnetic field lines of a spherical tokamak: the particles stay longer on the inner, good curvature side than on the outer, bad curvature side.

The major disadvantage of the tokamak concept is the pulsed mode of operation. Resistivity will decrease the induced plasma current, which is critical for the field design as well as for ohmic heating of the plasma. In modern tokamaks, mechanisms such as “current drive”, radio-frequency, and neutral beam injections are used to drive the plasma current. They are limited through the Greenwald limit and other effects, which make it difficult to generate the entire required current by current drive. However, there are other mechanisms to drive the toroidal plasma current without induction. [14]

To avoid problems resulting from the requirement of a plasma current in order to maintain the field geometry, consider another fusion energy device: the stellarator, covered in the next section.

2.5.2 Stellarator

In times when fusion was a restricted science, parallel to the construction of tokamak in the USSR, the stellarator concept was invented by Lyman Spitzer in 1950 [45]. In contrast to a tokamak, in a stellarator the magnetic cage is generated without a toroidal plasma current, so there is no need for a transformer. Thus stellarators work in a non-pulsed mode of operation. To provide the required magnetic cage without a parallel plasma current, there is no longer axial symmetry, but the coils are shaped in complex geometry. The geometry of the coils as well as the resulting plasma shape is illustrated in figure 2.10. It shows the sketch for Wendelstein 7-X, a new stellarator, which is being built in Greifswald, Germany. The advanced configuration of the magnetic field will show the future of the stellarator concept as a candidate for fusion power plants.

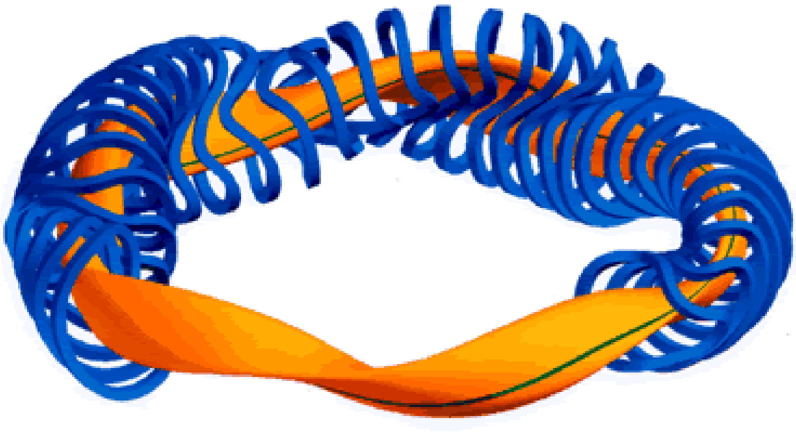

Figure 2.10: Wendelstein 7-X - Scetch of the plasma (orange) and the magnetic coils (blue) of the Stellarator Wendelstein 7-X (taken from Ref. [36]).

Experiments will show which configuration, tokamak or stellarator, is the optimum for future power plants. Not only the physical parameters, but also the cost, will determine this decision. Wendelstein 7-X and ITER hopefully will bring answers to light to solve the earth's energy problem.

2.6 Plasma Transport

The transport of particles in a tokamak greatly exceeds the predicted rates of classical and even that of neoclassical transport theory. Particle collisions alone are not able to explain the high transport coefficients. The reason for the high particle loss in fusion devices are fluctuations in density, potential and temperature. These microinstabilities can drive turbulence [50]. Plasma confinement is today assumed to be mainly affected by turbulent transport.

The first part of this section introduces the random walk, used as a basis for estimations of particle and heat transport. The subsequent parts introduce mixing length theory and gyro-Bohm transport scaling.

2.6.1 Random Walk Diffusion

In 1827 Robert Brown observed the random motion of pollen in water, which was later named after him "Brownian motion" [17]. The Brownian motion as simulated three-dimensional random walk is depicted in figure 2.11. The mechanism behind it was long unknown, until 1905 when Einstein gave the explanation in his famous work "Über die von der molekularkinetischen Theorie der Wärme geforderte Bewegung von in ruhenden Flüssigkeiten suspendierten Teilchen" [12].

He concluded that the motion of the pollen is caused by collisions with randomly moving water molecules, whose motion is so complex that they have to be described probabilistically. His explanation is based on the assumption of the existence of atoms, which was, in contrast to the observation of the Brownian motion, a questionable theory at that time. He assumed that each pollen particle is pushed a small distance away after a certain amount of time, which leads to

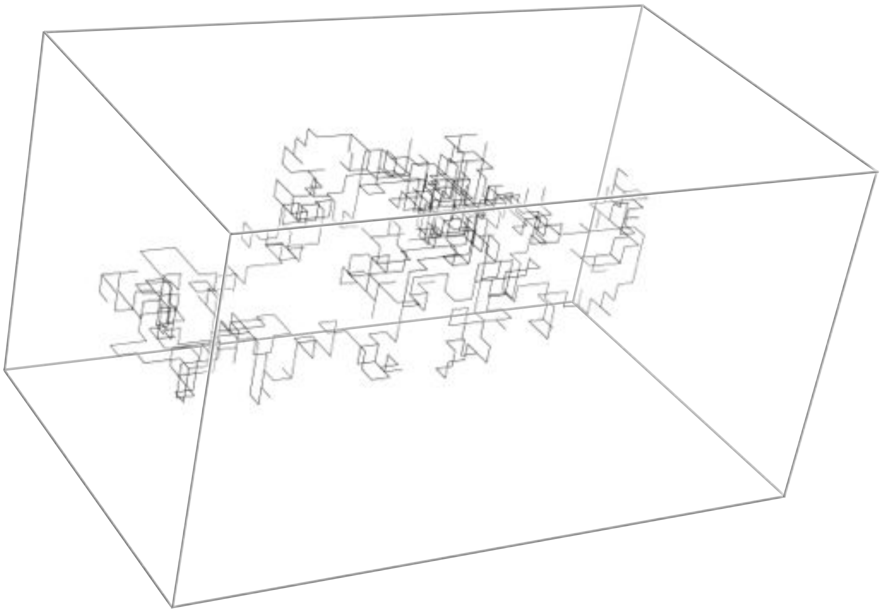

Figure 2.11: Random walk - 3-dimensional random walk.

the already known diffusion equation for the particle density n,

$$\frac{\partial n}{\partial t} = D\frac{\partial^2 n}{\partial^2 x} \ ,$$

with the general solution

$$n(x,t) = \frac{1}{\sqrt{4\pi D t}} e^{-\frac{x^2}{4Dt}} \ .$$

Einstein related the diffusion coefficient D to the arithmetic mean of the square of the displacement

$$\langle x^2 \rangle = 2Dt \ .$$

In the formulation of random walk, the diffusion coefficient is the squared length of one step $(\Delta x)^2$ divided by the time between two steps Δt,

$$D = \frac{(\Delta x)^2}{2\Delta t} \ . \tag{2.14}$$

With good assumptions of Δx and Δt, it is possible to estimate the diffusion of confined plasma particles using a similar argument to the one leading to (2.14). In the next section this concept is used for the estimation of particle diffusion due to drift waves in the context of mixing length theory.

2.6.2 Mixing Length Theory and Turbulent Transport

The mixing length theory was developed by Prandtl, giving an approximation of the diffusion rate. Considering a small fluid element traveling in the fluid, Prandtl assumed the existence of a distance that the fluid element can travel before becoming decorrelated. This distance is the "mixing length", whereas the time it takes a fluid element to decorrelate from its initial state is called the "decorrelation time". Obviously the argument follows the random walk analogy, with the correlation length as mean free path [5].

Drift wave instabilities are fundamental to linear theory and can morph into a turbulent state [49]. Drift wave turbulence is strongly assumed to be responsible for the high transport at the plasma edge of a confined toroidal system [39]. As the focus of this thesis lies on drift waves, they are covered in detail in chapter 3. At this point, the order of magnitude for the diffusivity will be calculated, without specifying the mechanism or accurate growth rate of the drift wave.

Advection caused by drift waves is mainly due to $\mathbf{E} \times \mathbf{B}$ - velocity, leading to an incompressible flow. Considering a fluid element propagating a distance Δx, the fluctuation becomes $\tilde{n} \sim \Delta x \ \nabla_\perp \bar{n}$, where $\nabla_\perp \bar{n}$ is the gradient of the mean density. The mixing length Δx is estimated in terms of a characteristic wave number $\Delta x \sim k_\perp^{-1}$. The decorrelation time is estimated as $\Delta t \sim 1/\gamma$, the inverse drift wave growth rate γ. With the typical scales $k_\perp \sim 1/\rho_s$ and $\gamma \sim L_n/c_s$ an estimation of the density diffusion coefficient for drift wave turbulence is the drift-wave - or gyro-Bohm diffusivity

$$D \sim \frac{\gamma}{k_\perp^2} \sim \left(\frac{\rho_s}{L_n}\right)\left(\frac{cT_e}{eB}\right) \ ,$$

with the density gradient scale length $1/L_n = -\partial_x \ln(n)$. The second factor is the Bohm-diffusivity $D_B = cT_e/eB$ [27]. Since $\rho_s/L_n \ll 1$, the first factor significantly lowers the diffusivity and adds the "gyro-" to the Bohm-diffusivity.

While all diffusion processes can be interpreted as a random walk process (2.14), the finding of the relevant step size Δx and step time Δt is crucial. It depends on various factors involving Lagrangian versus Eulerian decorrelation times, the anisotropy of the turbulence and multiple possible decorrelation mechanisms (see for example different types of mixing length theories in Ref. [28, 38, 51]) [24]. For the purpose of this thesis, D is estimated as $D \sim \gamma(k_y, k_\parallel)/k_y^2$. A more accurate treatment can be given by fully nonlinear gyrokinetic turbulence calculations.

Even though it is tempting, the mixing length estimation of the drift wave diffusivity only predicts the approximate size and is not to be used for calculation of explicit values. Simulations of particle diffusivity due to drift waves based on the mixing length theory are provided in section 5.2.

3

Drift Waves and Microinstabilities

As pointed out in section 2.6, drift wave turbulence is responsible for anomalous transport at the plasma edge of a toroidal confinement system. In simple terms, drift waves are electrostatic, low-frequency dynamics appearing in every confined plasma. Without any special geometric requirements, they are the most universal modes that exist in neutral, magnetized plasmas with pressure gradients. The drift wave instability needs an additional source of dissipation, like resistivity or kinetic effects, to become unstable. Thus, unlike for example Rayleigh-Taylor instabilities, drift wave instabilities have both real frequencies and growth rates and hence are typically not only purely growing, but also traveling in space.

In this chapter drift waves are discussed in detail. Starting with a description of the general drift wave mechanism, the drift wave instability is analyzed. After a short discussion of a nonlinear drift wave model, two linear models are derived in detail. The first model includes drift kinetic electrons and cold fluid ions. The second one treats electrons and ions as kinetic and adds ion polarization drift and finite Larmor radius effects as additional terms to the dispersion relation.

3.1 Drift Wave Instability

To discuss the mechanism of drift waves, a low density plasma in a local slab geometry [8] is assumed. The following consideration is based on figure 3.1, which shows the slab geometry embedded in its original three-dimensional structure.

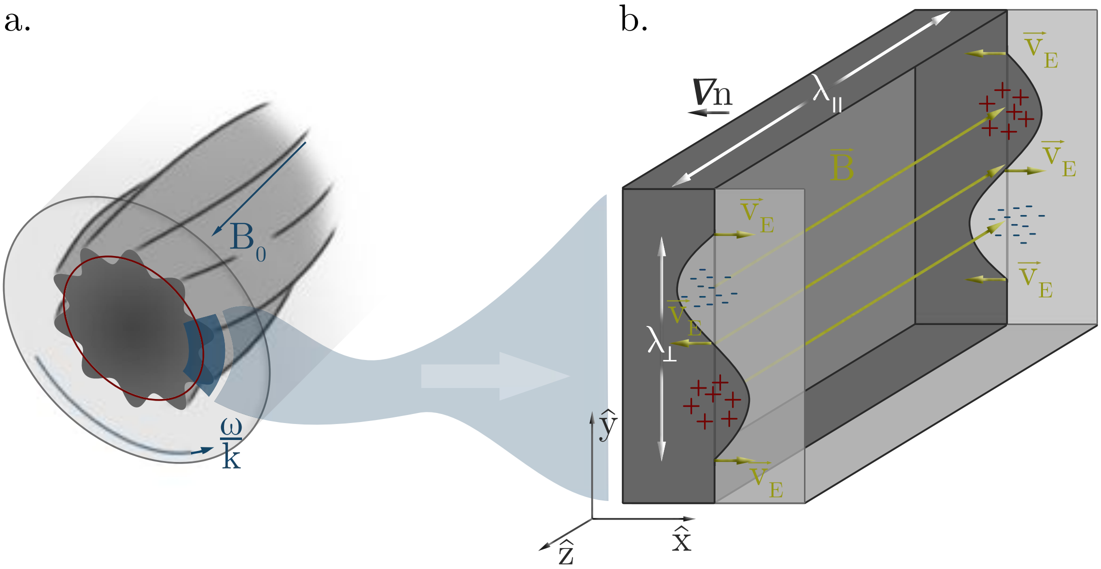

Figure 3.1: Drift wave - a. Section of a torus shaped plasma. In equilibrium the isobar is a concentric circle (red). A small density perturbation drives a drift wave, the mechanism for which is shown in b. The embedding of the plane plasma slab-geometry in a torus is shown in the passage from a. to b.

Consider a constant and homogenous magnetic field parallel to the $\hat{\mathbf{z}}$-axis and a density gradient in negative $\hat{\mathbf{x}}$-direction with $\nabla n_0/n_0 = const.$ The ions are assumed to be cold and there is no electron temperature gradient. Looking at the plasma tube on the left of figure 3.1, in equilibrium the curve of constant density is a concentric circle around the $\hat{\mathbf{z}}$-axis. Assume there is a small oscillating density perturbation

$$\tilde{n} \sim n_0 e^{i(k_\perp y + k_\parallel z - \omega t)}$$

with $k_\perp \gg k_\parallel$. This perturbation in the slab limit of figure 3.1 b., when translated to the geometry of figure 3.1 a., causes isobars with a shape of a twisted cylinder, as depicted in figure 3.1 a.

Choose a value of $k_{\|}$ that is big enough to consider the electrons as free along the magnetic field, $k_{\|} v_{te} \gg \omega$, but $k_{\|} v_{ti} \ll \omega$, to enable neglecting the ions' motion in the $\hat{\mathbf{z}}$-direction. This simplification allows the assumption of adiabatic electrons, fulfilling the linearized Boltzmann-relation

$$n = n_0 + \tilde{n} = n_0 e^{\frac{e\tilde{\Phi}}{T_e}} \approx n_0 \left(1 + \frac{e\tilde{\Phi}}{T_e} \right) . \tag{3.1}$$

In this case the perturbed potential $\tilde{\Phi}$ and the perturbed density, $\tilde{n} = n_0 e\tilde{\Phi}/T_e$, are in phase. Assuming the electrons move freely along the magnetic field, they would spread away from density maxima into density minima, generating parallel currents. Since the ions have much higher inertia than the electrons, they remain in the density maxima, which would result in positive space charge. These space charges are depicted in figure 3.1 with red indicating positive and blue indicating negative preponderance. In reality, there will be a potential $\tilde{\Phi}$ developing that will attract the electrons, as given in equation 3.1, so that the electron density perturbation nearly cancels the ion density perturbation, which is called "quasi-neutrality" and will be elaborated more in section 3.2.1.

The charge imbalances produce perpendicular electric fields $\tilde{\mathbf{E}}_{\perp}$. As described in section 2.2.1, this leads to local $\mathbf{E} \times \mathbf{B}$ - drifts in the perpendicular plane, which causes plasma advection [6]. Since the guiding center distribution is inhomogeneous, the initial density perturbation drifts with the diamagnetic velocity as a transversal wave in the $\hat{\mathbf{x}}$-$\hat{\mathbf{y}}$-plane, perpendicular to both the magnetic field and the density gradient [27], as described in section 2.2.3.

Yet the wave is perfectly stable, since nothing affects the amplitude of the density distribution. As illustrated in figure 3.2, potential $\tilde{\Phi}$ and density $\tilde{n}$ are in phase as described; the $\mathbf{E} \times \mathbf{B}$-drift has a relative phase difference of $\pi/2$.

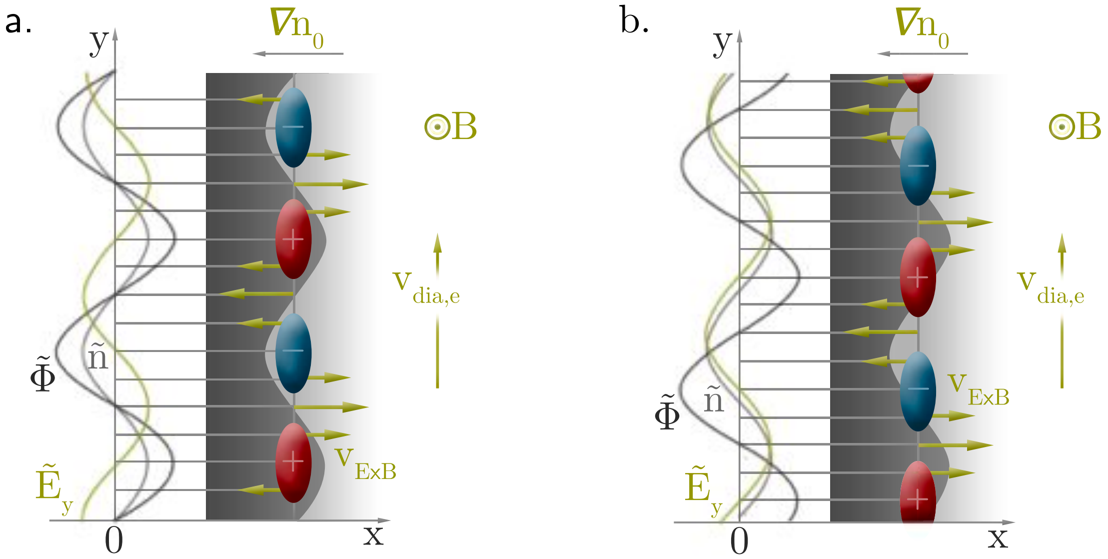

Figure 3.2: Mechanism of the linear drift wave in the perpendicular plane of a local-slab model - The density gradient ∇n_0 is depicted by the gray color gradient, while the linear periodic density instability is embedded. The electrons, moving faster than the ions, cause local negative space charges, which are illustrated in blue for negative charge preponderance and red for positive. The generated $\mathbf{E} \times \mathbf{B}$ - field is depicted with green arrows. In a. drift waves, while in b. drift wave instabilities are illustrated. Respectively on the left side curves for $E_y = -\nabla\tilde{\Phi}$ in green, Φ in dark gray and $\tilde{n}$ in light gray are plotted. In a. there is no phase shift between $\tilde{n}$ and $\tilde{\Phi}$ and a $|\pi/2|$ phase difference to E_y, resulting in a linearly stable, propagating drift wave. In b. there is a phase shift between $\tilde{n}$ and $\tilde{\Phi}$, which describes a linearly unstable drift wave. (adapted from Ref. [6]).

The key to a damping or growing of the drift wave lies in the coupling between the parallel electron motion and the perpendicular drift [41]. Both ions and electrons move with the $\mathbf{E} \times \mathbf{B}$ - velocity, but to offset the rapid parallel motion of the electrons, an electrostatic potential must be created. Modeling as before the electrons as an ideal gas parallel to the magnetic field, the pressure is proportional to the density. Density and potential are coupled by the parallel electron current density $\tilde{n} \leftrightarrow \tilde{j}_{\|} \leftrightarrow \tilde{\Phi}$ [41].

There are some possibilities that break the assumption of adiabatic electrons and result in dissipative coupling [41]: resistivity, which gives rise to resistive drift waves, and electron Landau damping, which is caused by kinetic effects. Another possibility is inductive coupling. The slower electron motion compared to the adiabatic assumption causes a delay in the potential perturbation, resulting in a phase shift between the perturbed potential $\tilde{\Phi}$ and $\tilde{n}$ and in a reduced phase shift between $\mathbf{E} \times \mathbf{B}$ and the density perturbation. The $\mathbf{E} \times \mathbf{B}$ - drift in turn increases the density perturbation, resulting in an unstable wave. Figure 3.2 shows the phase shifts between the variables.

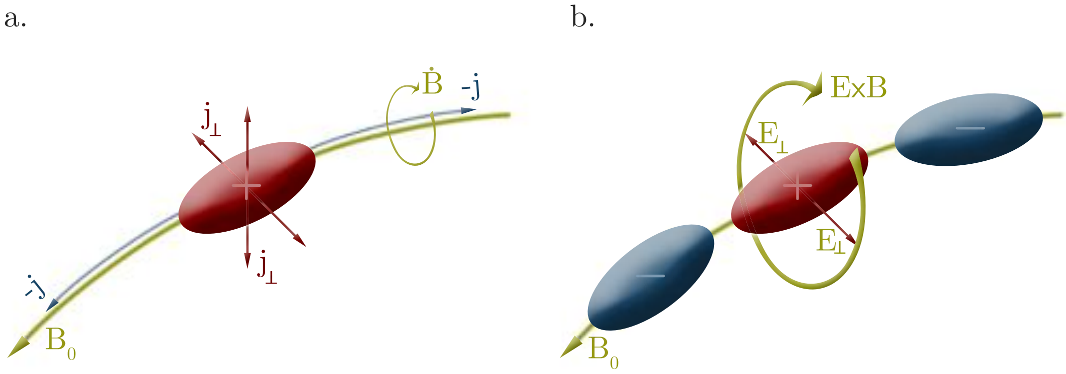

Figure 3.3: Three dimensional dynamic of the drift wave - a. The density perturbation $\tilde{n}$ generates currents: the electrons stream parallel to B_0 with $j_\parallel$ away from the maxima (depicted in blue), and the ions experience the perpendicular polarization drift $j_\perp$ (depicted in red). b. These currents lead to space charges, generating electric fields, which produce drifts [47] (adapted from Ref. [6, 47]).

The description of the three-dimensional mechanism of the drift wave is based on figure 3.3. Until now only the perpendicular part of the wave vector $\mathbf{k} = \mathbf{k}_\perp + \mathbf{k}_\parallel$ was considered for the drift wave dynamics. However, the examined parallel dynamic causes an additional parallel part, where $\mathbf{k}_\perp \gg \mathbf{k}_\parallel$, i.e. $\lambda_\perp \ll \lambda_\parallel$. This gives rise to a stretched wave along the magnetic field as depicted in figure 3.3. The electrons, dominating the parallel dynamic due to their higher mobility, create the mentioned parallel currents $\tilde{j}_\parallel$, which are constrained by self-induction $\partial_t \mathbf{B}$. The ions experience polarization drift. The perpendicular electric field, causing advection of the plasma, is depicted in figure 3.2 [6].

Drift waves in toroidal geometry

The drift wave was considered in local slab geometry, first in two dimensions, then in the three-dimensional case. To be more realistic, it is interesting to examine the case of cylindric geometry. Though the plasma shape of a tokamak is not cylindric, a nonlocal model in form of a closed cylinder, i.e. a torus, is a good model for understanding the functionality of the drift wave in a tokamak. For this purpose, the variables are transformed from the local slab geometry into cylindric coordinates via $(x, y) \rightarrow (r, \theta)$ [13]. Figure 3.4 shows the equidensity and equipotential surfaces of a drift wave in a cylindrical geometry. Both equidensity and equipotential are twisted around the magnetic field, on the perpendicular plane, density and potential perturbations propagate with the diamagnetic velocity.

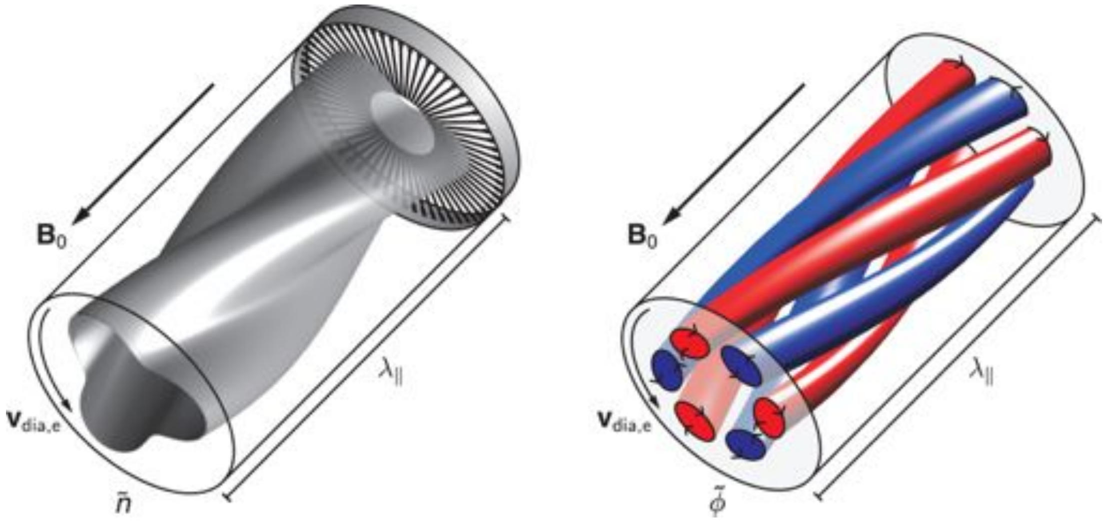

Figure 3.4: The drift wave in cylindrical geometry - The eigenmode structure is azimuthal with mode numbers $m = rk_\perp$[6, 13]. a. Surface of equidensity and b. potential perturbation in cylindrical geometry (taken from Ref. [6]).

Microinstabilities in magnetically confined plasmas

Besides the discussed drift wave, other instabilities arise in magnetically confined plasmas. Figure 3.5 illustrates the location of the most important microinstabilities using the example of ASDEX upgrade. In the core region, ITGs, ETGs and TEMs dominate the particle transport. Drift waves are important in the edge plasma and interchange instabilities dominate in the scape-off-layer (SOL) [34]. ITGs and TEMs are variants of drift waves that involve toroidal magnetic geometry.

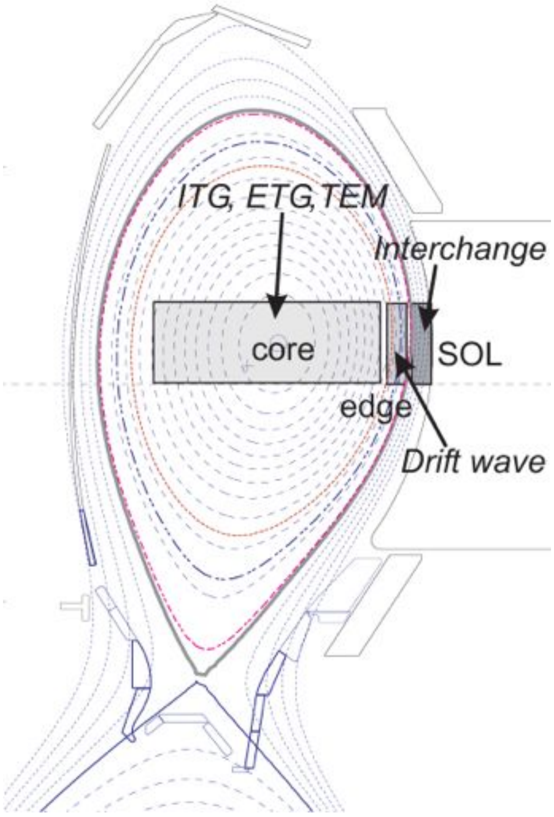

Figure 3.5: Location of microinstabilities - The typical location of microinstabilities in tokamaks, shown in the cross-section of ASDEX upgrade. In the core region ITG, ETG and TEM are present, while in the edge drift waves dominate, and the interchange instability arises in the scape-off-layer (taken from Ref. [34]).

An important criterion to distinguish the modes from each other is the perpendicular scaling, as well as the direction of the group velocity and the instability mechanism. In figure 3.6 the typical microinstabilities of a confined plasma are arranged according to their growth rate γ and perpendicular scale $k_\perp \rho_s$.

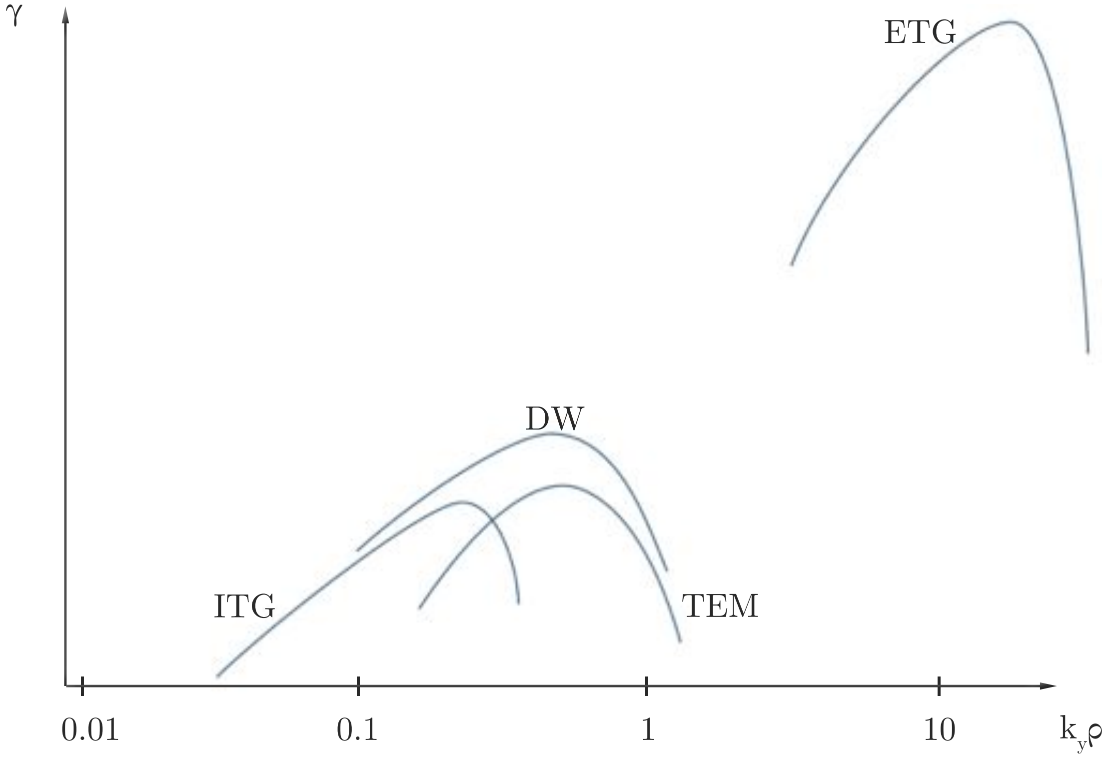

Figure 3.6: Microinstability scaling - Perpendicular scaling of the typical microinstabilities of confined plasmas [24].

3.2 Drift Wave Models

To describe drift waves mathematically, different models, each stressing distinguishing features, are developed in this section. The simplest linear drift wave model with adiabatic electrons will confirm that drift waves propagate with the electron diamagnetic frequency. Since this model is too simplified to cover all drift wave effects, the Hasegawa-Mima equation and the $i\delta$-model are derived, which include nonlinear effects. To describe the drift wave instability, a more comprehensive model is necessary. For the analytic study of drift wave effects, cold ions and a reduced kinetic electron model is used. To examine the current-driven drift wave numerically, kinetic effects of both ions and electrons are included.

3.2.1 Adiabatic Electrons

In this first, simplified model for drift waves, adiabatic electrons and fluid ions are assumed. The unperturbed density gradient provides the free energy to drive the instability. Assuming small scale perturbations $\tilde{n}$, $\tilde{n} \ll n_0$. As the density perturbations do not only have small amplitudes but also short wavelengths, the gradient of the density perturbations $\nabla\tilde{n}$ is in the range of the gradient of the unperturbed density ∇n,

$$\nabla\tilde{n} \sim \nabla n_0 \ . \tag{3.2}$$

As previously discussed in section 3.1, the assumption of adiabatic electrons and cold ions is consistent with the mechanism of drift waves. Thus the electrons fulfill the linearized Boltzmann equation (3.1), $\tilde{n}_e = n_{e,0}e\tilde{\Phi}/T_{0,e}$. Assuming cold ions, $T_{0,i} \ll T_{0,e}$ with finite $T_{0,i}/T_{0,e}$, the ions' thermal velocity is much less than the electrons', $v_{t,i} \ll c_s \ll v_{t,e}$. Since the diamagnetic velocity is according to equation 2.10 proportional to the temperature, $v_{di} \ll v_{de}$. As a consequence the ion thermal velocity is negligible and ions are described as cold fluid, characterized by the conservation law

$$\partial_t n_i + \nabla \cdot (n_i \mathbf{u}) = 0 \ , \tag{3.3}$$

neglecting higher order fluid equations. Since the equilibrium value of the density $n_{0,i}$ does not depend on time, $n_i(\mathbf{x}, t) = n_{0,i}(\mathbf{x}) + \tilde{n}_i(\mathbf{x}, t)$, equation 3.3 becomes

$$\partial_t \tilde{n} + \mathbf{u} \cdot \nabla (n_{0,i} + \tilde{n}_i) + n_i \nabla \cdot \mathbf{u} = 0 \ . \tag{3.4}$$

Simplication can verify the prediction of section 3.1, namely that the classic drift wave propagates with the electron dielectric frequency. First, ignoring the parallel dynamics and polarization effects of the ions, the velocity $\mathbf{u}$ becomes the $\mathbf{E} \times \mathbf{B}$ - drift velocity $\mathbf{v}_E = c/B(\hat{\mathbf{e}}_z \times \nabla \Phi)$. Due to the slab limit assumption, which is described in detail in section 3.2.2, the last term in (3.4), $\sim \nabla \cdot \mathbf{u}$, can be dropped. Although the second term dotted with $\mathbf{u}$, $\sim \nabla \tilde{n}_i$, is nonlinear, it has to be kept to satisfy the gradients' ordering assumption in (3.2). However, for this simplified linear consideration the nonlinear term is neglected.

After Fourier transformation and the application of the quasineutrality condition, equation (3.4) becomes the dispersion relation for linear drift waves,

$$\omega = -\frac{k_y c T_{0,e}}{eB} \frac{\partial_x n_0}{n_0} = \frac{k_y c T_{0,e}}{eBL_n} = \omega_{*e} \ .$$

For the frequency to be positive, either the density gradient or the perpendicular wave number, k_y, has to be negative. In this work the density gradient is defined to be negative, $d_x n_0 = -n_0/L_n$ and thus $k_y > 0$. This result is consistent with the consideration of the basic drift wave mechanism in section 3.1: The basic drift wave propagates with electron diamagnetic velocity v_{de}.

Repeating this derivation without dropping nonlinear terms and including ion polarization effects additional to the $\mathbf{E} \times \mathbf{B}$ - drift results in the Hasegawa-Mima equation [25].

The $i\delta$-Model and the Hasegawa-Mima-Equation

The Hasegawa-Mima equation is the simplest nonlinear model, covering drift waves, by describing electrostatic potential fluctuations in the presence of a background density gradient. As drift waves also cover the domain of microinstabilities with small structures $k_\perp \rho_s > 1$, the ion polarization drift has to be considered. Thus, the ion velocity $\mathbf{u}$ in (3.3) consists of the $\mathbf{E} \times \mathbf{B}$ - drift, $\mathbf{v}_E$, and the ion polarization drift, $\mathbf{v}_{i,p}$,

$$\mathbf{u} = \mathbf{v}_E + \mathbf{v}_{i,p} \ .$$

The actual ion density consists of the guiding center density, $n_{i,gc}$, and the ion polarization density, $n_{i,pol}$, [32, 43]

$$n_i = n_{i,gc} + n_{i,pol} \ .$$

Thus the fluid equation 3.3 becomes

$$\begin{aligned}&(\partial_t + \mathbf{v}_E \cdot \nabla)\, n_{i,gc} + (\partial_t + \mathbf{v}_E \cdot \nabla)\, \tilde{n}_{i,pol} \\ &+ \mathbf{v}_{i,p} \cdot \nabla(n_{i,gc} + \tilde{n}_{i,pol}) + (n_{i,gc} + \tilde{n}_{i,pol})\nabla \cdot \mathbf{v}_{i,pol} = 0 \ . \end{aligned} \tag{3.5}$$

The gyrocenter density $n_{i,gc}$ fulfills equation 3.4, which is equivalent to (3.5) with $u_{i,pol} = 0$. The terms $\sim \mathbf{v}_{i,p} \cdot \nabla n$ and $\sim \tilde{n}_{i,pol} \nabla \cdot \mathbf{v}_{i,p}$ can be neglected since $|\mathbf{v}_{i,p}| \ll |\mathbf{v}_E|$ and $|\tilde{n}_{pol}| \ll |n_{i,gc}|$. Thus, equation 3.5 becomes

$$(\partial_t + \mathbf{v}_E \cdot \nabla)\, n_{i,gc} + (\partial_t + \mathbf{v}_E \cdot \nabla)\, \tilde{n}_{i,pol} + n_{i,gc} \nabla \cdot \mathbf{v}_{i,pol} = 0 \ . \tag{3.6}$$

Solving the last two terms, $d_t n_{i,pol} = -n_{i,gc} \nabla \cdot \mathbf{v}_{i,pol}$, results after integration in time in the ion polarization density:

$$\tilde{n}_{i,pol} = n_{i0}\rho_s^2\nabla_\perp^2\frac{e\tilde{\Phi}}{T_{0,e}} \ . \tag{3.7}$$

Considering the first term of equation 3.6, the gyrocenter density, which consists of an equilibrium and a perturbed part, $n_{i,gc} = n_{i0} + \tilde{n}_{i,gc}$, satisfies

$$\partial_t\tilde{n}_{i,gc} + i\omega_{*e}\frac{e\tilde{\Phi}}{T_{0,e}}n_{i,0} + \mathbf{v}_E\cdot\nabla\tilde{n}_{i,gc} = 0 \ . \tag{3.8}$$

The quasi-neutrality condition, $\tilde{n}_i \approx \tilde{n}_e$ with $n_{i,0} \approx n_{e,0}$, reads now

$$\tilde{n}_{i,gc} + \tilde{n}_{i,pol} = \tilde{n}_e \ . \tag{3.9}$$

As discussed in the previous section 3.1, the drift wave is stable, unless there is additional dissipation to create a phase shift between density and potential. To cover drift wave instabilities the $i\delta$-model is used, which adds a small imaginary phase to the Boltzmann-relation [27],

$$n_e = n_{0,e}e^{\frac{e\tilde{\Phi}}{T_{0,e}}}e^{-i\delta_{\mathbf{k}}} \ . \tag{3.10}$$

With the linearization of (3.10), the perturbed part of the density becomes

$$\tilde{n}_e \approx n_{e,0}[1 - i\delta_{\mathbf{k}}]\frac{e\tilde{\Phi}}{T_{0,e}} \ . \tag{3.11}$$

Inserting (3.7), $\tilde{n}_{i,pol}$, in the quasi-neutrality condition (3.9) and using the linearized $i\delta$-Boltzmann relation (3.11), the perturbed ion gyrocenter density becomes

$$\tilde{n}_{i,gc} = n_{e,0}[1 - i\delta_{\mathbf{k}} - \rho_s^2\nabla_\perp^2]\frac{e\tilde{\Phi}}{T_{0,e}} \ . \tag{3.12}$$

The concept of the "quasineutrality approximation" appears to be contradictory, since with an exact neutrality, no potentials could exist in the plasma. However, the quasi-neutrality condition (3.9) can be replaced with the exact Poisson equation:

$$-\nabla^2\Phi = 4\pi e\left(\tilde{n}_{i,gc} + \tilde{n}_{i,pol} - \tilde{n}_e\right)\ .$$

With the insertion of the equations 3.7 and 3.11, the perturbed ion gyrocenter density becomes

$$\tilde{n}_{i,gc} = n_{e,0}[1 - i\delta_{\mathbf{k}} - (\rho_s^2 + \lambda_{De}^2)\nabla_\perp^2]\frac{e\tilde{\Phi}}{T_{0,e}}\ . \tag{3.13}$$

This is comparable to equation 3.12, which was achieved by using quasineutrality, with the additional term involving the Debye length $\lambda_{De} = \sqrt{T_e/(4\pi n e^2)}$. For typical plasma parameters, $\lambda_{De}^2/\rho_s^2 \sim 10^{-3}$ is negligible. Thus, the potential is determined by the “quasineutral” requirement: it attracts electrons in order to nearly balance out the ions.

Finally, inserting equation 3.12 into equation 3.8, the $i\delta$-model can be written as

$$\begin{aligned} & n_0[1 - i\delta_{\mathbf{k}} - \rho_s^2\nabla_\perp^2]\partial_t\frac{e\tilde{\Phi}}{T_{0,e}} + i\omega_{*e}\frac{e\tilde{\Phi}}{T_{0,e}}n_0 \\ & +\frac{c}{B}\hat{\mathbf{e}}_z \times \nabla\tilde{\Phi}\cdot\nabla(n_0[1 - i\delta_{\mathbf{k}} - \rho_s^2\nabla_\perp^2]\frac{e\tilde{\Phi}}{T_{0,e}}) = 0\ . \end{aligned} \tag{3.14}$$

The Hasegawa-Mima equation is obtained by setting the phase shift $\delta_{\mathbf{k}} = 0$. It describes an undriven, purely stable drift wave. The last term in (3.14) includes the nonlinear terms. As the two-dimensional vorticity is

$$\Omega = \hat{\mathbf{e}}_z \cdot \nabla \times \mathbf{v}_E = \frac{c}{B}\nabla^2\Phi\ ,$$

this term includes the advection of vorticity [29]. The Hasegawa-Wakatani equation is an advancement of the Hasegawa-Mima equation, including resistive coupling and thus a decrease or increase of the growth rate of the mode, which can be represented by $\delta_{\mathbf{k}} \neq 0$.

In contrast to the oversimplified case $\omega = \omega_{*e}$, the frequency of the drift wave, described by the $i\delta$-model, is [47]

$$\omega = \frac{\omega_{*e}}{1 + \rho_s^2 k_\perp^2 - i\delta_{\mathbf{k}}} \; . \tag{3.15}$$

It is obvious that the polarization drift becomes the more important the smaller the structure is. Figure 3.7 illustrates the growing influence of the polarization drift on the frequency, as $k_z \rho_s$ becomes bigger.

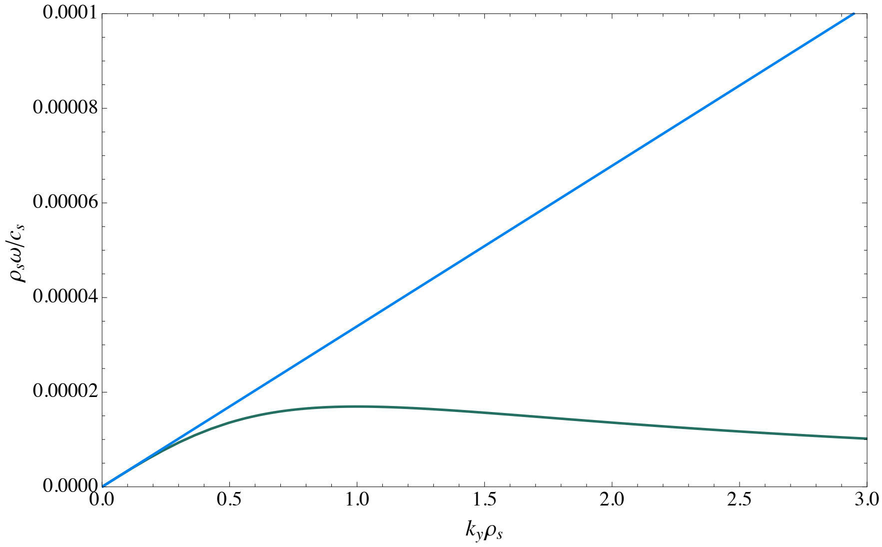

Figure 3.7: Drift wave dispersion relation according to (3.15) - Difference between inclusion (green curve) and exclusion (blue straight line) of ion polarization drift effects. The parameters are $i\delta = 0$ and $T_e = 1\text{keV}$, $B = 5.2\text{T}$ and $L_n = 25.8563\text{cm}$.

The growth rate γ of the drift wave in this model becomes

$$\gamma = \frac{\omega_{*e}}{1 + \rho_s^2 k_\perp^2} \delta_{\mathbf{k}} \; .$$

Thus, the drift wave is unstable if $\omega_{*e} \delta_{\mathbf{k}} > 0$. In the following sections drift wave models that include kinetic effects as sources of dissipation are developed. As the purely drift-kinetic treatment used in this work does not include ion polarization drift (but is reducible to the adiabatic case), the previously-developed model will be used to include this important effect.

3.2.2 Kinetic Electrons

We are interested in non-resistive drift waves, driven unstable by kinetic effects to determine the influence of a parallel electron current. The first model, developed in this chapter, includes kinetic electrons and fluid ions, a second model in the next section will treat both electrons and ions as kinetic.

In the first step the drift-kinetic equation for electrons is derived including density and temperature gradients and a parallel electron current. As before, the electrostatic case in a plane plasma slab is assumed. The derivations and thoughts of this section are guided by [21].

Drift Kinetic Description of the Electrons

As explained in 2.3 the equation of motion for the kinetic theory is the Vlasov equation

$$\partial_t f_e + \nabla_{\mathbf{x}} \cdot (f_e \dot{\mathbf{x}}) + \nabla_{\mathbf{v}} \cdot (f_e \dot{\mathbf{v}}) = 0 \ , \tag{3.16}$$

where a constant mass is assumed and $\nabla_{\mathbf{v}} \cdot\ = (\partial_{v_1}, \partial_{v_2}, \partial_{v_3}) \cdot$ is the three-dimensional divergence with respect to the velocity coordinates.

To build a model covering the behavior of drift waves in a local slab geometry, the Vlasov equation (3.16) will be simplified in several steps. The main assumption is the neglect of the particle gyration, leading to a drift-kinetic description. The main spatial scale is ρ_s, the ions' gyroradius evaluated at the electrons' temperature. Since $\rho_e = \rho_s \mu^{-1}$ with $\mu = \sqrt{m_i/m_e} \approx 60$, the gyration radius of electrons is small compared to ρ_s, allowing to equate the particle distribution function to the distribution function of the gyration center, $f_e = f_{gc}$. In this drift kinetic description the gyro center motion and additional drift motions, described in section 2.1, are considered.

For the guiding center description the dimension can be reduced by one by writing the velocity components in cylindrical coordinates:

$$\partial_t f_e + \nabla_{\mathbf{x}} \cdot (f_e \cdot \dot{\mathbf{x}}) + \frac{1}{v_\perp}\partial_{v_\perp}(\dot{v}_\perp v_\perp f_e) + \partial_{v_\parallel}(\dot{v}_\parallel f_e) = 0 \ . \tag{3.17}$$

Assuming electrostatic waves in a plane plasma slab with a strong, uniform and straight magnetic field in the $\hat{\mathbf{z}}$-direction, $\mathbf{B} = B\ \hat{\mathbf{e}}_z$, the component parallel to the magnetic field is $v_\parallel = v_z$. The plasma is defined to be uniform and infinite extended in the $\hat{\mathbf{y}}$- and $\hat{\mathbf{z}}$-directions, and all gradients are assumed to be in the $\hat{\mathbf{x}}$-direction.

As seen in section 3.1 when analyzing the mechanism for drift waves, there has to be a small initial disturbance in the density $\tilde{n}$ to cause disturbances in the electric potential $\tilde{\Phi}$. By assuming a WKB-approximation, the variables consist of an equilibrium part and a small wave-like disturbance $\sim e^{i(-\omega t + k_y y + k_z z)}$. Considering electrostatics, $\mathbf{E} = \mathbf{E}_0 + \tilde{\mathbf{E}}$ simplifies to

$$\mathbf{E} = \mathbf{E}_0 = -\nabla\tilde{\Phi} \ .$$

As pointed out in section 2.2.2 the polarization drift is negligible for electrons in respect to the $\mathbf{E} \times \mathbf{B}$-drift, so the guiding center motion, the sum of parallel velocity and drifts, can be described as

$$\mathbf{v} = \mathbf{v}_\parallel + \mathbf{v}_E = v_z\hat{\mathbf{e}}_z + \frac{c}{B}\mathbf{E} \times \hat{\mathbf{e}}_z \ .$$

By assuming a uniform magnetic field and electrostatics, the $\mathbf{E} \times \mathbf{B}$-drift leads to an incompressible flow

$$\nabla \cdot \mathbf{v}_E = 0 \ . \tag{3.18}$$

A further consequence of the uniformity of $\mathbf{B}$ is the constancy of the first adiabatic moment $\mu = \frac{mc}{2B}v_\perp^2$ leading to a time-constant perpendicular velocity

$$\dot{v}_\perp = 0 \; . \tag{3.19}$$

The parallel acceleration of the electrons is given by the electric field

$$\dot{v}_\parallel = -\frac{e}{m}E_z \; . \tag{3.20}$$

Combining (3.18), (3.19) and (3.20) and inserting in (3.17), the simplified drift kinetic equation in the electrostatic plane plasma slab-limit is:

$$\partial_t f_e + \frac{c}{B}(\mathbf{E} \times \hat{\mathbf{e}}_z) \cdot \nabla_\perp f_e + v_z \partial_z f_e - \frac{e}{m}E_z \; \partial_{v_z} f_e = 0 \; . \tag{3.21}$$

This simplified drift kinetic equation is valid for ions as well when changing $e \rightarrow -e$. The negligible electron gyration radius allowed one to consider only the gyration center motion and particle drifts. This reasoning fails for ions, so when using drift kinetic for ions, second order effects like the polarization drift and additional finite Larmor radius (FLR) effects must be taken into account. In this model cold fluid ions are assumed. However for the second model derived in section 3.2.3 drift kinetic ions are used, so that additional terms and factors alter the ions' response.

The next step is to calculate the response of the electrons to a small disturbance resulting in a drift wave. Small oscillations of the plasma and the electromagnetic fields are assumed in order to linearize the equations. This means, only first-order expressions in any perturbed quantity are taken into account. Additionally the plasma is assumed to be uniform on space scales greater than one wavelength.

These two assumptions allow a Fourier transformation of equation 3.21 in time and space. As discussed previously, the macroscopic quantities like density or temperature consist of an equilibrium and a small perturbed part. Since the macroscopic quantities are calculated from the distribution function f, as pointed out in section 2.3, f exists likewise as $f = f_0 + \tilde{f}$ with $\tilde{f} \ll f_0$. In many cases a Maxwellian distribution function is valuable, so the equilibrium part of the distribution function is assumed to be Maxwellian:

$$f_0(x, v) = n_0(x) \left(\frac{m}{2\pi T_0(x)} \right)^{3/2} e^{-\frac{m(\mathbf{v} - u_\parallel(x)\hat{\mathbf{e}}_z)^2}{2T_0(x)}} \;,$$

assuming an x-dependency in temperature T_0, density n_0 and in the parallel electron velocity $u_\parallel(x)\hat{\mathbf{e}}_z$.

In the next step equilibrium and perturbed parts of the quantities are inserted in (3.21). Fourier transformation gives $\partial_t f = \partial_t \tilde{f} = -i\omega\tilde{f}$ and for the gradients in position- and velocity-space

$$d_x f_0 = -\left[1 + \frac{\eta}{2} \left(\frac{(\mathbf{v} - \mathbf{u})^2}{v_t^2} - 3 \right) + \eta_u \frac{(v_\parallel - u_\parallel)u_\parallel}{v_t^2} \right] \frac{f_0}{L_n} \;, \tag{3.22}$$

$$\nabla \tilde{f} = i(0, k_y, k_z)\tilde{f} \;, \qquad \partial_{v_\parallel} f_0 = -\frac{v_\parallel - u_\parallel}{v_t^2} f_0 \;, \tag{3.23}$$

with the gradient scaling lengths L, $1/L_n = -\partial_x n_0/n_0$ and $1/L_u = -\partial_x u_0/u_0$. The ratio of the scaling lengths are $\eta = L_n/L_T$ and $\eta_u = L_n/L_u$. Linearizing equation 3.21 while taking into account only first order perturbations brings further simplifications. As $\mathbf{v}_E \cdot \nabla \tilde{f} = 0$,

$$\mathbf{v} \cdot \nabla f = i k_z v_z \tilde{f} + v_{E,x}\, d_x f_0 \;. \tag{3.24}$$

Combining (3.22), (3.23) and (3.24) and eliminating all higher order terms, the simplified drift kinetic equation (3.21) becomes

$$\tilde{f}_e = \frac{e\tilde{\Phi}}{T_{0,e}} f_0 \left(1 - \frac{\omega - \omega_* Q - k_z u_z}{\omega - k_z v_z} \right)$$

with

$$Q = 1 + \eta \left(\frac{(\mathbf{v} - \mathbf{u})^2}{2v_t^2} - \frac{3}{2} \right) + \eta_u \frac{(v_z - u_z)u_z}{v_t^2} \ .$$

The diamagnetic velocity for constant T and $\mathbf{x}$-dependent n, is, in slab geometry with negative density gradient, for electrons:

$$\mathbf{v}_{de} = -\, c \frac{\nabla p \times \mathbf{B}}{qB^2 n} = \frac{cT_0}{eB} \frac{\partial_x n_0}{n_0} \hat{\mathbf{e}}_x \times \hat{\mathbf{e}}_z = \frac{cT_0}{qBL_n} \hat{\mathbf{e}}_y \ .$$

Thus, the electron diamagnetic frequency is

$$\omega_* = k_y v_{de} = \frac{cT_0}{eB} \, \frac{k_y}{L_n} \ .$$

To calculate the response of the electrons, the distribution function is integrated over the velocity space

$$\tilde{n}_e = \int d^3\mathbf{v} \ \tilde{f}_e = 2\pi \int\limits_{-\infty}^{\infty} dv_\parallel \int\limits_{0}^{\infty} dv_\perp \ v_\perp \ \tilde{f}_e \ .$$

The integration over $v_\perp$ is a standard Gaussian integral. Because of its singularity at $(\zeta - q)$, the integral over $v_\parallel$ can be calculated with a modified plasma dispersion function Z:

$$Z_u = Z(\zeta - q) = \frac{1}{\sqrt{\pi}} \int \frac{e^{-t^2}}{t - (\zeta - q)} dt \ , \tag{3.25}$$

where $t = (v_z - u_\parallel)/(\sqrt{2} v_t)$ collects the exponent and $q = u_\parallel k_z/(|k_z|\sqrt{2} v_t)$ includes the parallel electron current. For compactness the following normed quantities are introduced for the frequencies: $\zeta = \omega/(\sqrt{2}|k_z|v_t)$ is the quotient of phase velocity to thermal velocity and $\zeta_* = \omega_*/(\sqrt{2}|k_z|v_t)$ includes the diamagnetic velocity frequency. Integrating by parts, the perturbed electron density becomes

$$\begin{aligned} \tilde{n}_e = n_0 \frac{e\tilde{\Phi}}{T_{0,e}} \Bigg\{ & 1 - \zeta_* \left[\eta(\zeta - q) + 2\eta_u q \right] \qquad (3.26) \\ & + \left[\zeta - q - \zeta^* \left(1 - \eta \left[\frac{1}{2} - \zeta^2 + 2q\zeta - q^2 \right] - \eta_u \left[2q^2 - 2q\zeta \right] \right) \right] Z_u(\zeta - q) \Bigg\} \ . \end{aligned}$$

For the analytic study of drift waves in section 3.4 as well as for numerical considerations in section 5, Z will be approximated. For the analytic method, $\omega \ll k_z v_{te}$ will be assumed, so the calculation can be done by considering polar residues. In the analytic consideration a four-pole approximation is used.

Fluid Description of the Ions

As in section 3.2.2 the ions are assumed to be cold, described by the conservation law (3.3)

$$\partial_t n_i + \nabla \cdot (n_i \mathbf{u}) = 0 \ .$$

Ion polarization effects are not negligible, thus, the perpendicular velocity becomes according to (2.9)

$$\begin{aligned} \mathbf{u}_\perp = \mathbf{v}_E + \mathbf{v}_{pi} &= \frac{c}{B}\hat{\mathbf{e}}_z \times \nabla\Phi + \frac{1}{\Omega_c}\hat{\mathbf{e}}_z \times d_t \mathbf{v}_E \\ &= \frac{c}{B}\hat{\mathbf{e}}_z \times \nabla\Phi + \frac{1}{\Omega_c}\frac{c}{B} d_t \nabla_\perp \Phi \ . \end{aligned} \tag{3.27}$$

The parallel part of the electric field accelerates the ions and causes parallel motion

$$d_t u_\parallel = \frac{e}{M} E_z \ . \tag{3.28}$$

As for the electrons the equations (3.3) and (3.27) are inserted in (3.28) and linearized, resulting in

$$\tilde{n}_i = n_{i0} \frac{e\tilde{\Phi}}{T_{0,e}} \left(\frac{\omega_{*,e}}{\omega} - \rho_s^2 k_\perp^2 + \frac{c_s^2 k_z^2}{\omega^2} \right) \ . \tag{3.29}$$

The first term in (3.29) is the known electron diamagnetic frequency. The second term arises from the ion polarization drift.

Dispersion Relation

To close this model, the ion and electron responses are substituted into the Poisson equation, $\nabla \cdot \mathbf{D} = 4\pi\rho$, which is for this case

$$\nabla\tilde{\Phi} = -4\pi e(\tilde{n}_i - \tilde{n}_e) \ ,$$

resulting in an equation for $\tilde{\Phi}$. In the here assumed limits the application of the quasi neutrality condition $n_e = n_i$ is reasonable, replacing the Poisson equation. Inserting equation 3.26 for n_e and (3.29) for n_i leads to a dispersion relation for drift waves:

$$\begin{aligned} &1 - \zeta_* \left[\eta(\zeta - q) + 2\eta_u q\right] - \left[\frac{\zeta_*}{\zeta} - \rho_s^2 k_\perp^2 + \frac{1}{2\mu^2\zeta^2}\right] \qquad (3.30) \\ &= - \left[\zeta - q - \zeta^* \left(1 - \eta\left[\frac{1}{2} - \zeta^2 + 2q\zeta - q^2\right] - \eta_u\left[2q^2 - 2q\zeta\right]\right)\right] Z_u(\zeta - q) \ . \end{aligned}$$

In section 3.4 this dispersion relation is simplified for a specific regime in order to analytically estimate the growth rate of the drift wave instability.

3.2.3 Kinetic Ions

To drop the condition of cold fluid ions in order to include more effects, a second model for drift waves is set up. In this section, the ions are described, as the electrons, by a drift kinetic equation.

To use the previously derived drift kinetic equation 3.26 for ions, the sign of the charge has to be changed, since the negative charge of the electrons was already included in the derivation:

$$e \rightarrow -e, \qquad\qquad \omega_{*,e} \rightarrow \omega_{*,i} = -\epsilon_T \omega_{*,e} \ ,$$

where $\epsilon_T = T_i/T_e$. All indices switch from $e \rightarrow i$, allowing different values for electrons and ions for the following parameters: $T_{0,e/i}$, $\eta_{e/i}$, $\omega_{*,e}$, $u_{0,e/i}$, $\eta_{u,e/i}$ and

$m_{e/i}$. To ensure quasi neutrality, the density scaling factor is the same for both electrons and ions, $(-d_x n/n)^{-1} = L_{n,e} = L_{n,i}$.

As previously discussed, the inclusion of ion polarization effects is crucial for the description of drift waves. Since the drift kinetic description of the perturbed ion density, (3.26), does not consider polarization drifts, an additional term is added to n_i:

$$n_i = n_{i,0} + \tilde{n}_i + \tilde{n}_{i,pol} \ .$$

In section 3.2.1, the ion polarization density, $\tilde{n}_{i,pol}$, was derived to be

$$\tilde{n}_{i,pol} = n_{i0}\rho_s^2 k_\perp^2 \frac{e\tilde{\Phi}}{T_{0,e}} \ .$$

To improve the model for finite ion temperature, finite Larmor radius effects will be included, which requires an improved polarization density:

$$\tilde{n}_{i,pol} = n_{i0}\left(1 - \Gamma_0\right)\frac{e\tilde{\Phi}}{T_{0,i}} \ , \tag{3.31}$$

where $\Gamma_0(b) = exp(-b)I_0(b)$ and $b = k_\perp^2 \rho_i^2$ [9]. The factor $I_0(b)$ is the modified Bessel function, which is defined as

$$I_n(b) = i^{-n} J_n(ib) \ ,$$

with the Bessel function J_n. For small b, I_n can be approximated to [2]

$$I_n(b) \sim \frac{(b/2)^n}{\Gamma(n+1)} \ ,$$

which gives $I_0 = 1$ for $n = 0$. The exponential function will be approximated by a Padè-approximation, and so Γ_0 becomes

$$\Gamma_0(k_\perp^2\rho_i^2) \sim \frac{1}{1 + k_\perp^2\rho_i^2} \ . \tag{3.32}$$

Inserting (3.32) into (3.31), the ion polarization density that includes finite Larmor radius effects, is

$$\tilde{n}_{i,pol} = n_{i0} \frac{k_\perp^2 \rho_s^2}{1 + k_\perp^2 \rho_i^2} \frac{e\tilde{\Phi}}{T_{0,e}} \ .$$

Like the ion polarization density, all perturbed parts can be adjusted to include finite Larmor radius effects by dividing the densities by $1 + k_\perp^2 \rho^2$ as follows:

$$\tilde{n}_{e/i} \to \frac{\tilde{n}_{e/i}}{1 + k_\perp^2 \rho_{e/i}^2} \ .$$

For electrons, $k_\perp^2 \rho_e^2 \ll 1$; however, for the sake of completeness, it is kept in the denominator. The quasineutrality constraint, $n_e = n_i$, closes the equations, which reads in terms of the response functions, $\tilde{R}_{e/i} = \tilde{n}_{e/i} T_{0,e/i} / (n_0 |e| \Phi)$,

$$\frac{\tilde{R}_e}{1 + k_\perp^2 \rho_e^2} = \frac{\tilde{R}_i}{1 + k_\perp^2 \rho_i^2} \frac{T_{0,e}}{T_{0,i}} + \frac{k_\perp^2 \rho_s^2}{1 + k_\perp^2 \rho_i^2} \ . \tag{3.33}$$

Both electron and ion responses $\tilde{R}_{e/i}$ contain the plasma dispersion function $Z(\zeta - q)$. Since it has a pole at $\zeta - q$, further examination requires an approximation. To consistently preserve the required ordering at least a three-pole approximation for Z is necessary.

For this purpose, the three- and four-pole approximations, developed by Gregory Hammett and Francis Perkins [23], respectively:

$$Z_3(\zeta) = \frac{-i + i\Gamma + 2i\chi_1\mu_1 + 2\chi_1\zeta + 2\mu_1\zeta - i2\zeta^2}{\chi_1 - i\Gamma\zeta - 2i\chi_1\mu_1\zeta - 2\chi_1\zeta^2 - 2\mu_1\zeta^2 + i2\zeta^3} \ , \tag{3.34}$$

$$Z_4(\zeta) = \frac{i4D_1 + (10 + 4\beta_1)\zeta - 4iD_1\zeta^2 - 4\zeta^3}{3 + 2\beta - i6D_1\zeta - (12 + 4\beta_1)\zeta^2 + i4D_1\zeta^3 + 4\zeta^4} \ , \tag{3.35}$$

will be used in the numerical simulations in chapter 5. The parameters are chosen according to [23] as $\mu_1 = 0$, $\chi_1 = 2/\sqrt{\pi}$ and $\Gamma = 3$ for Z_3, and $D_1 = 2\sqrt{2}/(3\pi - 8)$ and $\beta_1 = (32 - 9\pi)/(6\pi - 16)$ for Z_4.

Expressing the plasma dispersion functions in terms of polynomials $\mathcal{P}$, the four-pole approximation becomes $Z_4 = \mathcal{P}_{Z,3}(\zeta)/\mathcal{P}_{Z,4}(\zeta)$, and $Z_3 = \mathcal{P}_{Z,2}(\zeta)/\mathcal{P}_{Z,3}(\zeta)$.

The kinetic density response function, based on (3.26), can be written as $R = \mathcal{P}_{R,1}(\zeta) + \mathcal{P}_{R,2}(\zeta)\, Z_u$. For kinetic electrons and kinetic ions, the adapted quasineutrality constraint, (3.33), gives, using the example of the four-pole approximation,

$$\frac{\mathcal{P}_{R_e,1} + \mathcal{P}_{R_e,2}\mathcal{P}_{Z_e,3}/\mathcal{P}_{Z_e,4}}{1 + k_\perp^2 \rho_e^2} = \frac{\mathcal{P}_{R_i,1} + \mathcal{P}_{R_i,2}\mathcal{P}_{Z_i,3}/\mathcal{P}_{Z_i,4}}{1 + k_\perp^2 \rho_i^2} \frac{T_{0,e}}{T_{0,i}} + \frac{k_\perp^2 \rho_s^2}{1 + k_\perp^2 \rho_i^2} \; .$$

To consider only the ordering of ζ, one approximates $k_\perp^2 \rho_{e/i}^2 \approx 0$ and $T_{0,e} \approx T_{0,i}$. After multiplication by the common denominator $\mathcal{P}_{Z_e,4} \cdot \mathcal{P}_{Z_i,4}$, the equation becomes

$$\mathcal{P}_{R_e,1} \cdot \mathcal{P}_{Z_e,4} \cdot \mathcal{P}_{Z_i,4} + \mathcal{P}_{R_e,2}\mathcal{P}_{Z_e,3} \cdot \mathcal{P}_{Z_i,4} = \mathcal{P}_{R_i,1} \cdot \mathcal{P}_{Z_e,4} \cdot \mathcal{P}_{Z_i,4} + \mathcal{P}_{R_i,2}\mathcal{P}_{Z_i,3} \cdot \mathcal{P}_{Z_e,4} \; .$$

The highest order of the polynomials appears to be nine, and thus, nine solutions of the dispersion relation seem to be expected. The same reasoning applied to the three-pole approximation gives a fifth order polynomial as the highest and, therefore, five expected modes.

However, based on the fact that the coefficients of the respective highest order polynomial in denominator and numerator of $Z_{3/4}$ are the same absolute value but opposite sign ("$\pm 2i$" in the three-pole approximation and "± 4" in the four-pole approximation), the actual number of solutions is reduced by one, becoming 8 for the four-pole approximation and 4 for the three-pole approximation. This fact is discussed and illustrated in section 5.1.2.

The model derived in this section contains drift kinetic electrons and drift kinetic ions and is supplemented by an ion polarization term and modified to include FLR effects. It forms the basis of the numerical analysis of drift waves in chapter 5.

3.3 Drift Parameter

The aim of this thesis is to study current-driven drift waves in fusion energy devices. To chose a realistic size of the parallel electron drift current, in this section the dimension of the drift parameter $v_{\|0}/c_s$ is estimated for Alcator C-Mod experiments. All drift wave models used in this work assume magnetostatics, which is a standard approximation for plasma waves with phase velocity $v \ll c$. Ampere's Law for the magnetostatic case

$$\nabla \times \mathbf{B} = \frac{4\pi}{c}\mathbf{j}$$

is the starting point for this general discussion. First, the shape of the tokamak (see section 2.5.1 fig. 2.6) is assumed to be a circle. After integration over the cross section and using Stoke's theorem,

$$\oint \mathbf{B}\ d\mathbf{l} = \frac{4\pi}{c}\int\limits_0^{r'} 2\pi r'\mathbf{j}(r')\ ,$$

the poloidal magnetic field can be written as

$$r\mathbf{B}_p = \frac{4\pi}{c}\int\limits_0^{r'} r'\mathbf{j}(r')\ . \tag{3.36}$$

The safety factor indicates how many times a magnetic field line toroidally goes around the torus for one time around poloidally:

$$q = \frac{r}{R}\frac{B_T}{B_p}\ .$$

As an established quantity q is used to represent the poloidal field in (3.36). Differentiating both sides of equation 3.36 with respect to r, the current becomes

$$j(r) = \frac{c}{2\pi}\frac{B_T}{qR}(1 - \frac{\hat{s}}{2})\ ,$$

where the magnetic shear is defined as $\hat{s} = \frac{r}{q}\partial_r q$. Using $u_{\|0} = j/(ne)$, the drift parameter is

$$\frac{u_{\parallel 0}}{c_s} = \frac{1}{nec_s}\frac{c}{2\pi}\frac{B_T}{Rq}(1-\frac{\hat{s}}{2}) \ . \tag{3.37}$$

In the next step non-circularity is allowed in order to state the drift parameter more precisely. Numerical studies showed [46] that for moderately shaped plasmas the current enclosed inside a flux surface with width r can be modeled as

$$I(r) = \frac{c}{2}\frac{r^2 B_T}{qR}\frac{1+\kappa^2}{2} \ , \tag{3.38}$$

with the elongation κ. As a simple approximation,

$$I(r) \approx \int\limits_0^r 2\pi r' \kappa(r') j(r') \tag{3.39}$$

will be used. Repeating the steps leading to (3.37), equation 3.38 is inserted in (3.39), both sides are differentiated with respect to r and the drift parameter becomes

$$\frac{u_{\parallel 0}}{c_s} = \frac{1}{nec_s}\frac{c}{2\pi}\frac{B_T}{qR}\left[1-\frac{\hat{s}}{2}+\frac{\kappa^2 s_\kappa}{1+\kappa^2}\right]\frac{1+\kappa^2}{2\kappa} \ , \tag{3.40}$$

where $s_\kappa = (r/\kappa)\partial_r \kappa$.

$\bar{n}_e$ (10^{20} m^{-3})	0.34
R/a	3.115097
q	1.410419
$\hat{s}$	1.625332
κ	1.221334
s_κ	0.164005
a/L_{Ti}	3.612313
a/L_{Te}	3.451792
a/L_n	0.850856
T_i/T_e	0.385030

Table 3.1: Alcator C-Mod parameters - for the specific experiment this work is referring to (taken from Ref. [33]).

Using the Alcator C-Mod parameters for the specific experiment this work is referring to, listed in table 3.1, a toroidal magnetic field of $B = 5.2$T, an electron temperature of 1keV and a minor radius of $a = 22$cm [22], the drift parameter (3.40) becomes

$$\frac{u_{\|0}}{c_s} \approx 2.09279 \ ,$$

predicting that the electron drift current can become about two times higher than the ion sound speed. In the large aspect ratio circular limit (3.37), the drift parameter is

$$\frac{u_{\|0}}{c_s} \approx 1.34612 \ ,$$

and in the non-circular limit (3.40), but neglecting the magnetic shearing, $\hat{s} = 0$, it becomes

$$\frac{u_{\|0}}{c_s} \approx 8.04947 \ ,$$

which is about four times higher than the original value including the shear parameter.

Due to uncertainties in the values of $\hat{s}$ and other shaping effects, such as the Shafranov shift, larger values of the drift parameter $u_{\|0}/c_s$ are possible. Also, the drift parameter may be larger if one considers locations in the plasma closer to the plasma center, where the magnetic shear is lower, or when considering other experiments at lower density or in smaller tokamaks. Even if the parallel electron drift current is not high enough in most parts of the plasma, magnetohydrodynamic (MHD) instabilities can possibly drive large local current densities at resonant surfaces, which might generate current-driven drift waves as secondary instabilities.

Thus in chapter 5 results for $u_{\|0}/c_s = 2.09279$, as well as for $u_{\|0}/c_s = 8.04947$

will be shown in order to demonstrate the sensitivity to a range of values and whether $u_{\|0}$ is possibly big enough to have a significant effect on growth rates.

3.4 Analytic Discussion of Drift Wave Instabilities

The model derived in section 3.2.2 for drift waves with kinetic electrons and fluid ions will be analytically analyzed in detail. Landau's method will be used to solve the integral in the plasma dispersion function Z (3.25). Assuming $\omega \sim \zeta$ has a small positive imaginary part, the integral in Z is evaluated along an integration path distorted around the pole as shown in figure 3.8.

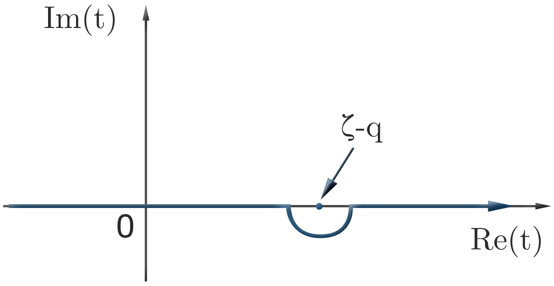

Figure 3.8: Integration path - Integration of t along the real axis, except using Landau's method for integration around the pole at $t = \zeta - q$.

For the analytic discussion

$$\omega \ll k_z v_{te} \tag{3.41}$$

is assumed. As the classic drift wave ordering is

$$v_{ti} \ll \frac{\omega}{k_\|} \ll v_{te} \ ,$$

assumption (3.41) is reasonable. With this assumption, the contribution from the pole exceeds the contribution from the real axis [18], allowing one to neglect the principal value and solve the problem with residues. Calculating the pole contribution with (3.41) and assuming that the parallel electron drift velocity

$u_{e0} = u_{\|0}$ is much smaller than the electron thermal velocity $u_{e0} \ll v_{te}$, gives

$$\begin{aligned} Res\left(\frac{1}{\sqrt{\pi}}\int\limits_{-\infty}^{\infty}\frac{e^{-t^2}}{t-(\zeta-q)}dt\right) =& i\sqrt{\pi}e^{-(\zeta-q)^2} \\ \approx& i\sqrt{\pi}\ . \end{aligned} \tag{3.42}$$

That $u_{e0} \ll v_{te}$ for real fusion devices is shown in section 3.3, where the drift parameter is estimated for Alcator C-Mod parameters. Inserting (3.42) in (3.30), the dispersion relation in this regime becomes

$$\begin{aligned} &1-\zeta_*\left[\eta(\zeta-q)+2\eta_u q\right]-\left[\frac{\zeta_*}{\zeta}-\rho_s^2k_\perp^2+\frac{1}{2\mu^2\zeta^2}\right] \\ =&-i\sqrt{\pi}\left[\zeta-q-\zeta^*\left(1-\eta\left[\frac{1}{2}-\zeta^2+2q\zeta-q^2\right]-\eta_u\left[2q^2-2q\zeta\right]\right)\right]\ . \end{aligned} \tag{3.43}$$

In the following the calculated dispersion relation (3.43) will be analyzed to give predictions about the behavior of drift waves in presence of an electron current drift and used to examine the influence of temperature gradients on drift waves.

Assuming a density gradient, but neither temperature gradient ($\eta = 0$) nor parallel electron drift ($q = 0$, $\eta_u = 0$), the dispersion relation (3.43) simplifies to

$$\omega(1+\rho_s^2k_\perp^2)-\omega_*-\frac{k_z^2c_s^2}{\omega} = -i\sqrt{\frac{\pi}{2}}\frac{\omega(\omega-\omega_*)}{|k_z|v_t}\ . \tag{3.44}$$

Figures 3.10 and 3.11 illustrate equation 3.44 for Alcator C-Mod parameters (see table 3.1). By ignoring the imaginary term and solving the quadratic equation on the left hand side, two solutions exist, as illustrated in figure 3.9. In the limit $\rho_s k_\perp \ll 1$ and $c_s k_z \ll \omega_*$ the frequency of the drift wave is the electron diamagnetic frequency $\omega \approx \omega_*$, as predicted in section 3.1. Since ω_{*e} is defined to be positive, the branch in the upper half plane is called the "electron branch", while the mode with the opposite sign is the ion branch.

Including the other terms as small corrections, the solution corresponding to the

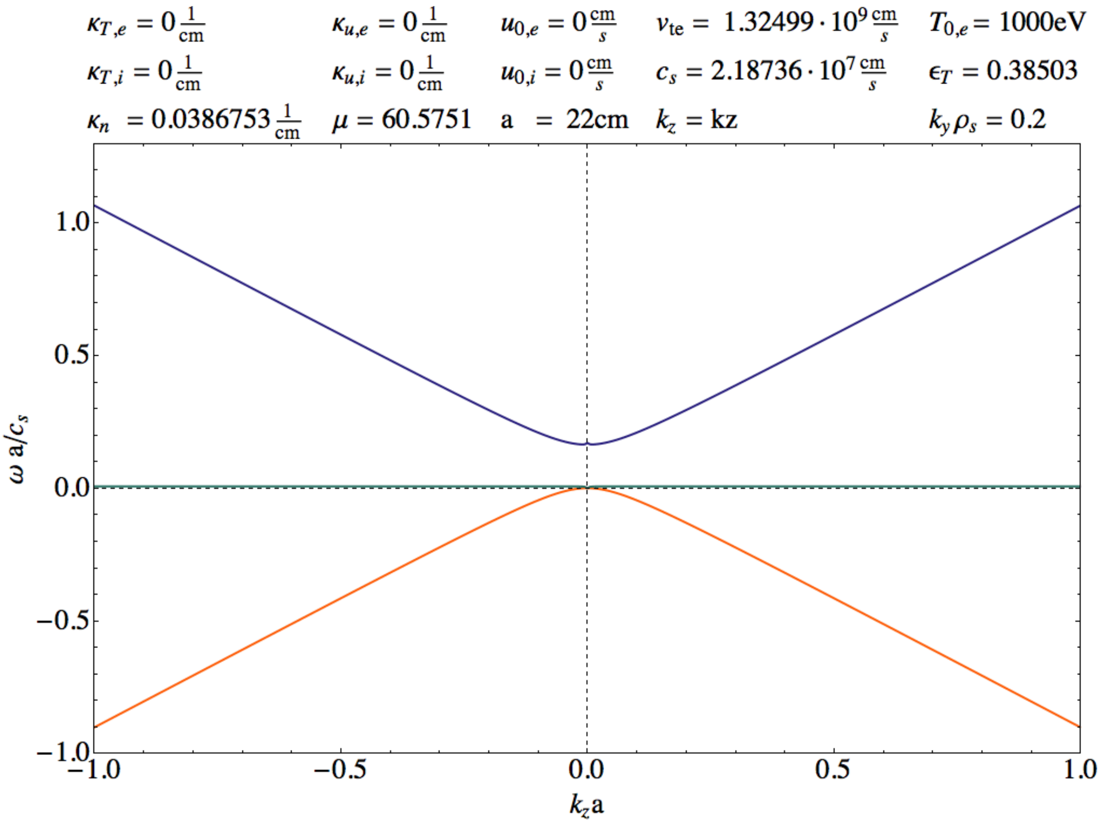

Figure 3.9: Frequency versus parallel wave vector - The branches approach the assymptotes $\omega = \pm k_z c_s$.

electron branch in figure 3.9 is

$$\omega_r = \omega_*(1 - \rho_s^2 k_\perp^2) + \frac{c_s^2 k_z^2}{\omega_*} \ .$$

To evaluate the growth rate of this drift wave, ω in (3.44) is replaced by $\omega \to \omega_r + i\gamma$. Taking the imaginary part and assuming the same approach as before for the real part, the growth rate is in this range

$$\gamma \approx \sqrt{\frac{\pi}{2}} \frac{\omega_*^2}{|k_z| v_{te}} \left(k_y^2 \rho_s^2 - \frac{k_z^2 c_s^2}{\omega_*^2} \right) \ . \tag{3.45}$$

Thus the stability threshold in this limit is

$$k_y^2 \rho_s^2 > \frac{k_z^2 c_s^2}{\omega_*^2} \ .$$

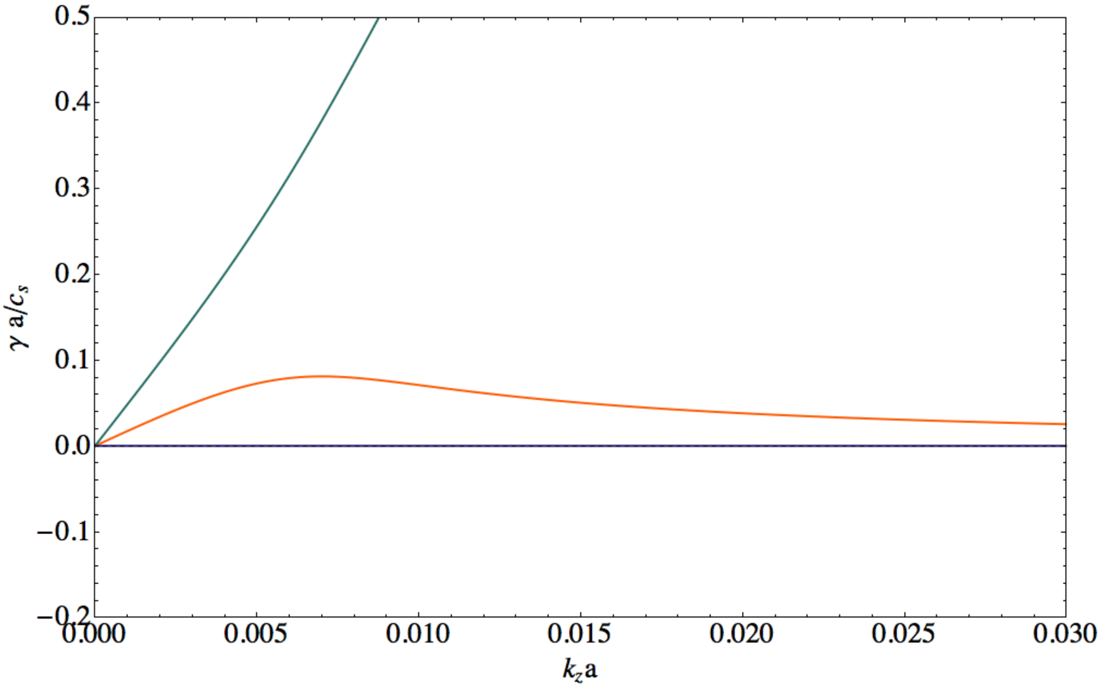

Figure 3.10: Growth rate versus ak_z according to (3.44) - Plot of the simplified dispersion relation (3.44) with $T_{0,e} = 1\text{keV}$, $\kappa_n = -0.0386753\,\text{cm}^{-1}$, $\kappa_T = 0$, $u_{0,e} = 0$ and $k_y \rho_s = 0.6$. This plot corresponds to figure 3.11, which shows the mode with the same parameters in perpendicular direction. The purely growing mode, depicted in green, is unphysical (i.e. it violates the assumptions used to get this analytic dispersion relation) and will be ignored in further considerations.

A more realistic treatment includes an electron temperature gradient. By ignoring terms $\sim \omega^2\omega_*$, setting $q = 0$ and $\eta_u = 0$, equation 3.43 simplifies to

$$\omega(1 + \rho_s^2 k_\perp^2) - \omega_* - \frac{k_z^2 c_s^2}{\omega} = -i\sqrt{\frac{\pi}{2}}\frac{\omega(\omega - \omega^* \left[1 - \eta/2\right])}{|k_z| v_{t,e}} \ . \tag{3.46}$$

After solving the dispersion relation 3.46 with nonzero η in the same limit as above, the growth rate is

$$\gamma = \sqrt{\frac{\pi}{2}}\frac{\omega_*^2}{|k_z| v_{te}}\left(k_y^2\rho_s^2 - \frac{k_z^2 c_s^2}{\omega_*^2} - \eta\right) \ , \tag{3.47}$$

which corresponds to (3.45) with an additional term $\sim \eta$. Since in most cases the gradients of density and temperature are of the same sign, η is assumed to be positive. Thus the temperature gradient is stabilizing and the instability threshold shifts to a higher value.

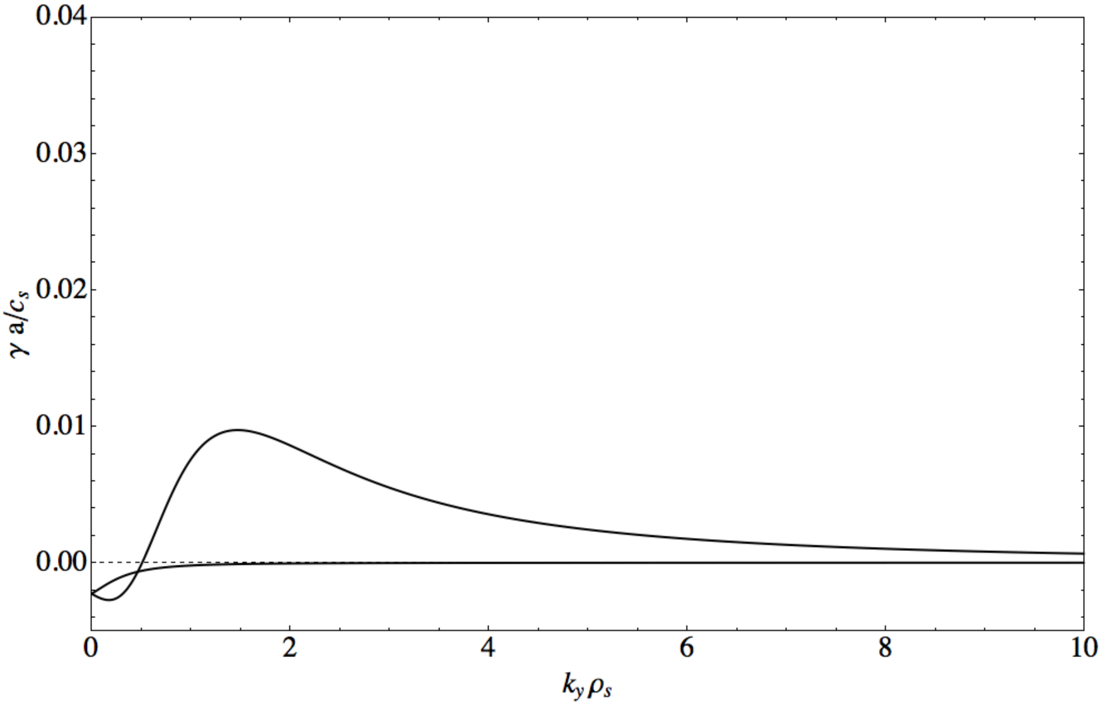

Figure 3.11: Growth rate versus $k_y\rho_s$ according to (3.44) - Plot of the simplified dispersion relation (3.44) with $T_{0,e} = 1\,\mathrm{keV}$, $T_{0,i}/T_{0,e} = 0.38503$, $\kappa_n = -0.0386753\,\mathrm{cm}^{-1}$, $\kappa_T = 0$, $u_{0,e} = 0$ and $k_z = 0.01\,\mathrm{cm}^{-1}$.

Using Alcator C-Mod parameters for the experiment this work is focussing on

[33], $T_{0,e} = 1\text{keV}$, $k_y\rho_s = 0.6$, and $1/L_n = \kappa_n = 0.0386753$, for $\eta = 0$ and $k_z = 0.01\text{cm}^{-1}$ the mode is stable according to (3.47) within the range of $|k_y\rho_s| < 0.51$. Adding a temperature gradient, $\eta = 4.06$, the range of stability extends to $|k_y\rho_s| < 2.02$.

The same approximation can be done for the case of an additional parallel electron current u_0. After evaluating the dispersion relation in the assumed limit, the growth rate is

$$\gamma = \sqrt{\frac{\pi}{2}}\frac{\omega_*^2}{|k_z|v_{te}}\left(-\frac{k_z^2c_s^2}{\omega_*^2} - \eta + \frac{k_z u_0}{\omega_*}\right) \ . \tag{3.48}$$

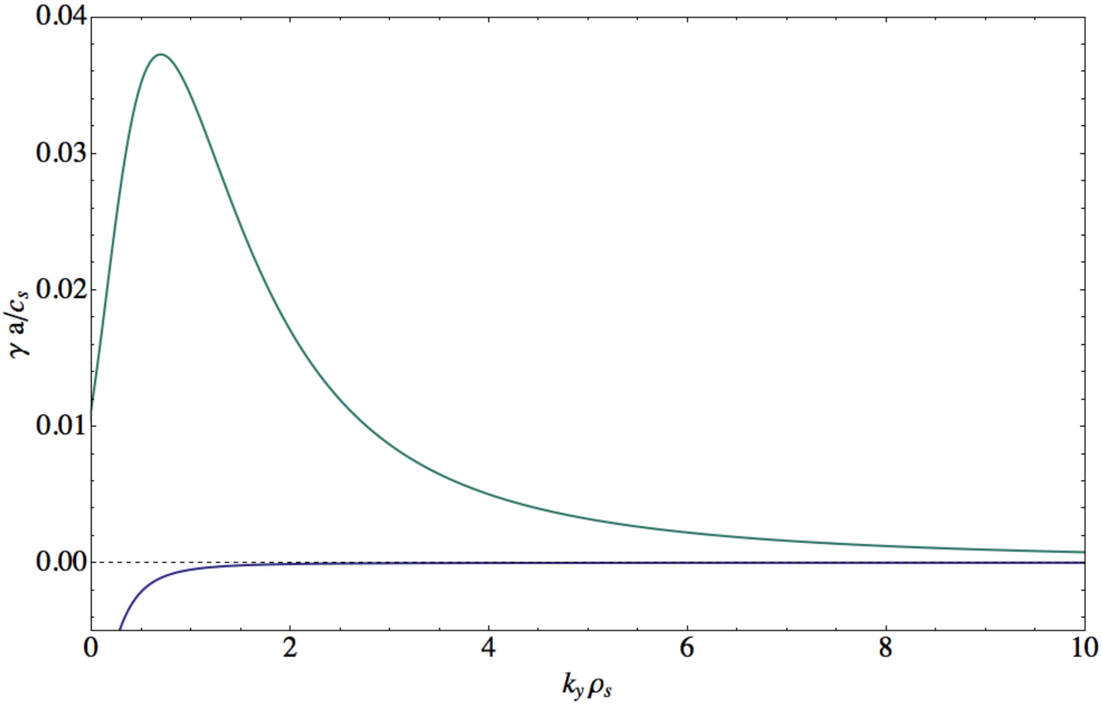

Figure 3.12: Growth rate of the CDDW versus $k_y\rho_s$ - Plot of the simplified dispersion relation with $T_{0,e} = 1\text{keV}$, $\kappa_n = -0.0386753\,\text{cm}^{-1}$, $\kappa_T = 0$, $u_{0,e} = -1.3124210^8\,\text{cm}\,\text{s}^{-1} = -6c_s$ and $k_z = 0.01\,\text{cm}^{-1}$. In order to plot positive $k_y\rho_s$-values, the electron current was chosen to be negative. As predicted in (3.48), the drift wave is driven more unstable by the electron current. The corresponding drift wave without the current is shown in figure 3.11. This CDDW is depicted in the parallel direction in figure 3.13.

If ω_* and $k_z u_0$ have the same sign, a parallel electron current is destabilizing, which can be seen by comparing figures 3.12 with 3.11 and 3.13 with 3.10. Recapitulating, this prediction is based on a model that includes fluid ions and kinetic electrons and depends on the classic drift wave ordering $\omega/k_{\|} \ll v_{te}$ with the additional limits $\rho_s k_\perp \ll 1$ and an electron streaming speed $u_{e0} \ll v_{te}$. To calculate (3.48), $c_s k_z \ll \omega \approx \omega_*$ is assumed, keeping only terms to order $k_z^2 c_s^2/\omega_*^2$, while $k_y^2 \rho_s^2$ corrections are neglected.

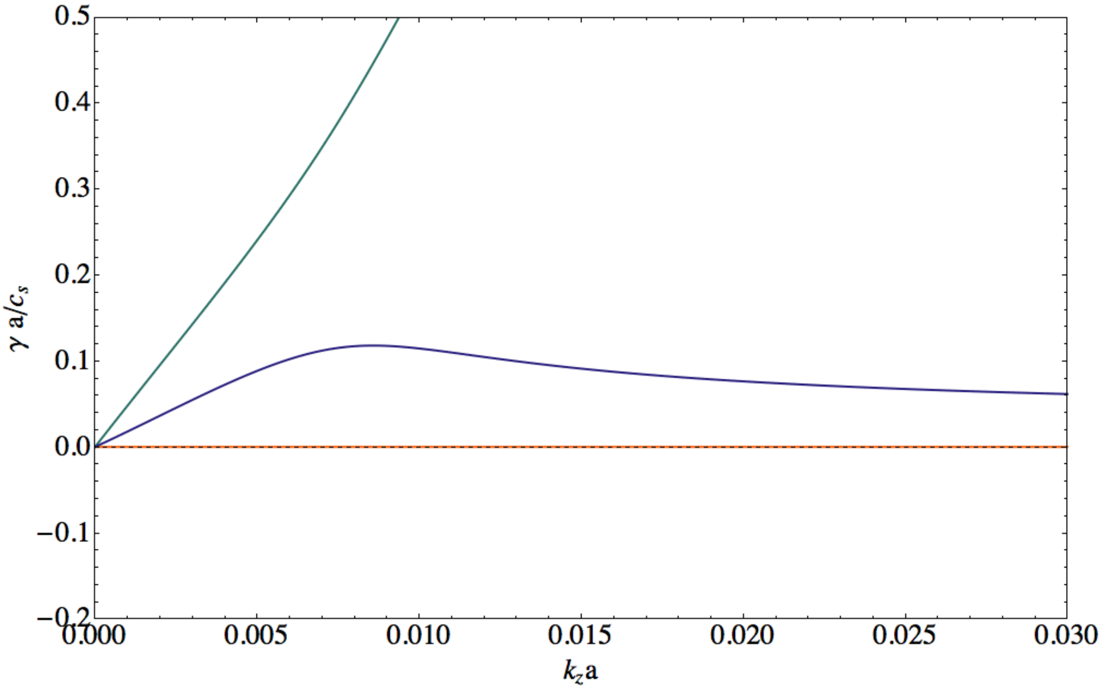

Figure 3.13: Growth rate of the CDDW versus ak_z - Plot of the simplified dispersion relation with $T_{0,e} = 1\text{keV}$, $\kappa_n = -0.0386753\,\text{cm}^{-1}$, $\kappa_T = 0$, $u_{0,e} = 1.31242 \cdot 10^8\,\text{cm}\,\text{s}^{-1}$ and $k_y \rho_s = -0.6$. This plot corresponds to figure 3.12, where the perpendicular direction is shown. Like in figure 3.10, the green line is unphysical.

Calculating the instability threshold $\gamma > 0$ in this limit as a function of k_z, two conditions have to be met:

$$2c_s\sqrt{\eta_e} < u_{0,e} \tag{3.49}$$

$$\frac{\omega_*(u_{0,e} - \sqrt{u_{0,e}^2 - 4c_s^2\eta_e})}{2c_s^2} < k_z < \frac{\omega_*(u_{0,e} + \sqrt{u_{0,e}^2 - 4c_s^2\eta_e})}{2c_s^2} .$$

The first condition states that the electron temperature gradient η_e has to be smaller than the quotient of electron streaming velocity and ion sound velocity squared, $\eta_e < (u_{0,e}/2c_s)^2$, to allow the current-driven drift wave to be unstable. Inserting the highest approximated drift parameter (see 3.3) $u_{e\|}/c_s \approx 8$, the threshold for η_e is according to 3.49

$$\eta_e < (u_{0,e}/2c_s)^2 \approx 16 \ . \tag{3.50}$$

For the Alcator C-Mod parameters, used in the plots above, $\eta_e = 4.05685$ and accordingly the condition (3.50) is met. The lowest drift parameter leading to current-driven drift waves according to this simple model is $u_{0,e}/c_s = 4.02832$ for the specific value of $\eta_e = 4.05685$.

The predictions about current-driven drift waves given in this chapter are verified in a model containing drift kinetic electrons and drift kinetic ions in section 5, where an additional temperature gradient for ions is added.

4

Program for Drift Waves Properties

In this chapter a program is described that can be used to examine drift waves numerically in more detail. It is written in "Wolfram Mathematica 7", which is further referred to as "Mathematica". First, the drift wave models that are provided in the program are recapitulated in the section "model". The design of the program is described in detail in the section of the same name, which covers input parameters, the use and interaction of functions, as well as the mode of operation of the program as a whole. The application of the program to the study of drift waves is provided in chapter 5.

4.1 Model

Multiple models exist in the program for increased flexibility and ease when studying drift waves in the plane plasma slab. The most advanced model used in this thesis is based on kinetic electrons and kinetic ions. It is described in detail in section 3.2.3. For standard use, the four pole approximation [23] for the plasma dispersion function is provided with the possibility to switch to the three pole approximation. The dispersion function for this model is called "disprel2". In table 4.1 the dispersion function together with the expected number of solutions are specified.

The second model uses kinetic ions and adiabatic electrons. Its dispersion relation is called with “disprel1”. Instead of the 8 expected modes when describing all species as kinetic, with adiabatic electrons 4 solutions exist.

In order to compare the numerical results with the analytic approximation, the dispersion relation for fluid ions and simplified kinetic electrons, used in section 3.4 for the analytic discussion, is “disprel0”. To allow the testing of concrete analytic results, manually defined growth rates can be plotted together with “disprel0”.

	3-pole approx.	**4-pole approx.**
kinetic ions, adiabatic electrons	disprel1 dim=3	disprel1 dim=4
kinetic ions, kinetic electrons	disprel2 dim=6	disprel2 dim=8
fluid ions, (simplified) kinetic electrons	disprel0 dim=3	

Table 4.1: Drift wave models contained in the program - The program provides three models for drift waves, which can be called with the listed internal names. For example, “disprel2” calls the dispersion relation describing electrons and ions kinetically. Besides the internal names, the corresponding number of solutions, denoted as “dim”, is shown.

4.2 Design

The program is designed in six parts. The first part contains the functions needed to calculate, plot, and save the results to the corresponding filesystem. The input parameters, listed in table 4.2, are provided in the following section. The user is able to choose electron $T_{0,e}$ and ion temperature via the relation $T_{0i} = \epsilon_T T_{0,e}$, as well as the density, temperature and velocity gradient via the parameters κ_n, κ_T and κ_u. Temperature- and velocity-gradients, and a parallel velocity u_0 are separately defined for both electrons and ions.

In the next section, analytically calculated γ is provided for comparison with the numerical results. The main calculation is done in part 4, where the electron and ion response functions are calculated. In the following part these response functions are combined into a dispersion relation. In the last section, the functions are called to finally calculate growth rate, frequency or diffusivity, to plot the solutions and save them into an externally saved file.

4.2.1 Input Parameter

All global variables, for example the minor radius a, are given the prefix "var", and every function has the prefix "fct". Since some functions are called without arguments, this convention clarifies their type in the program sequence.

The physical input parameters are defined in the program section "Input Parameter". Non-constants are specified in the sections "Parameters I" and "Parameters II". In the first parameter section, the minor radius a of the experimental device, $vara$, which is only used for normalization, and the ions' and electrons' temperatures are defined. While the electron temperature is defined by its own variable, "varTe", the ion temperature is represented by "varϵ_T", the ratio of the ions' to the electrons' temperature, $\epsilon_T = \frac{T_{i0}}{T_{e0}}$.

The second parameter block, "Parameters II", specifies the most frequently varied parameters. The gradients, bulk velocities and wave numbers can be chosen in a list. All plots require a non-zero density gradient and k_z. Every gradient is represented by $\kappa_x = 1/L_x$, which is defined as $d_r x/x$. For example $\kappa_n =$

$d_r n/n = 1/L_n$. Temperature- and velocity-gradients, as well as an additional parallel velocity u_0 are separately defined for both electrons and ions. Table 4.2 shows the provided input parameters with their definitions.

Parameter	**Global Variable**	**Definition**
a	vara	Inner radius
$T_{0,e}$	varT0e	Electron temperature in eV
κ_{Ti}		$1/L_{Ti} = d_r T_{0,i}/T_{0,i}$
κ_{u0i}		$1/L_{ui} = d_r u_{0,i}/u_{0,i}$
$u_{0,i}$		Ion parallel velocity
κ_{Te}		$1/L_{Te} = d_r T_{0,e}/T_{0,e}$
κ_{u0e}		$1/L_{ue} = d_r u_{0,e}/u_{0,e}$
$u_{0,e}$		Electron parallel velocity
κ_n		$1/L_n = d_r n_0/n_0$
k_z		Parallel wave vector
$k_y \rho_i$		Normalized perpendicular wave vector
ϵ_T	varϵT	$T_{0i}/T_{0,e}$
m_i	varmiD	Mass deuterium
m_p	varmp	Mass proton
m_e	varme	Mass electron
μ	varmu	$\sqrt{m_i/m_e}$
v_{ti}	varvti	$\sqrt{T_i/m_i}$; Ion thermal velocity
v_{te}	varvte	$\sqrt{T_e/m_e}$; Electron thermal velocity
c_s	varcs	$\sqrt{T_e/m_i}$; Ion sound velocity

Table 4.2: Input parameters of the program - The input parameters are defined in the section "Input Parameter". The first column, "Parameter", states the name of the physical parameter, while the second one names the corresponding internally used global variables.

4.2.2 Functions

In order to give the user the opportunity to plot growth rate, frequency and diffusivity versus different parameters, while reducing lines of code and runtime, the program is built modular. The variables, which are automatically used as plotting variables, are depicted in table 4.3.

Function	γ, f, D_{mix}
2D	$k_{\|}$, $k_{\perp}$, $u_{0,e}$, $\kappa_{T,e}$, $\kappa_{T,i}$, κ_{ue}
3D	$k_{\|}$ & $k_{\perp}$

Table 4.3: Physical quantities to evaluate - By default, the growth rate, γ, frequency, f, and diffusivity D_{mix} are calculated and plotted as a function of one of the parameters of the second row. Three dimensional plots are provided versus $k_{\perp}$ and $k_{\|}$.

The functions can be classified in four groups. The first group contains functions that set parameters for the list of values and clean up after using variables. The next group contains functions that logically determine the paths of directories in which to save images. The most important functions are the ones that actually calculate and store the values for plotting, which is done in the last group. In the following sections an overview of the functionality of the program is given and some important functions are described in detail.

Functions for setting parameters

The dispersion relation is first calculated with symbolic variables. Then, the variables are replaced with values to numerically solve the equation. To insert the chosen parameters (see section 4.2.1), lists are constructed. Each list contains the values or the variables in the following order:

`valueList` = $\{\kappa_{Ti}, \kappa_{ui}, u_{0,i}, k_y\rho_s, c_s, \kappa_{Te}, \kappa_{ue}, u_{0,e}, T_{0,e}, \epsilon_T, \kappa_n, \mu, k_z, \omega\}$.

Listing 4.1: valueList - The list “valueList” shows the ordering of the parameters.

The function “fctSetValueList” constructs these lists, which are later called by other functions in order to replace the variables with values. Since it is useful to allow later plotting of the calculated growth rate, frequency or diffusivity versus different parameters, for every designated abscissa there is one list defined. The list for plotting versus k_z for example is constructed as follows, where both k_z

and ω stays as variable and the others are replaced by their values:

```
fctSetValueList[var1_, var2_, var3_, var4_, var5_, var6_, var7_,  var8_, var9_] :=
Module[{},
valueListkz =
  {(*\[Kappa]Ti*)var1,
   (*\[Kappa]ui*)var2,
   (*u0i*)var3,
   (*kyrhos*)var4/Sqrt[varepsT],
   (*cs*)varvte/varmu,
   (*\[Kappa]Te*) var5,
   (*\[Kappa]ue*)var6,
   (*u0e*)var7,
   (*T0e*)varT0e,
   (*\[Epsilon]T*) varepsT,
    (*\[Kappa]ni = \[Kappa]ne*) var8,
   (*\[Mu]^2*) varmu,
   (*kz*) kz,
   (*\[Omega]*) ω]}
  ...
  ...
]
```

Listing 4.2: fctSetValueList - This function constructs the lists that provide the values for insertion into the dispersion relations.

Each time that a value in the input parameter section is changed and the corespondent cell is evaluated, “fctSetValueList” is called to renew the list of values, which are needed to calculate and plot the results.

Functions to determine the path

For further analysis, the plots are saved into files. To be able to easily find plots of different parameters, there is a designated folder structure, in which the plots are automatically sorted. An example is shown in figure 4.1.

The first layer, “0”, “e”, “i” or “ei”, sorts the plots, depending on which group of parameters of the correspondent list of values are nonzero: if $\kappa_{T,x}$, $\kappa_{u,x}$ and $u_{0,x}$ are zero for both electrons and ions (x indicates the particle species), the folder “0” is active. If the named parameter group is zero for ions, but at least one of

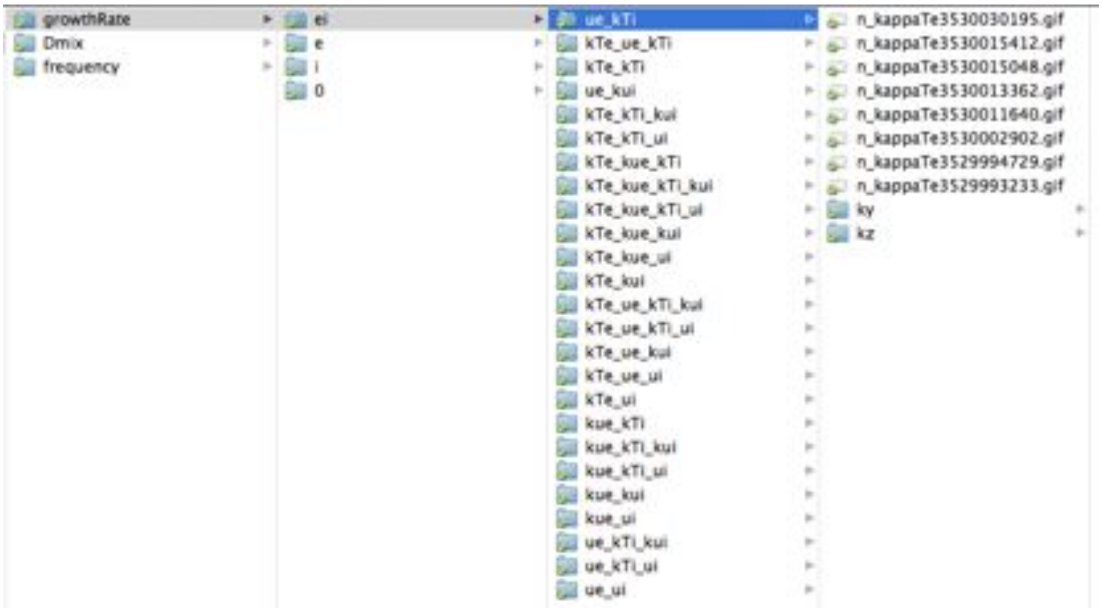

Figure 4.1: Folder structure - The plots are automaticaly saved into folders according to their parameters.

the parameters is nonzero for electrons, "e" is chosen, vice versa, "i". For at least one nonzero parameter for both, electrons and ions, the files are stored in "ei".

The second layer distinguishes the single parameters for electrons and ions. The folders are named after the nonzero variables, for example "kTe_kue" for nonzero κ_{Te} and κ_{ue}.

The most interesting plots probably are the ones versus parallel and perpendicular wave vectors, so in the last layer there are the two folders "ky" and "kz" for plots versus perpendicular and parallel wave numbers. The described distribution of the plots is done in the two functions "fctDirEI" and "fctdirmulti", called by the top function "fctDirPath", as illustrated in figure 4.2.

The return value of "fctDirPath" is a String, composed of the structure of the directories, where the file is to be saved, for example "e/ue/kz". The first layer is computed by "fctDirEI", which is called with the list of values as argument, whose construction was previously described. It returns the first layer, "0", "e", "i" or "ei".

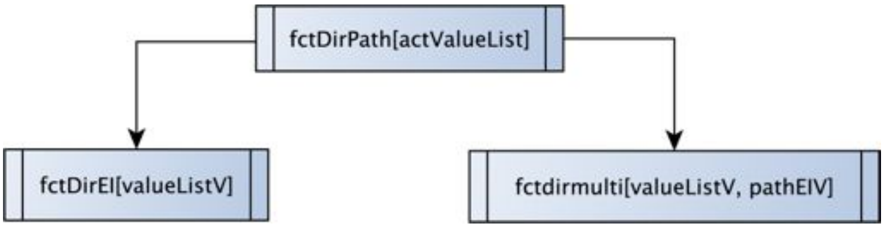

Figure 4.2: Functions, indicating the path for saving - The output string defines the path, where the output plot is saved.

The second function “fctdirmulti” returns layer two and three combined, such as “ue/kz”.

Calculation of growth rate, frequency and diffusion

The calculation of the actual results for growth rate, frequency or diffusion is done numerically. The starting point is the dispersion relation and the array of values described in section 4.2.2. Figure 4.3 shows the interaction of the functions, which provide together the designated results.

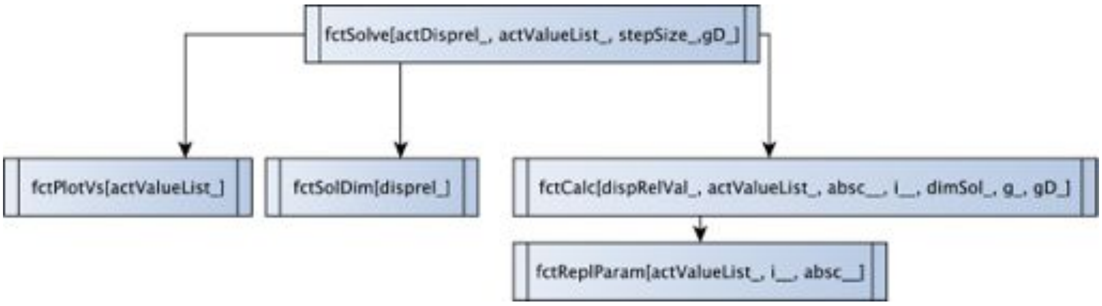

Figure 4.3: Functions for solving - The function “fctSolve” calls as master function the subfunctions “fctPlotVs”, “fctSolDim” and “fctCalc”, which in turn calls “fctReplParam”. Together they calculate the growth rate γ, frequency f and Diffusion D out of a given dispersion relation.

The function “fctSolve” is the master function of the calculation. It provides loops for the numerical calculation, one for two dimensional and two loops for the three-dimensional case, as can be seen in the code-fragment 4.3. The input parameters are: “actDisprel”, the name of the dispersion relation to be used;

“actValueList”, the name of the list of values, which implicitly gives the abscissa; “stepSize”, which is used in calculating numerical solutions; and a variable called “gD”, which contains information about the designated result.

```
1  fctClearAll;
2  fctSolve[actDisprel_, actValueList_, stepSize__, gD_] := Module[
3     {gdaAtemp1, gdaAtemp2, solArray, dispRelVal, ikz, iky, solArrayGes,
4       p, solDim, plotDim, i1, absc, iboth},
5     dispRelVal = Apply[actDisprel, actValueList];
6     solDim = fctSolDim[ToString[actDisprel]];
7     absc = fctPlotVs[actValueList];
8     solArray = {}; solArrayGes = {}; p = 1; plotDim = 2;
9     If[Dimensions[stepSize][[1]] == 2, plotDim = 3];
10    If[plotDim == 2, (*2D*)
11     {For[i1 = stepSize[[1]], i1 < stepSize[[2]], i1 = i1 + stepSize[[3]],
12        gdaAtemp2 = fctCalc[dispRelVal, actValueList, absc, i1, solDim[[1]], solDim[[2]], gD];
13        solArray = Join[solArray, {gdaAtemp2}]
14        ];
15      },
16     If[plotDim == 3,(*3D*)
17       {For[ikz = stepSize[[1,1]], ikz < stepSize[[1,2]], ikz = ikz + stepSize[[1,3]], {
18          For[iky = stepSize[[2,1]], iky < stepSize[[2,2]], iky = iky + stepSize[[2,3]], {
19             iboth = {ikz, iky};
20             gdaAtemp2 = fctCalc[dispRelVal,actValueList,absc,iboth, solDim[[1]], solDim[[2]], gD];
21             solArray = Join[solArray, {gdaAtemp2}];
22             }
23            ];
24          }];
25        },
26       {Print["Error in Dimensions. Allowed: 2D and 3D"]; Abort[];}
27         ];];

29    While[p <= solDim[[1]],
30     solArrayGes = Join[solArrayGes, {solArray[[All, p]]}];
31     p++;
32     ];
33    solArrayGes
34    ];
```

Listing 4.3: fctSolve - The function “fctSolve” provides the loop for numerical calculation of the growth rate gamma γ, frequency f or Diffusion D. The result is a multidimensional array of the calculated values.

The function “fctSolDim”, called in listing 4.3, line 6, is shown in the code fragment 4.4. It provides the number of solutions according to the given dispersion relation, as well as the type: “$g = 0$” are already given growth rates with one solution, “$g = 1$” the simplified dispersion relations with three solutions, and “$g = 2$” the full dispersion relation with 4 or 8 solutions, depending on the use of the three- or four-pole approximation for the plasma dispersion function.

```
fctSolDim[disprel_] := Module[{solDim, g},
   If[disprel == "gammaan1", {solDim = 1; g = 0;}];
   If[disprel == "gammaan2", {solDim = 1; g = 0;}];
   If[disprel == "gammaan3", {solDim = 1; g = 0;}];
   If[disprel == "gammaan4", {solDim = 1; g = 0;}];

   If[disprel == "disprelan1", {solDim = 3; g = 1;}];
   If[disprel == "disprelan2", {solDim = 3; g = 1;}];
   If[disprel == "disprelan3", {solDim = 3; g = 1;}];
   If[disprel == "disprelan4", {solDim = 3; g = 1;}];
   If[disprel == "disprel0", {solDim = 3; g = 1;}];

   If[disprel == "disprelnu1", {solDim = 4; g = 2;}];
   If[disprel == "disprelnu2", {solDim = 8; g = 2;}];
   {solDim, g}
   ];
```

Listing 4.4: fctSolDim - The function “fctSolDim” provides the number of solutions and the type of a specific dispersion relation.

The function “fctSolDim” returns an array containing the number and type of solution. The number of the solutions is needed to optimize the array dimension of the solution and to design the graphics.

The second function, which is called in “fctSolve”, listing 4.3, is “fctPlotVs”, depicted in listing 4.5. It tests for every element of the actual list of values, if it is a number (“NumberQ”). Each non-numeric element is a variable against which the function will be plotted.

The generated information is used in “fctSolve” to calculate lists of solutions to be plotted later. The variable “dispRelVal” contains the list of values applied to the dispersion relation. The result is a function of only ω and the variables against which it will be plotted. For a two dimensional plot versus k_z for example, ω and k_z are indefinite. For a three-dimensional plot, k_y can also vary.

```
fctPlotVs[actValueList_] := Module[{p, dim, printVar},
  dim = Dimensions[actValueList][[1]]; p = 1; printVar = {};
  While[p < dim,
   If[! NumberQ[actValueList[[p]]], printVar = Join[printVar, {actValueList[[p]]}];];
   p++];
  printVar
  ]
```

Listing 4.5: fctPlotsVs - The function “fctPlotVs” returns the non-numerical parameters of the value list and so defines the variable for the numerical solution.

In the next step, the remaining variables, except for ω, are in a loop replaced by the values according to “stepSize”, a list containing start value, step size and stop value. For every step the function “fctCalc” is called, which gives an array of the solutions back. For three-dimensional case there are two loops, for each perpendicular and parallel k “fctCalc” is called once.

The actual calculation is done in the function “fctCalc”. The sequence of this function is shown in figure 4.4 and an example of the source code in listing 4.6. The first determination is related to the dispersion equation: depending on the value of g, which was discussed above in listing 4.4, different branches are chosen.

Subsequently, the value for the loop parameter is inserted and for the case of the dispersion relation, the equation is numerically solved. For the analytically calculated cases ($g = 0$ or $g = 1$) the next step is the evaluation of thresholds: The analytic calculation of the growth rate of drift waves in section 3.4 was based on the assumption $\omega \ll k_z v_{te}$. For this reason, the constraint $|\omega| < 0.05\ k_z v_{te}$ is tested. Only if $\omega = \omega_r + i\gamma$ is small enough, the desired quantity is calculated and added to the array of solutions. As illustrated in figure 4.4, the parameter gD switches between the growth rate, frequency or diffusion and thus initializes the calculation, shown in listing 4.6.

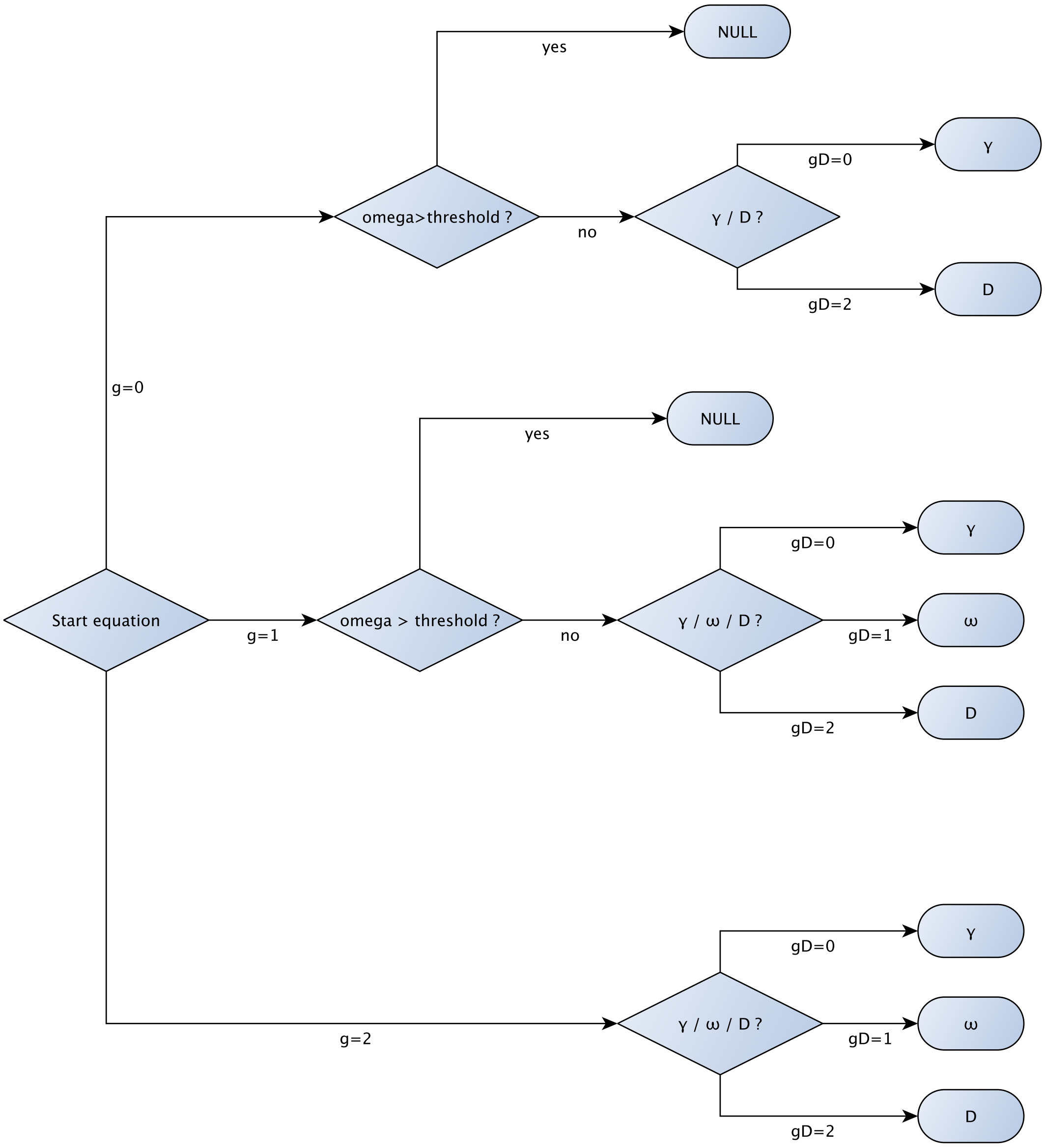

Figure 4.4: Sequence of the function "fctCalc" - In this function, depending on different parameters, the desired quantity (growth rate, frequency, or diffusion) is calculated. The parameter g chooses the equation to be evaluated: $g = 0$ is an already-calculated growth rate, $g = 1$ the analytically-calculated dispersion relation, and $g = 2$ the numerically-calculated dispersion relation. After the evaluation of the thresholds in the analytic cases, the parameter gD decides whether frequency, growth rate, or diffusion is calculated (see listing 4.6).

```
fctClearAll;
fctCalc[dispRelVal_, actValueList_, absc__, i__, dimSol_, g_, gD_] :=
  Module[
   {gdaAtemp1, gdaAtemp2, replParam, gdaAtemp3, ii},
   gdaAtemp1 = ConstantArray[0, dimSol];
   gdaAtemp2 = ConstantArray[Missing["NotAvailable"], dimSol];
   replParam = fctReplParam[actValueList, i, absc];

   For[ii = 1, ii <= dimSol, ii++,
    Switch[g,
      0, {(*0:gamma*)
         ...
       };
      1, {(*1:analytic*)
         ...
       };
      2, {(*2:numeric*)
       gdaAtemp1 := NSolve[(dispRelVal /.replParam[[1]]) == 0, \[Omega]] ;
       If[
        gD == 0, {(*growth rate*)
         gdaAtemp2[[ii]] = Flatten[{i,Im[\[Omega] /.gdaAtemp1][[ii]]/(varcs/vara)}]},
        If[gD == 1, (*frequency*)
         {
          gdaAtemp2[[ii]] = Flatten[{i,Re[\[Omega] /.gdaAtemp1][[ii]]/(varcs/vara)}];
          },
         If[gD == 2, (*Subscript[D, mix]*)
          {
           gdaAtemp2[[ii]] = Flatten[{i,Im[\[Omega] /.gdaAtemp1][[ii]]
                                  *((varrhos*10^-2)/replParam[[3]])^2}];
           },
          Print["Error in fctCalc!"]]]
        ];
       }
      ];
    ];
   gdaAtemp2
];
```

Listing 4.6: fctCalc - The actual calculation is done in the function "fctCalc." As shown in figure 4.4, depending on the desired quantity (frequency, growth rate, or diffusion) different branches are chosen. The calculation is performed using the Mathematica-built-in function "NSolve".

The function "fctReplParam" returns the replacement rules, used in "fctCalc" for solving the dispersion relation and scaling of the axes. In listing 4.7, "fctReplParam" is shown for the example case of "valueListky". The replacement parameter depends on the intended axis normalization.

```
fctReplParam[actValueList_, i__, absc__] :=
 Module[{dim, replParam},
  dim = Dimensions[absc][[1]];
  replParam = {};
  If[dim == 1, (*2D plot*)
    Switch[ToString[absc[[1]]],
      ...
      "kyrhos", replParam = {{kyrhos -> i}, Abs[actValueList[[13]]], i};,
      ...
      ];
    ]
   If[dim == 2,(*3D plot*)
    {replParam = {{kz -> i[[1]]/vara, kyrhos -> i[[2]]}, Abs[i[[1]]], i[[2]]};}
    ];
  replParam (*{param -> i}, |kz|, kyrhos*)
  ]
```

Listing 4.7: fctReplParam - The function “fctReplParam” returns the replacement rule, $k_y\rho_s$ and the absolute value of k_z.

With the information from “fctReplParam”, γ, f or D is calculated, stored in a list and given back to “fctSolve”, which combines all results in one array and returns it for use by plotting functions, which will be described next.

Functions for plotting

The master function for plotting of the just calculated list of results is “fctListPlot”. It calls the built-in function “ListPlot”, which plots a list of values. The function “fctValuesString”, called in “fctListPlot”, prepares the parameters for use as the figure label.

Information for plotting the different combinations of dispersion relations are stored in “fctAnNu”. Listing 4.8 shows an extract for the case of one numeric dispersion relation (“n”), while “a” depicts “disprel0”, “aa” the growth rate and “disprel0”, and “nn” both numerical solved dispersion relations.

```
fctAnNu[anNu_] := Module[{PlotStyleArray, legendArray, actDisprel},
   Switch[ToString[anNu],
    "aa", {...};
    "nn", {...},
    "an", {...},
    "a", {...},
    "n", {
     actDisprel := {disprelnu2};
     legendArray := {...};
     PlotStyleArray := {...}
     }
    ];
   {actDisprel, legendArray, PlotStyleArray}
   ];
```

Listing 4.8: fctAnNu - The function “fctAnNu” provides information for the plotting of the different dispersion relations.

Calculation of the maxima

The solutions (growth rate, frequency or diffusion) are stored in an array, as discussed previously. The function “fctReturnMax” finds the maximum of each mode and returns their coordinates in an array.

```
fctReturnMax[solutionsArray_] :=
  Module[{jj, maxArray, dim},
   maxArray = {};
   dim = Dimensions[solutionsArray][[1]];
   For[jj = 1, jj < (dim + 1), jj++, maxArray = Join[maxArray,
       Pick[solutionsArray[[jj]], #, Max[#]] &[Last /@ solutionsArray[[jj]]] // N
       ];];
   maxArray
   ];
```

Listing 4.9: fctReturnMax - The function “fctReturnMax” lists the maximum of each mode and stores the coordinates in an array.

4.2.3 Analytic Dispersion Relation

The analytically calculated growth rates and dispersion relations, discussed in detail in section 3.4, are provided in the program section with the name “Analytic Dispersion Relation and Growth Rates". The growth rates are defined as approximated in section 3.4, for example in equation 3.48. The dispersion relation consists of fluid ions and simplified kinetic electrons (3.46).

4.2.4 Electron and Ion Response

In this section the response of the particles via the drift kinetic equation is calculated, and approximations are provided for the plasma dispersion function and the additional ion polarization term. The theoretical concept of the model is described in section 3.2.3.

First, the perturbed ion density is calculated as shown in listing 4.10. After the declaration of local variables in line 3, physical variables like velocities and distribution functions are defined. In line 4 the $\mathbf{E} \times \mathbf{B}$ - velocity is written in Fourier space notation. The parallel and perpendicular velocities are defined separately to be able to upgrade the code to include other velocity components. The equilibrium distribution function f_0 is assumed to be Maxwellian. To simplify the derivatives in line 11, f_0 is defined as product of a prefactor with two probability density functions (PDFs). The first PDF is a normal distribution with mean 0 and standard deviation $v_t(x)$, evaluated at $v_\perp$. The second PDF is a normal distribution with mean u_0 and standard deviation $v_t(x)$, evaluated at $v_\|$.

The first step is the integration of the drift kinetic equation over $v_\perp$, which is done in "n1withoutIntvparallelF" in line 9, after replacing the gradients with the scalings L_n and η. In order to simplify the calculation, terms that include v_z are separated from whose, that do not contain v_z. Thus, v_z is set zero in "n1withoutIntvparallelnurZF". Additionally the term is multiplied by $-\omega$, since the denominator was $(v_z - \omega k_z)$.

```
n1kinetic[eV_, mV_, BV_, cV_, ϕV_, vtV_, ηV_, ηuV_, n0V_, T0V_, u0V_, ωsV_, kzV_, ωV_, ZV_] =
 Module[
   {x, y, z, vperp, vparallel, ky, kx, q, ζ, ζs, Ln, t, f1D, ue, uparal, f0, f1, n1withoutIntvparallelF,
        n1withoutIntvparallelnurZF, c, n1, f10, m, Φ , B, kz, e, vt, η, ηu, n0, T0, u0, ωs, ω, Z, phi,
        n1Value},
   ue := -I (c* phi)/B {ky, -kx, 0};
   uparal := {0, 0, vparallel};
   f0 := n0[x]/(Sqrt[2 Pi] vt[x])* PDF[NormalDistribution[0, vt[x]], vperp]
            *PDF[NormalDistribution[u0[x], vt[x]], vparallel];
   f1 := f10[x] E^(I (ky*y + kz*z  - ω * t));

   n1withoutIntvparallelF :=
    ReplaceAll[ Integrate[(Solve[ReplaceAll[
    (D[f1, t] + D[f1, z]*Part[ue + uparal, 3] + D[f0, x]*Part[ue + uparal, 1] -
              I e/m phi*kz* D[f0, vparallel]),
            {E^(I (ky y + kz z - t ω)) -> f1D/f10[x],
             n0'[x] -> n0[x]/ Ln, vt'[x] -> vt[x]*η/(Ln *2), u0'[x] -> u0[x]*ηu/Ln ,
             ky -> (e*B*Ln*ωs)/(c*T0[x]),
             m ->  T0[x]/(vt[x])^2}] == 0, f1D][[1, 1, 2]]*2*Pi*vperp),
     {vperp, 0, Infinity}, Assumptions -> (Re[vt[x]^2] > 0)],
     {u0[x] -> u0, n0[x] -> n0, vt[x] -> vt, T0[x] -> T0}];
   n1withoutIntvparallelnurZF =
    ReplaceAll[(E^(u0^2/(2 vt^2))*(-ω)*n1withoutIntvparallelF), vparallel -> 0]*
     E^(-((u0 - vparallel)^2/(2 vt^2)))/(kz vparallel - ω);

   n1 := Collect[(ReplaceAll[(E^(u0^2/(2 vt^2))*(-ω)*n1withoutIntvparallelF), vparallel -> 0]
             *Z*Sqrt[Pi]*kz^-1) +
      (Simplify[ReplaceAll[Expand[Simplify[
           n1withoutIntvparallelF - n1withoutIntvparallelnurZF]],
         {E^(-((u0 - vparallel)^2/(2 vt^2))) vparallel -> (kz vparallel - ω)*Sqrt[2*Pi]*vt*
             Abs[kz]^-1 + (kz vparallel - ω)*Z*ω*Pi^(1/2)* Abs[kz]^-2,
          E^(-((u0 - vparallel)^2/(2 vt^2))) vparallel^2 -> (kz vparallel - ω)*Sqrt[2*Pi]*vt*
             u0*Abs[kz]^-1 + (kz vparallel - ω)*Sqrt[2*Pi]*vt*ω*kz^-2 + (kz vparallel - ω)*
             Z*ω^2*Pi^(1/2)*Abs[kz]^-3}]]), Z];

   n1Value :=
    ReplaceAll[
     Collect[n1, {(e n0 Φ)/T0}], {e -> eV, m -> mV, B -> BV, c -> cV, phi -> ϕV,
      vt -> vtV, η -> ηV, ηu -> ηuV, n0 -> n0V,
      T0 -> T0V, u0 -> u0V, ωs -> ωsV, kz -> kzV, ω -> ωV, Z -> ZV}];
   n1Value
   ];
```

Listing 4.10: n1kinetic - The function “n1kinetic” provides the perturbed ion density, which is calculated out of the drift kinetic equation in a plane plasma slab geometry.

The perturbed density is calculated in “n1”. First, all terms without v_z are multiplied by $Z\sqrt{\pi}|kz|^{-1}$, where $Z = Z(\zeta - q)$ is the plasma dispersion function.

In all other terms, v_z and v_z^2 are replaced, leading to an expression in terms of $Z(\zeta - q)$. In order to insert values, the local variables are replaced at the end with the variables of the function called.

The resulting symbolic plasma response derived with Mathematica agrees with the analytic derivation in equation 3.26. In chapter 3, a negative density gradient was needed to shift the electron drift wave to positive frequencies. This minus sign is given in the parameters in the input section, where for example $\kappa_n = -0.0386753\text{cm}^{-1}$. The response function for electrons is called with:

```
n1kinetic[-e, m, B, c, Φ, vt, η, ηi, n0, T0, u0, -ωs, kz, ω, Z]
```

Listing 4.11: Call of "n1kinetic" - The perturbed density of electrons is achieved by the call of "n1kinetic" with $-e$ and $-\omega_s$.

The perturbed densities for adiabatic particles and the ion polarization density are defined after the perturbed density is calculated from the drift kinetic equation. Since Z is still contained in the kinetic response, the three- (3.34) and four-pole approximations (3.35) are declared to replace Z in the dispersion relation.

4.2.5 Dispersion Relation

As all terms are defined now, the dispersion relation is calculated. Two models are prepared: adiabatic electrons and kinetic ions, leading to "disprel1", and kinetic electrons and kinetic ions, called "disprel2". The following listing 4.12 shows the code fragment for "disprel2".

```
disprel2[κTiDRB1_, κuiDRB1_, u0iDRB1_, kyrhosDRB1_, csDRB1_, κTeDRB1_, κueDRB1_, u0eDRB1_,
              T0eDRB1_, ϵTDRB1_, κnDRB1_, μDRB1_, kzDRB1_, ωDRB1_] :=
  Module[
   {mi, vti, ηi, ηui, n0i, T0i, u0i, ωsi, kz, ω, dispRel, kyrhoi, e, B, c, ϕ, result, me, vte, ηe, ηue,
      n0e, T0e, u0e, ωse, kyrhoe},
   dispRel :=
    Together[Simplify[
     (Together[
```

```
        n1kinetic[-e, me, B, c, ϕ, vte, ηe, ηue, n0e, T0e, u0e, -ωse, kz, ω, Z4PAu[vte, u0e, kz, ω]] /(e
              n0e ϕ)/T0e]*(1/(1 + (-kyrhoe)^2))
  - (Together[
        n1kinetic[e, mi, B, c, ϕ, vti, ηi, ηui, n0i, T0i, u0i, ωsi, kz, ω,
        Z4PAu[vti, u0i, kz, ω]] /(e n0e ϕ)/T0e]*(1/(1 + kyrhoi^2))
  + Together[
        IonPolT[kyrhoi, e, ϕ, n0i, T0i]/(e n0e ϕ)/T0e]))
        /.{ηi -> κTiDRB1/κnDRB1, ηui -> κuiDRB1/κnDRB1,
        u0i -> u0iDRB1, ωsi -> kyrhosDRB1*csDRB1*ϵTDRB1*κnDRB1,
        kyrhoi -> kyrhosDRB1*Sqrt[ϵTDRB1],
        T0i -> ϵTDRB1*T0eDRB1,
        vti -> csDRB1*Sqrt[ϵTDRB1], n0i -> n0e,
        ηe -> κTeDRB1/κnDRB1, ηue -> κueDRB1/κnDRB1,
        u0e -> u0eDRB1, ωse -> kyrhosDRB1*csDRB1*κnDRB1,
        kyrhoe ->  kyrhosDRB1/μDRB1, T0e -> T0eDRB1,
        vte -> csDRB1*μDRB1,
        kz -> kzDRB1, ω -> ωDRB1}
  *Denominator[Z4PAu[vti,u0i,kz,ω]]]
   ];
   result = Together[dispRel*Denominator[dispRel]];
   result
];
```

Listing 4.12: disprel2 - The dispersion relation “disprel2” includes kinetic electrons and kinetic ions.

4.3 Functionality

In the section of the program named “Plot Growth Rate, Frequency and Diffusion” the calculation and plotting can be started. A typical example is shown in listing 4.13.

```
fctClearAll;
anNu = fctAnNu[nn];
gD = 0; maxArray = {};
actValueList = valueListkz;
stepSize = {10^-15, 0.6, 1*10^-3};
PlotRangeArray = {{0, 0.6}, {-0.3, 0.7}};
varNow = ToString[AbsoluteTime[DateString[]]];
solutionsArray = Join[fctSolve[anNu[[1, 1]], actValueList, stepSize, gD],
                fctSolve[anNu[[1, 2]], actValueList, stepSize, gD]];
solPlot = fctListPlot[solutionsArray, anNu[[2]], PlotRangeArray, anNu[[3]], actValueList,
        "kz a", "γ/(vti/a)"];
Export[path0<>"growthRate/"<>fctDirPath[actValueList]<>"/n_g_kz_"<>varNow<>''.gif", solPlot];
maxArray = fctReturnMax[solutionsArray];
```

```
14 Export[path0<>"growthRate/"<>fctDirPath[actValueList]<>"/n_g_kz_"<>varNow<>’’.csv", maxArray];
15 solPlot
16 maxArray
```

Listing 4.13: Use of the program - This is a typical example for the use of the program. Both plot and the list that contains the maxima of the modes will be saved and output.

To exclude variable definition problems, in line 1 some of the variables are cleared via the function “fctClearAll”. The next line selects the underlying dispersion relations, in this case both numerical ones are chosen, “disprel1” and “disprel2”, via “anNu = fctAnNu[nn]”. Other options are shown in table 4.4.

aa	gammaanX, disprel0
nn	disprel1, disprel2
na	disprel2, disprel0
n	disprel2

Table 4.4: Options for “fctAnNu” - The X will be replaced by the number 1-4 in the section of the initial parameters. The variable “disprel1” denotes the dispersion relation for kinetic ions and adiabatic electrons, “disprel2” kinetic ions and kinetic electrons. Both “gammaanX” and “disprel0” are described in detail in section 4.2.3.

The parameter “gD” in line 3 chooses between γ (gD=0), ω_r (gD=1) or D (gD=2). Since in the analytically calculated dispersion relation the ions are based on an easy fluid model, plotting the analytic dispersion relation “disprel0” for nonzero ion parameters like temperature gradient or a parallel ion flux is not meaningful. Nevertheless, not to restrain the free choice of the user, it is allowed.

The abscissa-variable is chosen in “actValueList”, listing 4.13 line 4. For plots versus k_z, choose “actValueList = valueListkz”. The options for other variables are shown in table 4.5.

In 4.13, line 5, the range and the step size for the calculation are defined: the first value is the starting point, followed by the step size and the stopping

Free variable	**actValueList**
k_z	valueListkz
k_y	valueListky
k_z, k_y	valueListkykz
u_{e0}	valueListue0
κ_{ue}	valueListkappau0
κ_{Te}	valueListkappaTe
κ_{Ti}	valueListkappaTi

Table 4.5: Options for "actValueList" - The choice of "actValueList" defines the independent variable, which is as well the abscissa of the plots.

point. For numerical reasons, $k_z = 0$ is not possible, so it is recommended to start at an appropriate small, but nonzero value. In the next line, the plot range is defined: the first value is for the horizontal and the second for the vertical axis. Calculated solutions are stored in the variable "solutionsArray". The plot itself is written in "solPlot" and, via the export command, saved in the designated folder. The function "fctReturnMax" returns a list, that contains the maximum of each mode. This list is saved with the same name in the identical folder structure as the corresponding plot in order to simplify later analysis of the results.

Especially for three-dimensional cases, it is useful to be able to interact with the plot in Mathematica. With the output of "solPlot" in line 15 and "maxArray" in line 16, both figure and list of maxima are directly available in the program for further studies. In the next chapter this introduced program is used for the simulation of drift waves.

5

Numerical Study of Drift Waves

The previously discussed program provides a possibility to visualize the behavior of drift waves. In the following, drift waves, driven by density and temperature gradients and currents, are numerically analyzed. As in section 3.4, Alcator C-Mod parameters [33], which are summarized in table 3.1, are used.

5.1 Study of Growth Rates and Frequencies

The basis for this consideration is the model containing kinetic ions and kinetic electrons, discussed in section 3.2.3. First, a pure density gradient without any temperature gradients or streaming velocities is considered. The resulting plots are figures 5.1 for the growth rate versus the perpendicular wave number and 5.2 for γ versus the parallel wave number. All growth rates γ are normalized as $\gamma a/c_s$ and the wave numbers as $k_y\rho_s$ and $k_z a$. Within the considered parameter regime, one unstable mode, driven by the density gradient, exists with a maximum of $(k_y\rho_s, \gamma a/c_s) = (1.7, 0.0185)$ at $k_z a = 0.13$, as depicted in figure 5.1.

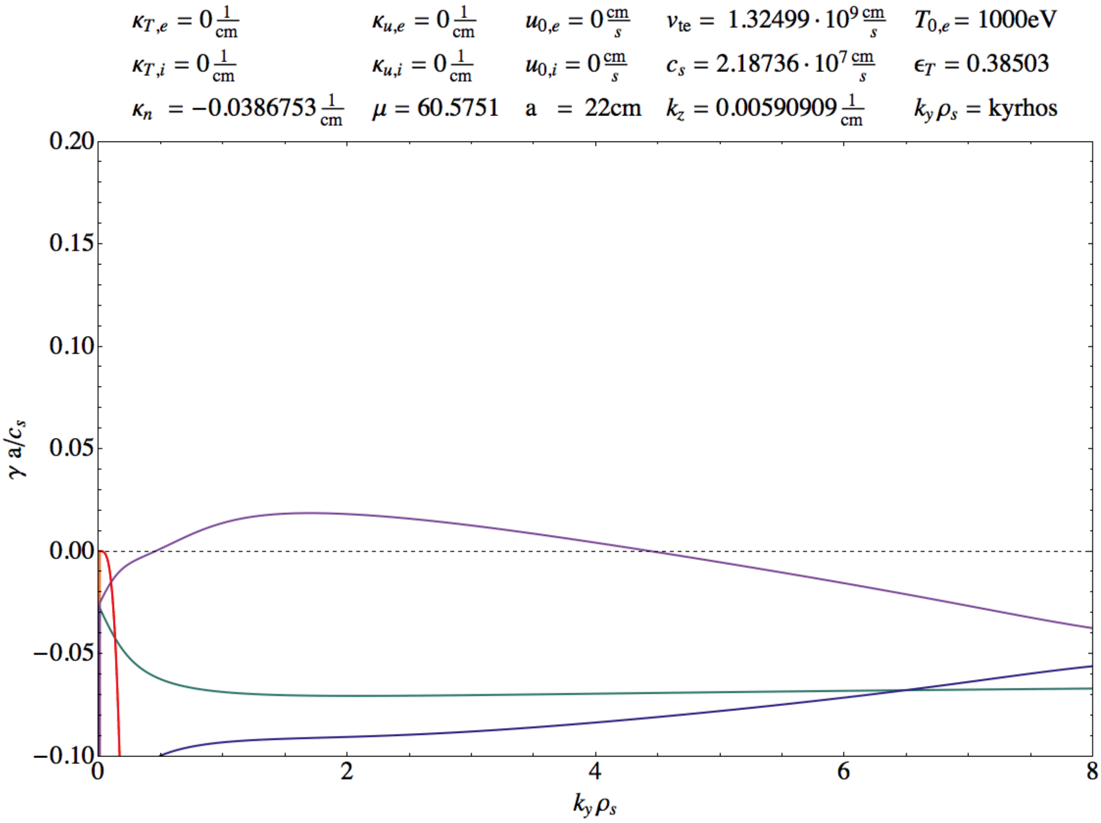

Figure 5.1: Growth rate versus $k_y\rho_s$ with $\eta_i = \eta_e = 0$, $u_{0,e} = 0$ - density gradient $\kappa_n = -0.0387\text{cm}^{-1}$ and $k_z a = 0.13$. One unstable mode exists with a maximum at $(k_y\rho_s, \gamma a/c_s) = (1.7, 0.0185)$.

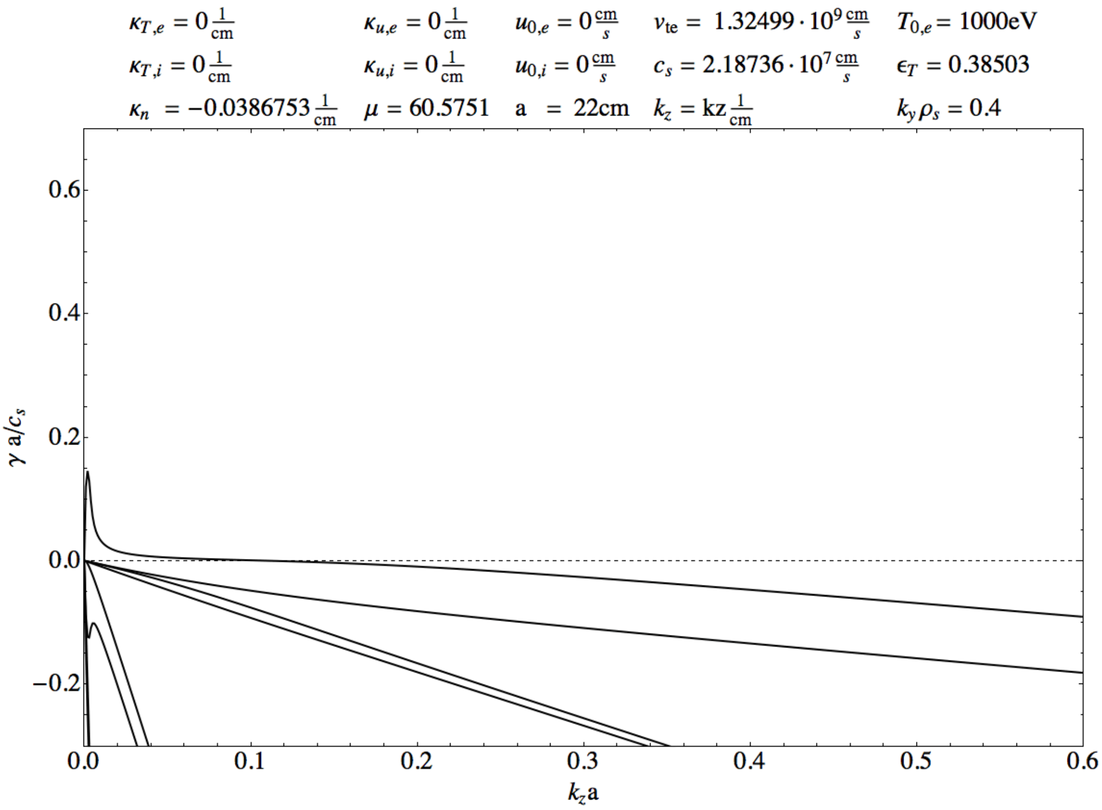

Figure 5.2: Growth rate versus $k_z a$ with $\eta_i = \eta_e = 0$, $u_{0,e} = 0$ - density gradient $\kappa_n = -0.0387\mathrm{cm}^{-1}$ and $k_y\rho_s = 0.4$. This plot corresponds to figure 5.1, which shows the same mode, driven unstable by the density gradient, in perpendicular wave number direction.

Subsequently, temperature gradients of electrons and ions and positive and negative electron currents are added separately and together, to study the resulting drift waves. With the next step, an ion temperature gradient with $\eta_i = 4.2455$ is added. Figure 5.3 illustrates the arising of the η_i-mode, which appears to have an about six times higher growth rate maximum than the purely density gradient driven mode. The growth rate versus parallel wave number, as well as an extended range of $k_y \rho_s$, can be found in the appendix chapter A, figures A.1 and A.2.

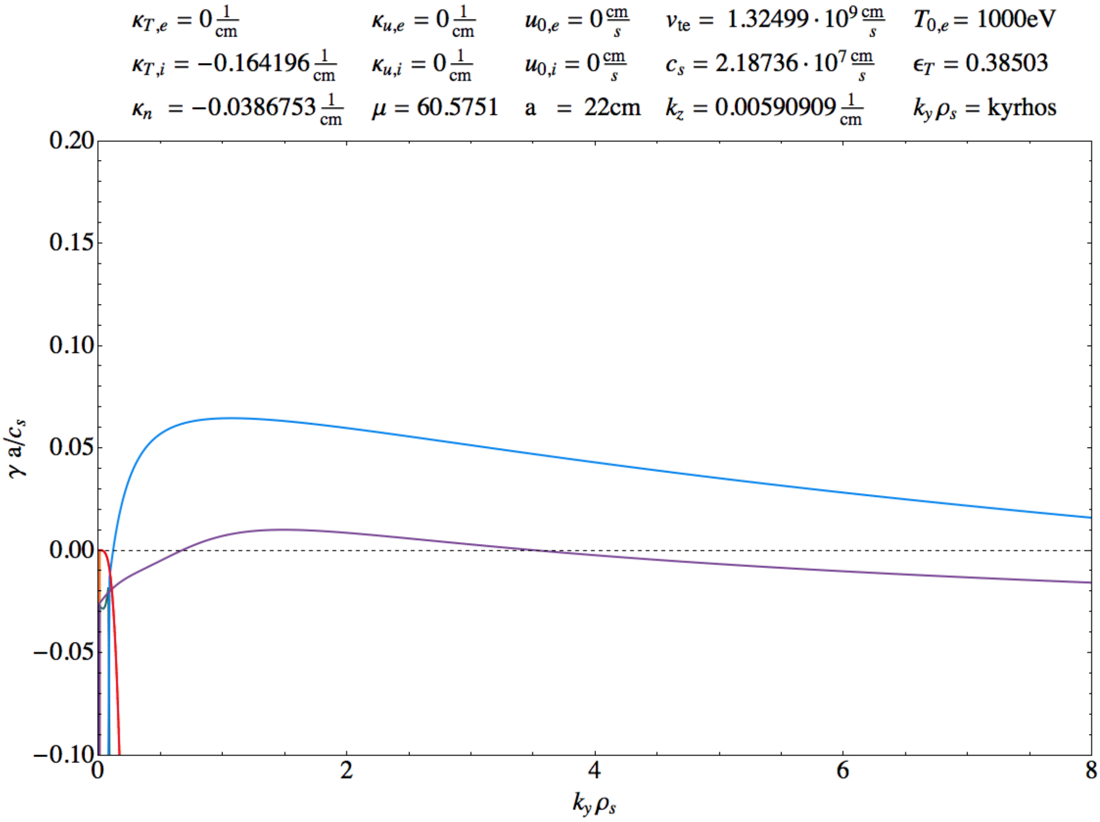

Figure 5.3: Growth rate versus $k_y \rho_s$ with $\eta_i \approx 4.25$, $\eta_e = 0$, $u_{0,e} = 0$. - The ion temperature gradient lowers the maximum growth rate of the density gradient driven mode to $(1.49, 0.01)$, but additionally, a new mode arises with a six times higher maximum growth rate of $(1.07, 0.064)$ for $k_z a = 0.13$.

An electron temperature gradient with the scaling $\eta_e \approx 4.06$, however, stabilizes the drift wave (see figures 5.4 and A.4), consistent with the predictions of the analytic studies in section 3.4. The growth rate γ is axially symmetric for $\pm\, k_y\rho_s$, as shown in figure A.3 in the appendix.

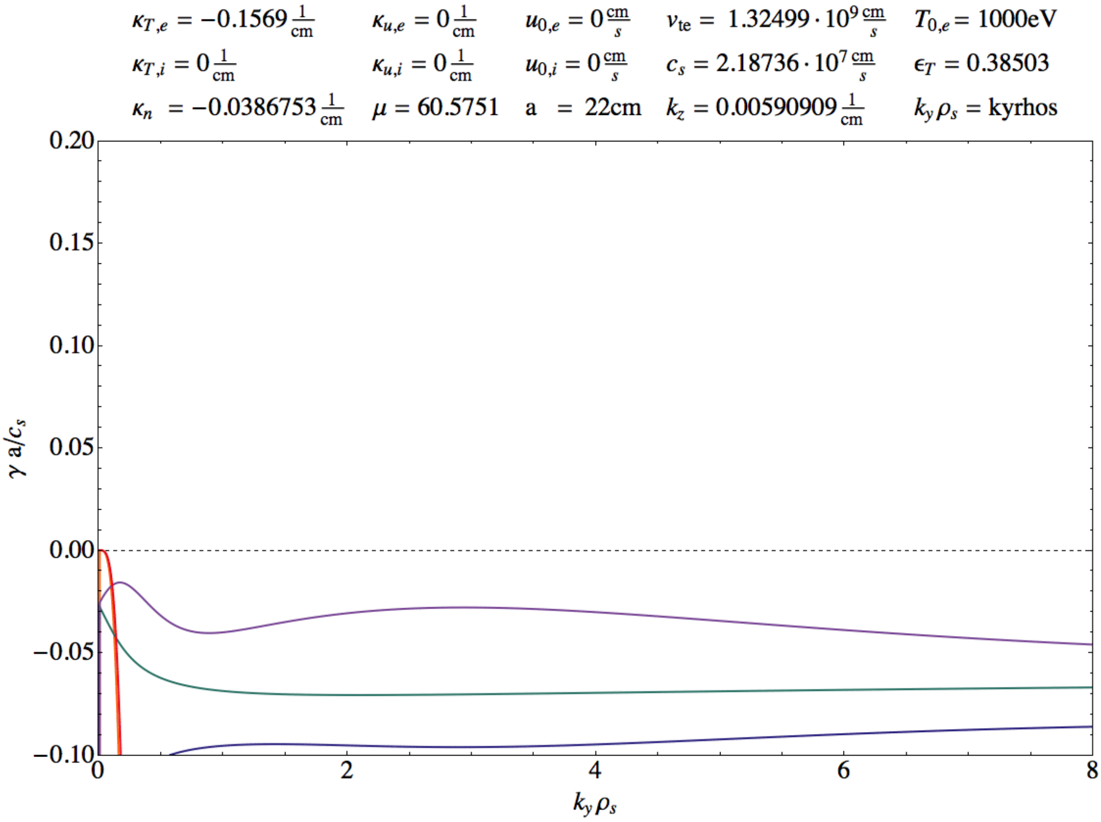

Figure 5.4: Growth rate versus $k_y\rho_s$ with $\eta_i = 0$, $\eta_e \approx 4.06$, $u_{0,e} = 0$. - The electron temperature gradient results in a damping; all modes are stable. The growth rate versus k_z is shown in figure A.4.

A combination of ion and electron temperature gradients results in a slightly less growing η_i mode compared to figure 5.3, as illustrated in figure 5.5. The maximum lowers marginally from $(1.07, 0.064)$ for an ion temperature gradient to $(1, 0.06)$ for an additional electron temperature gradient. The axial symmetry is preserved for γ versus $k_y\rho_s$ for both $\eta_e \neq 0$ and $\eta_i \neq 0$. Other figures with these parameters can be found in the appendix, figures A.5 and A.6.

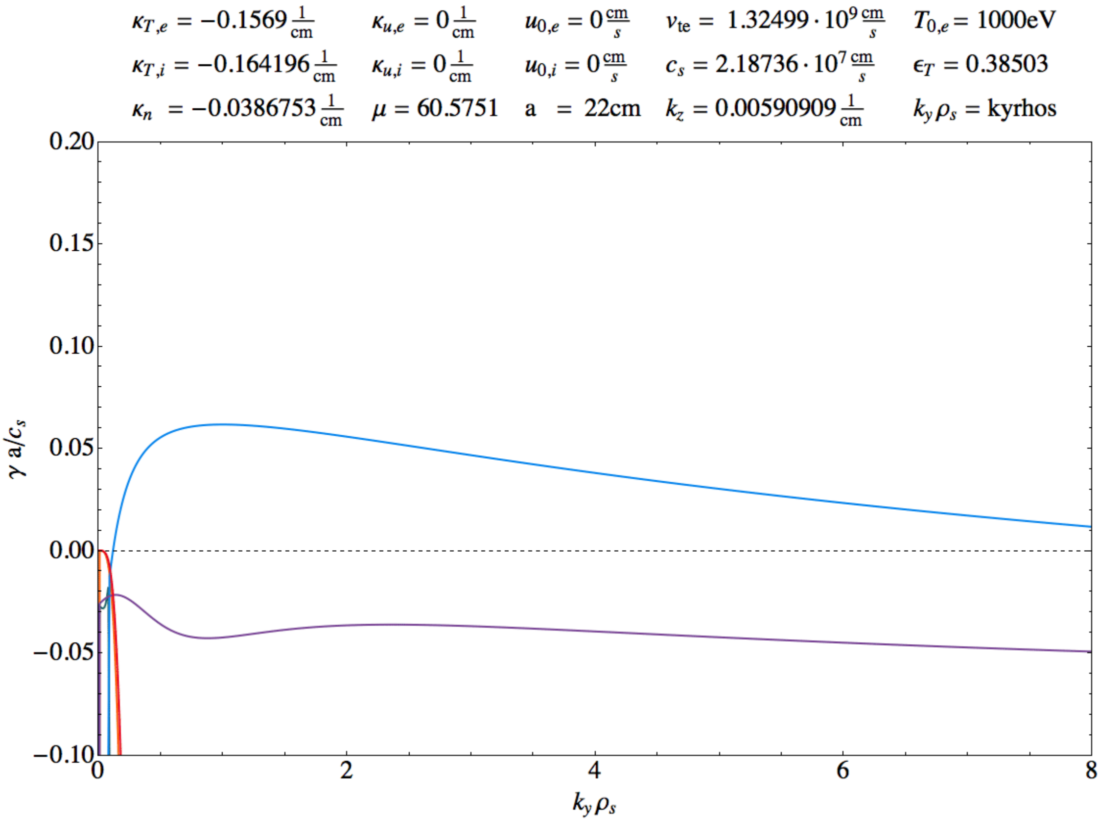

Figure 5.5: Growth rate versus $k_y\rho_s$ with $\eta_i \approx 4.25$, $\eta_e \approx 4.06$, $u_{0,e} = 0$. - The existence of an electron temperature gradient lowers the η_i-mode minimally; the maximum is at $(1, 0.06)$.

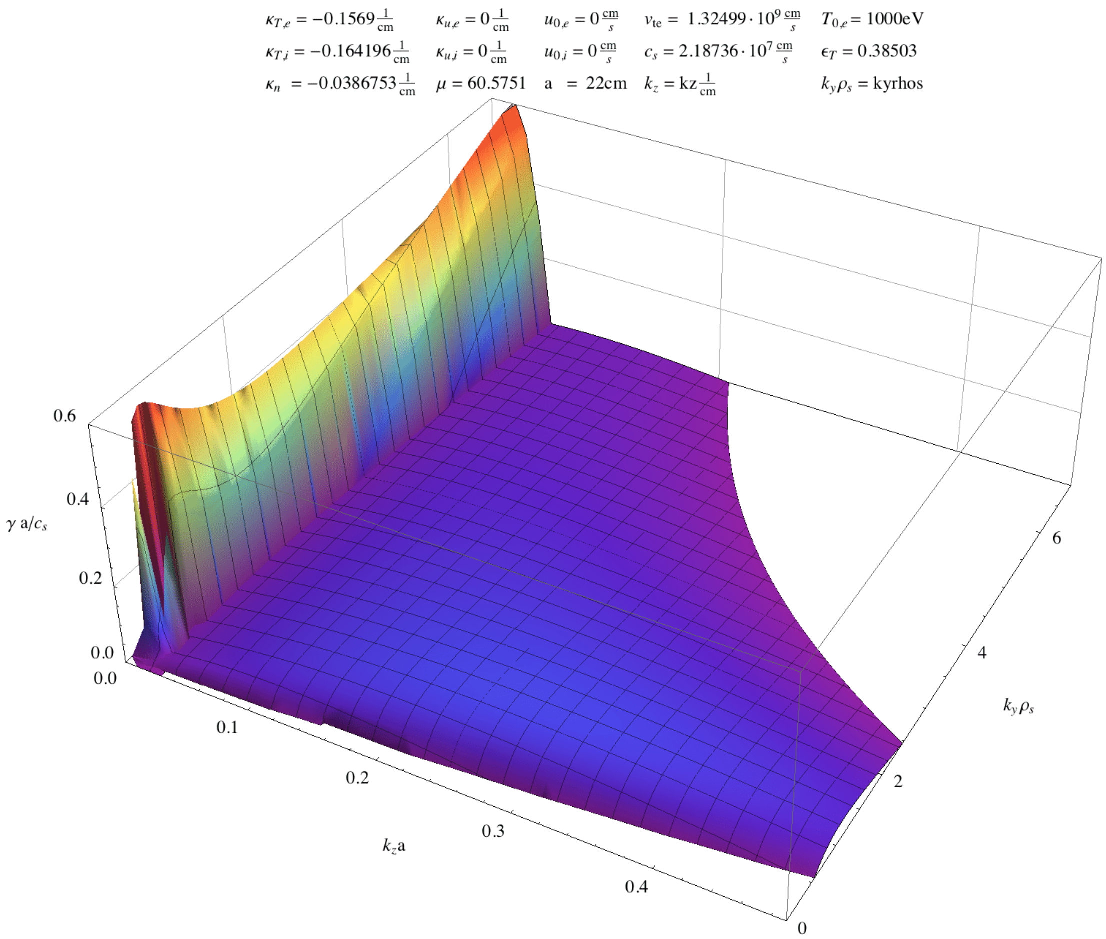

Figure 5.6: Growth rate versus $k_z a$ and $k_y \rho_s$ with $\eta_i \approx 4.25$, $\eta_e \approx 4.06$, $u_{0,e} = 0$. - This plot shows the modes in three dimensions. A detail is shown in figure A.7.

Solving the dispersion relation for the standard parameters as previously, but with a positive electron drift current $u_{0,e}$, the drift wave can be driven unstable, depending on the absolute value of $u_{0,e}$. Using a drift parameter of $u_{0,e}/c_s = 2.09279$, which was estimated in section 3.3 considering an elongation $\kappa = 1.221334$ and a magnetic shearing $\hat{s} = 1.625332$, the growth rate of the drift wave (illustrated in purple in figure 5.7) is raised, but still negative. Illustrations of the growth rate versus $k_z a$ as well as versus an extended range of $k_y \rho_s$ are shown in figures A.8 and A.9.

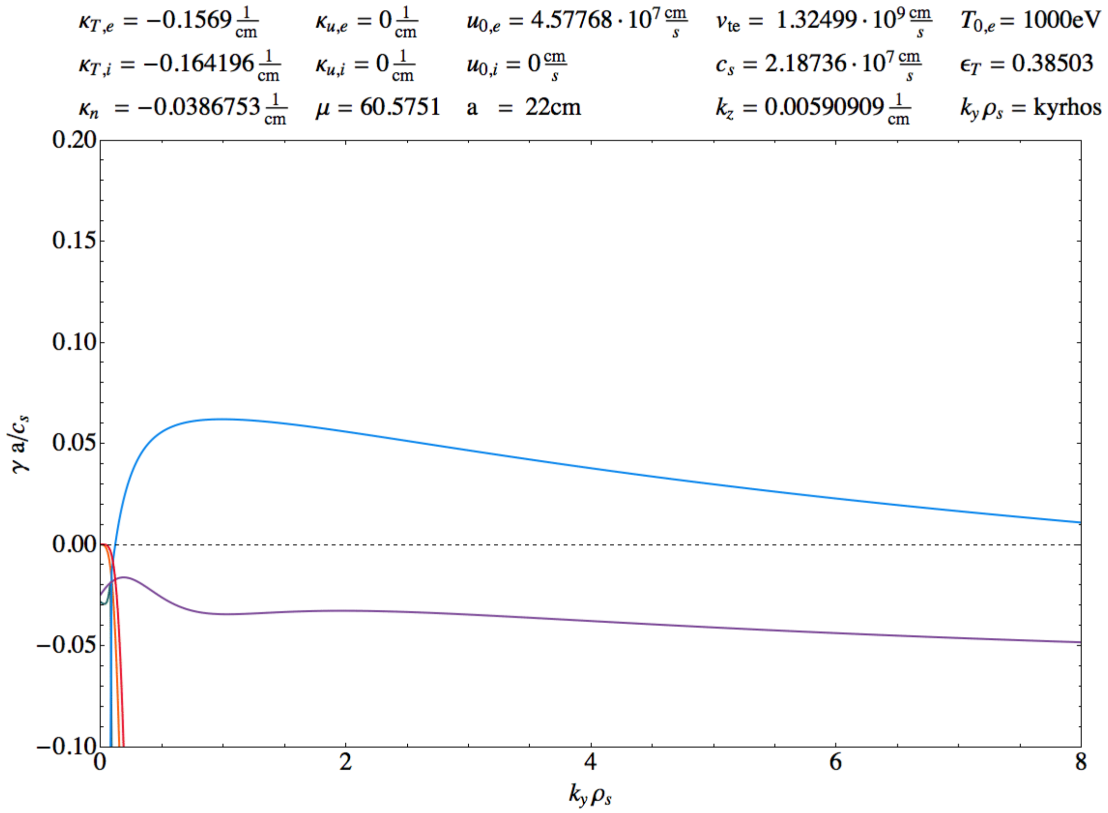

Figure 5.7: Growth rate versus $k_y \rho_s$ with $\eta_i \approx 4.25$, $\eta_e \approx 4.06$, $u_{0,e} \approx 2c_s$. - Comparing with figure 5.5, the electron current raises the drift wave growth rate (illustrated in purple), however, it is still stable. The η_i-mode, depicted in blue, is barely influenced by $u_{\|0} \approx 2c_s$.

Concentrating on a drift parameter of $u_{0,e}/c_s = 8.04947$, which was motivated in section 3.3 for a negligible magnetic shearing, the current-driven drift wave is driven unstable, as illustrated in figure 5.8 and A.10. The maximum growth rates are at $(0.96, 0.063)$ for the η_i-mode (depicted in blue) and at $(0.33, 0.004)$ for the electron-current-driven mode (purple).

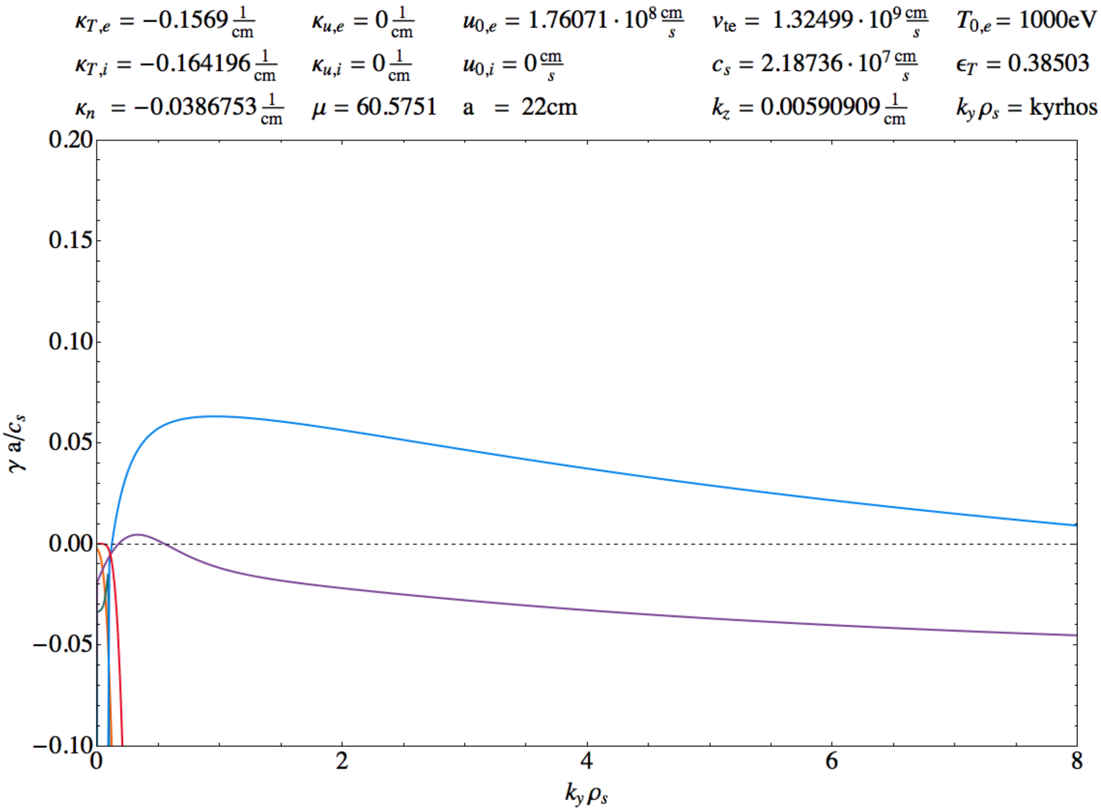

Figure 5.8: Growth rate versus $k_y\rho_s$ with $\eta_i \approx 4.25$, $\eta_e \approx 4.06$, $u_{0,e} \approx 8c_s$. - Comparing with figure 5.7, the higher electron current drives an additional mode unstable. The maxima are at $(0.96, 0.063)$ for the ion-temperature-gradient driven mode (blue) and at $(0.33, 0.004)$ for the electron-current-driven mode (purple).

Considering an even higher parallel electron drift of $u_{0,e} = 12c_s$, the influence of the current-driven drift wave becomes significant, as illustrated in figure 5.9. The maximum growth rate of the current-driven drift wave is with $(0.4, 0.021)$ only by a factor of 0.33 smaller than the maximum of the η_i-mode, $(0.94, 0.064)$.

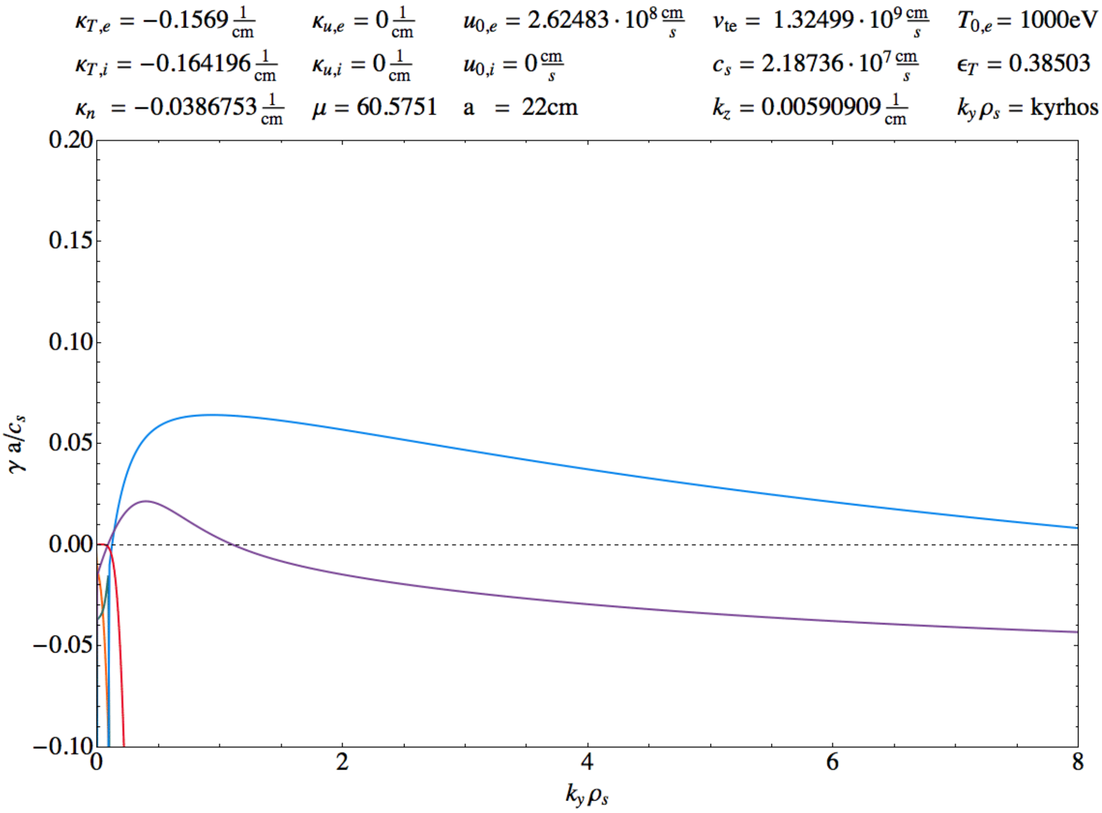

Figure 5.9: Growth rate versus $k_y\rho_s$ with $\eta_i \approx 4.25$, $\eta_e \approx 4.06$, $u_{0,e} \approx 12c_s$. - For this drift parameter, the influence of the current-driven drift wave is significant: while the maximum of the η_i-mode is at $(0.94, 0.064)$, the maximum of the CDDW is with $(0.4, 0.021)$ only by a factor of 0.33 smaller. Figure A.11 shows the same plot with an extended range of $k_y\rho_s$, and A.12 versus $k_z a$.

To classify the modes, the dispersion relation “disprel2” was solved manually and normalized by the following command:

```
(ω /.Solve[ReplaceAll[Apply[disprel2, valueListky], {kyrhos -> 0.6}] == 0, ω])
        *(vara/varcs) // ComplexExpand
```

Listing 5.1: Real- and imaginary part of ω - The dispersion relation is solved manually in order to receive $\omega = \omega_r + i\gamma$.

The following solutions are found for the real and imaginary parts of the frequency $\omega = \omega_r + i\gamma$, normalized to $a/c_s \approx 10^{-6}$s, with $ak_z = 0.13$, $k_y\rho_s = 0.4$, $u_{0,e} = 8c_s$ and the other parameters chosen according to figure 5.8:

$$\begin{array}{cc} -22.8873 - 1.41669i, & -7.64316 - 13.2063i, \\ -0.147388 - 0.148952i, & -0.0655611 + 0.0520221i, \\ 0.0942382 - 0.176544i, & 0.396842 + 0.00387484i, \\ 12.3748 - 12.2276i, & 26.4433 - 0.871923i \end{array}$$

For $ak_z = 0.13$, two modes are unstable, as illustrated in figure 5.10. The one with the greater growth rate, $\gamma \approx 0.05$, has a negative real frequency, $\omega_r \approx -0.066$. The less growing mode with $\gamma \approx 0.0039$ has a positive real frequency, $\omega_r \approx 0.397$. Since the positivity of electron drift wave frequencies is chosen as convention in this thesis, the mode with $\omega_r > 0$, is a current-driven electron drift wave.

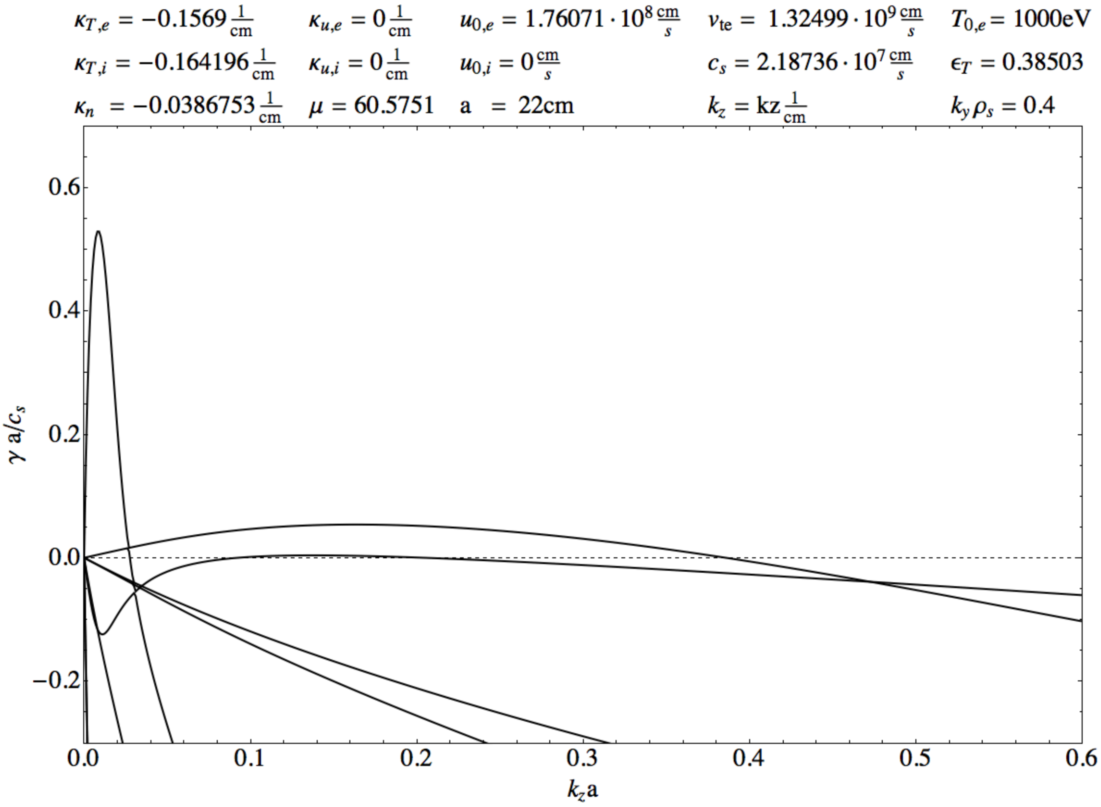

Figure 5.10: Growth rate versus $k_z a$ with $\eta_i \approx 4.25$, $\eta_e \approx 4.06$, $u_{0,e} \approx 8c_s$. - Corresponding to figure 5.8, this plot shows the modes in the parallel wave number direction. Due to the electron drift current, a third growing mode arised. The maxima of the three modes are $(0.008, 0.529)$, $(0.138, 0.00395)$ for the current-driven drift wave and $(0.163, 0.0539)$ for the ion-temperature-driven mode.

Plotting the growth rate versus the normalized electron current, one finds for $|u_{e0}| < 4 \cdot v_{te}$ one maximum for the current-driven drift wave at $(\gamma a/c_s, u_{e0}/v_{te}) = (1.51, 0.522)$, as illustrated in figure 5.11.

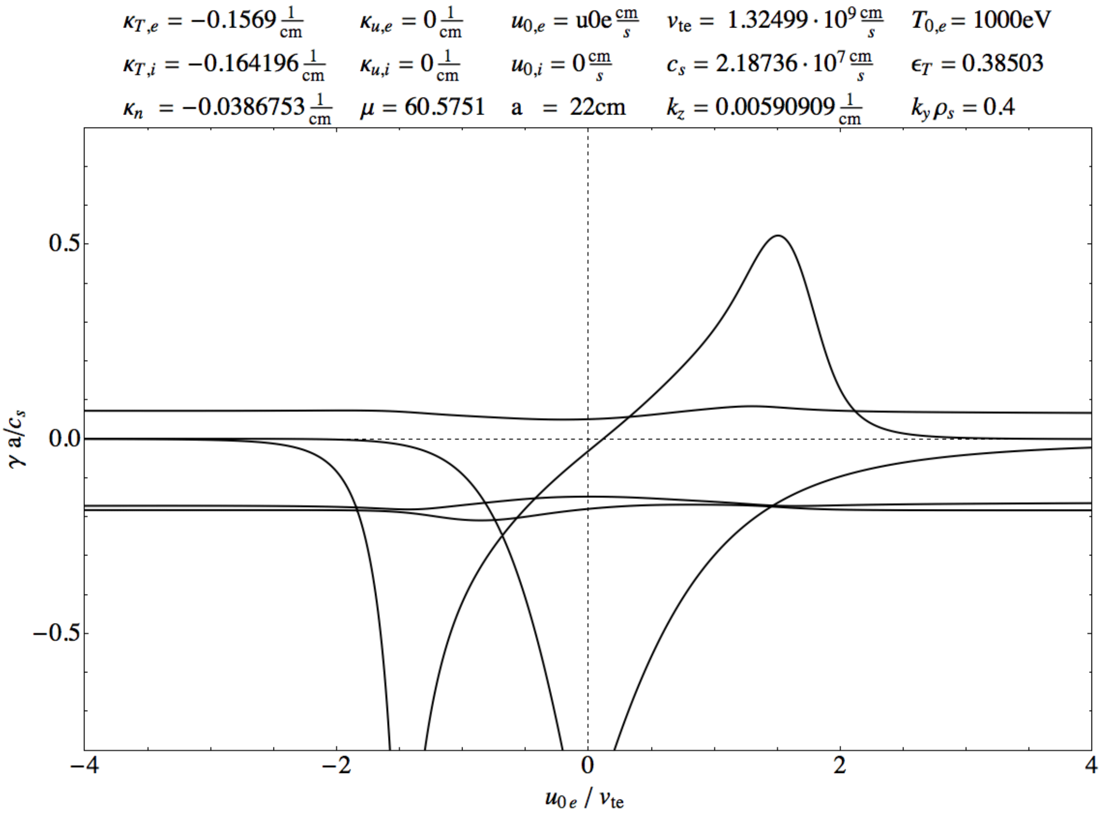

Figure 5.11: Growth rate versus $u_{0,e}/v_{te}$ with $\eta_i \approx 4.25$, $\eta_e \approx 4.06$, $k_z a = 0.13$, $k_y \rho_s = 0.4$. - A current of $u_{0,e} = 1.51\ v_{t,e}$ produces the maximum growth rate in the considered parameter regime. For $u_{0,e} > 7.16\ c_s$ the current induce a positive growth rate, as depicted in more detail in figure 5.12.

Comparing figure 5.11 with A.13, which shows the growth rate versus electron current without electron- or ion-temperature gradient, it turns out that this peak is the only mode with positive growth rate and corresponds to the current-driven drift wave.

Since in section 3.3 the drift parameter was estimated to be in the range of $u_{0,e}/c_s \approx 2$ or $u_{0,e}/c_s \approx 8$, the discussed maximum of $u_{0,e} = 1.51\ v_{te} \approx 91.5\ c_s$ is not in the range of this approximation. Scaling the horizontal axis as

$u_{0,e}/c_s$ would result in a scale from about -240 to $+240$. Plotting instead within range of the considered approximation, the electron drift wave mode becomes growing at $u_{0,e} \approx 7.16\ c_s$ and a further increase of the parallel electron velocity leads to an increasing growth rate, as illustrated in figure 5.12. Accordingly, the approximated value of $u_{0,e} = 8c_s$ is big enough to drive an electron drift wave unstable in the considered parameter regime.

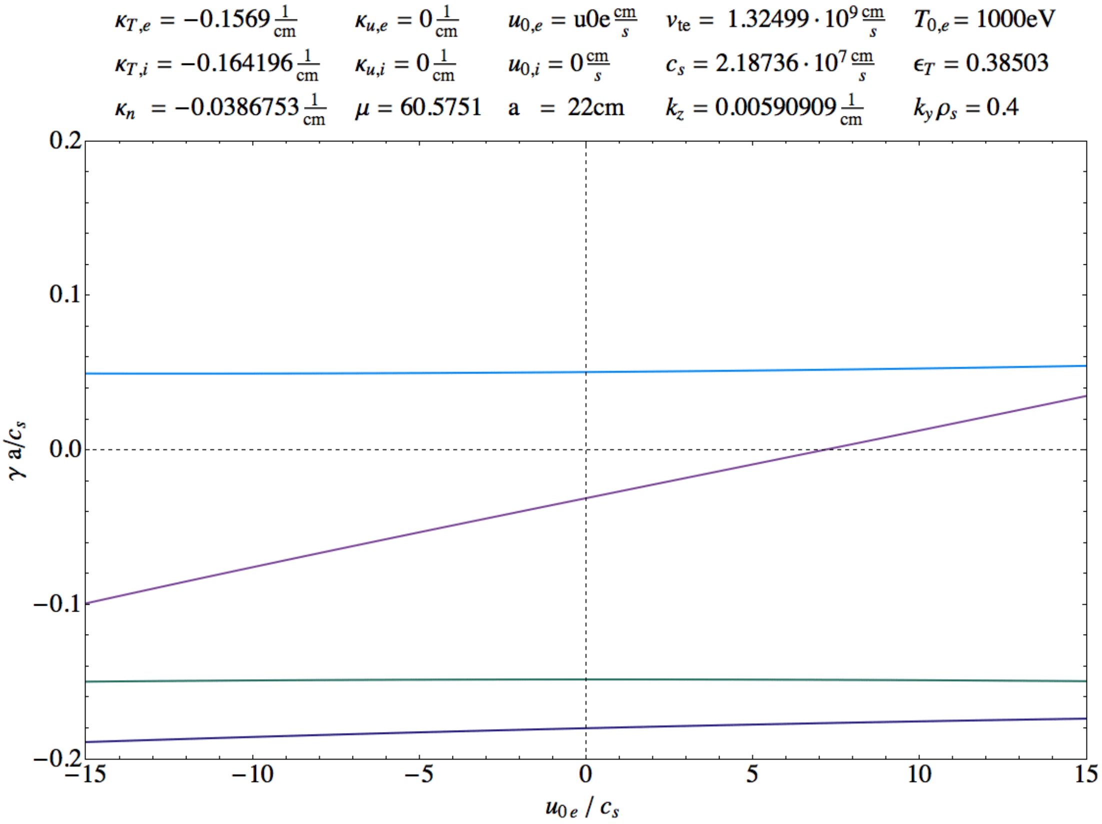

Figure 5.12: Growth rate versus $u_{0,e}/c_s$ with $\eta_i \approx 4.25$, $\eta_e \approx 4.06$, $k_z a = 0.13$, $k_y \rho_s = 0.4$. - This figure shows the zero crossing of the current-driven drift wave (illustrated in purple): for the considered parameters the mode becomes growing at $u_{0,e} \approx 7.16\ c_s$.

Setting the ion temperature gradient to zero, $\eta_i = 0$, but the electron temperature gradient remains $\eta_e \neq 0$, one mode is stabilized, while the other, $\omega \approx 0.345 + 0.0111i$, stays growing, as illustrated in figure 5.13 and calculated to:

$$\begin{array}{cc} -22.8873 - 1.41668i, & -7.64315 - 13.2063i, \\ -0.162041 - 0.0597288i, & -0.0381057 - 0.119146i, \\ 0.133063 - 0.101867i, & 0.345251 + 0.0111346i, \\ 12.3748 - 12.2276i, & 26.4432 - 0.871929i \end{array}$$

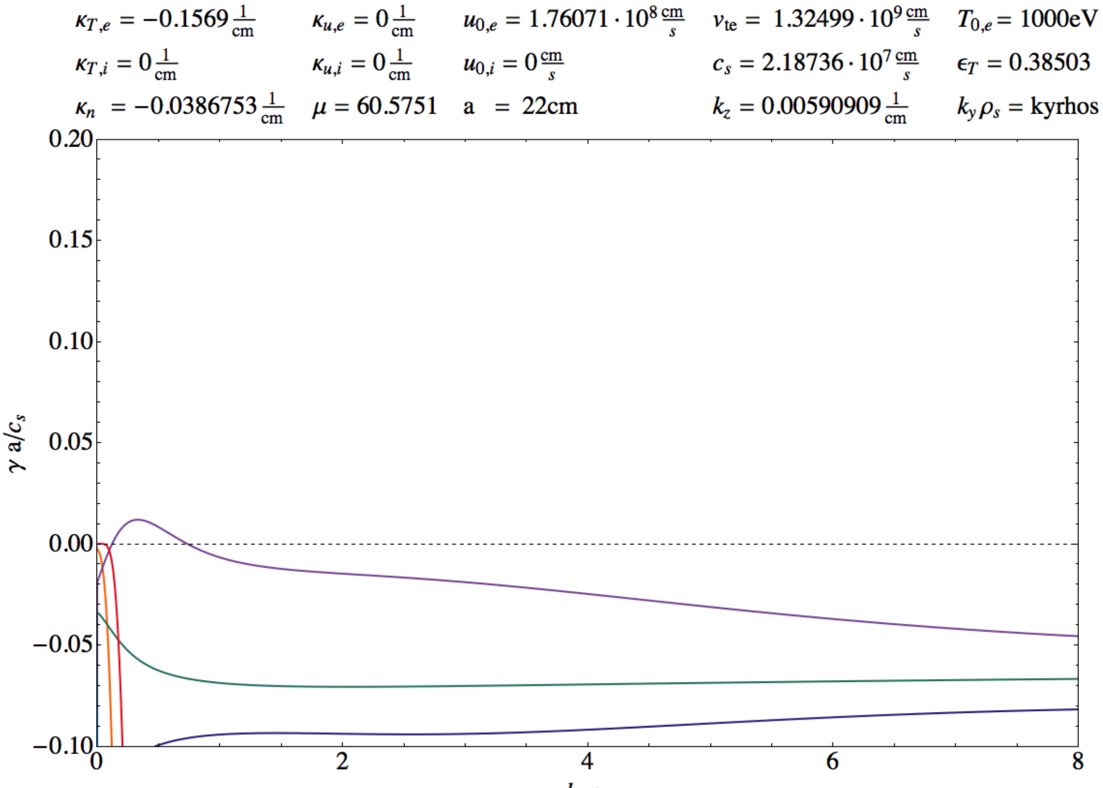

Figure 5.13: Growth rate versus $k_y\rho_s$ with $\eta_i = 0$, $\eta_e \approx 4.06$, $u_{0,e} \approx 8c_s$. - Without an ion temperature gradient, the η_i-mode disappears comparing to figure 5.8. The maximum growth rate of the current-driven drift wave is at $(0.33, 0.012)$.

This behavior is expected: the η_i-mode vanishes when setting η_i to zero. The growth rate versus parallel wave number is illustrated in figure A.15.

Conversely, with a vanishing electron temperature gradient, $\eta_e = 0$, but $\eta_i \neq 0$, both modes are still growing, as illustrated in figure 5.14. Real and imaginary parts of the frequency $\omega = \omega_r + i\gamma$ are normalized as before to $a/c_s \approx 10^{-6}$s, with $ak_z = 0.13$, $k_y\rho_s = 0.4$ and $u_{0,e} = 8c_s$. The other parameters are chosen according to figure 5.14. The frequency $\omega = \omega_r + i\gamma$ becomes:

$$\begin{array}{cc} -22.6067 - 1.2882i, & -8.23187 - 12.8219i, \\ -0.145201 - 0.149446i, & -0.0679432 + 0.053627i, \\ 0.0958183 - 0.174517i, & 0.396283 + 0.0275078i, \\ 11.8045 - 12.6989i, & 27.4195 - 0.94031i\ . \end{array}$$

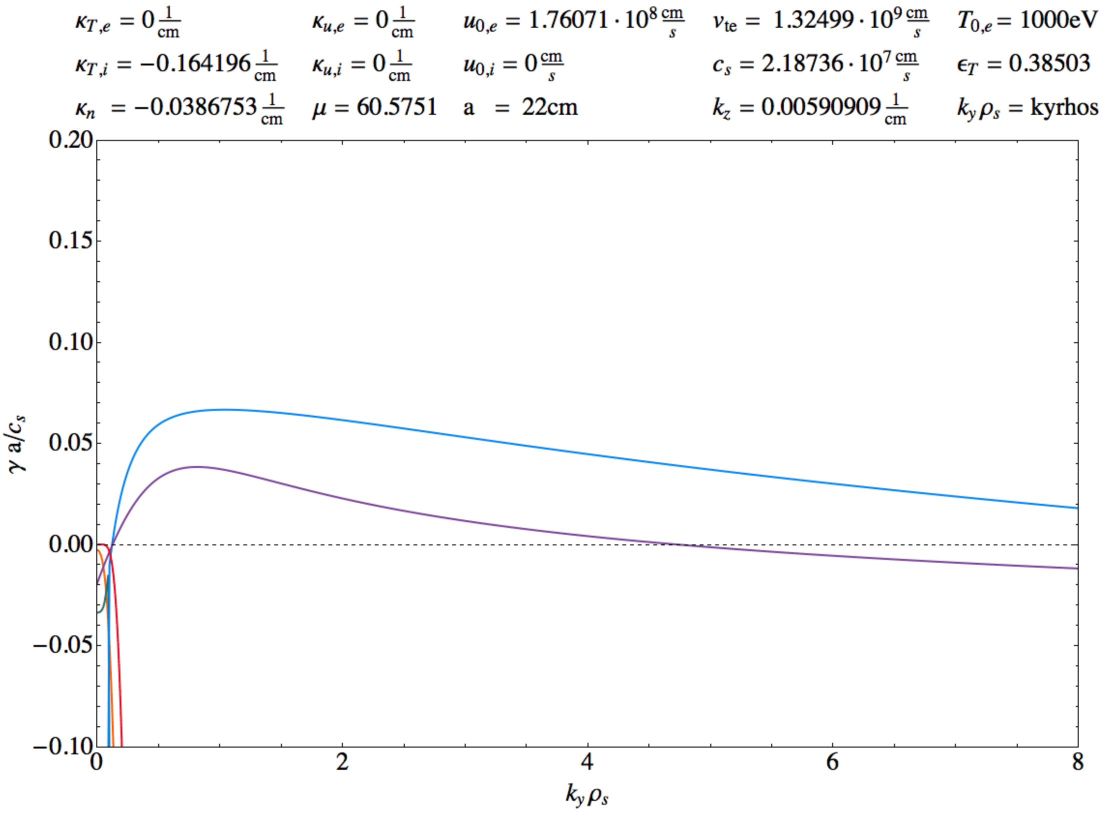

Figure 5.14: Growth rate versus $k_y\rho_s$ with $\eta_i \approx 4.25$, $\eta_e = 0$, $u_{0,e} \approx 8c_s$. - Without the strongly damping effects of the electron temperature gradient, the current-driven drift wave becomes significant: with a maximum at $(0.82, 0.038)$, it is about half as high as the maximum growth rate of the η_i-mode, $(1.04, 0.067)$. The parallel wave number direction is shown in figure A.16.

Without the strongly damping effects of the electron temperature gradient, the current-driven drift wave becomes significant: with a maximum at $(0.82, 0.038)$, it is about half as high as the maximum growth rate of the η_i-mode, $(1.04, 0.067)$. Considering as before an even higher parallel electron drift of $u_{0,e} = 12c_s$, the influence of the current-driven drift wave becomes even crucial, as illustrated in figure 5.15. The maximum growth rate of the current-driven drift wave, $(0.72, 0.056)$, is only by a factor of 0.82 smaller than the maximum of the η_i-mode, $(1.02, 0.068)$.

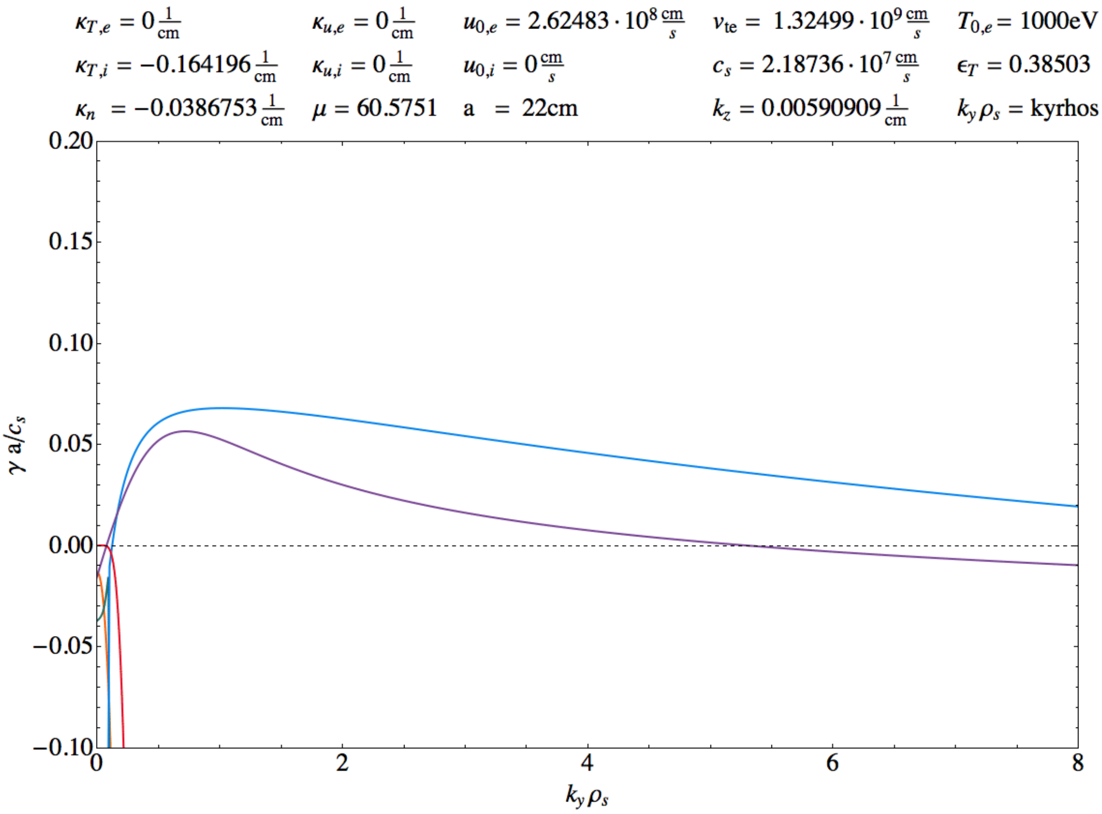

Figure 5.15: Growth rate versus $k_y\rho_s$ with $\eta_i \approx 4.25$, $\eta_e = 0$, $u_{0,e} \approx 12c_s$. - For this drift parameter, the influence of the current-driven drift wave is significant: while the maximum of the η_i-mode is at $(1.02, 0.068)$, the maximum of the current-driven drift wave, $(0.72, 0.056)$, is only by a factor of 0.82 smaller.

Setting both η_e and η_i to zero, the current-driven mode, $\omega = 0.345 + 0.036i$, is still unstable for $k_z a = 0.13$ and $k_y \rho_s = 0.4$:

$$\begin{array}{cc}
-22.6068{-}1.28819i, & -8.23185{-}12.8218i, \\
-0.162084{-}0.0599788i, & -0.0372164{-}0.118889i, \\
0.133131{-}0.100215i, & 0.345164{+}0.0362462i, \\
11.8045{-}12.699i, & 27.4195{-}0.940316i\ .
\end{array}$$

This purely current-driven mode, with only density gradient and electron current as source of dissipation, is illustrated in figure 5.16 for the perpendicular direction, as well as in A.17 for the parallel wave number direction.

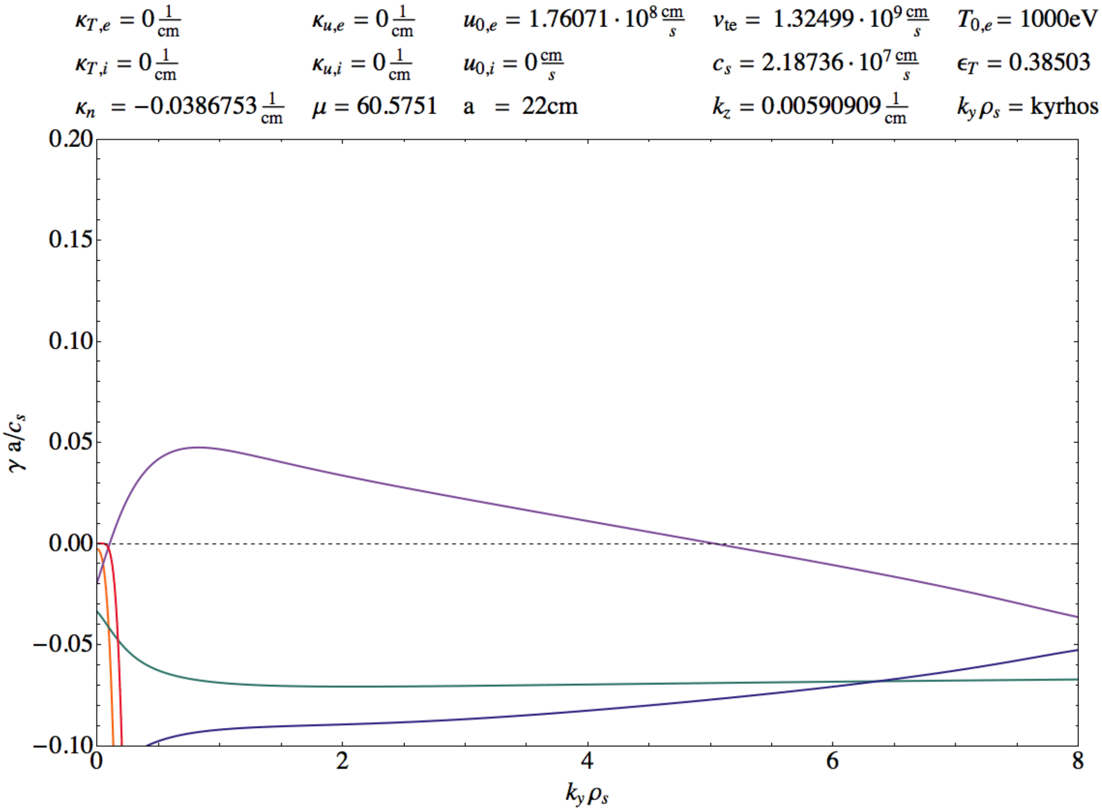

Figure 5.16: Growth rate versus $k_y\rho_s$ with $\eta_i = 0$, $\eta_e = 0$, $u_{0,e} \approx 8c_s$. - Comparing with figure 5.1, the electron current $u_{0,e}$ raises the maximum to $(0.82, 0.0475)$, which is an increase by about a factor of 2.6.

With a negative electron current, there is no current-driven drift wave at this particular value of $k_y\rho_s = 0.4$ and $k_z a = 0.13$:

$$\begin{array}{cc} -28.7618-0.917744i, & -11.433-13.1268i, \\ -0.154541-0.149059i, & -0.0579192+0.0493975i, \\ 0.0907283-0.184652i, & 0.397617-0.0671231i, \\ 8.82291-12.4258i, & 22.056-1.17043i\ . \end{array}$$

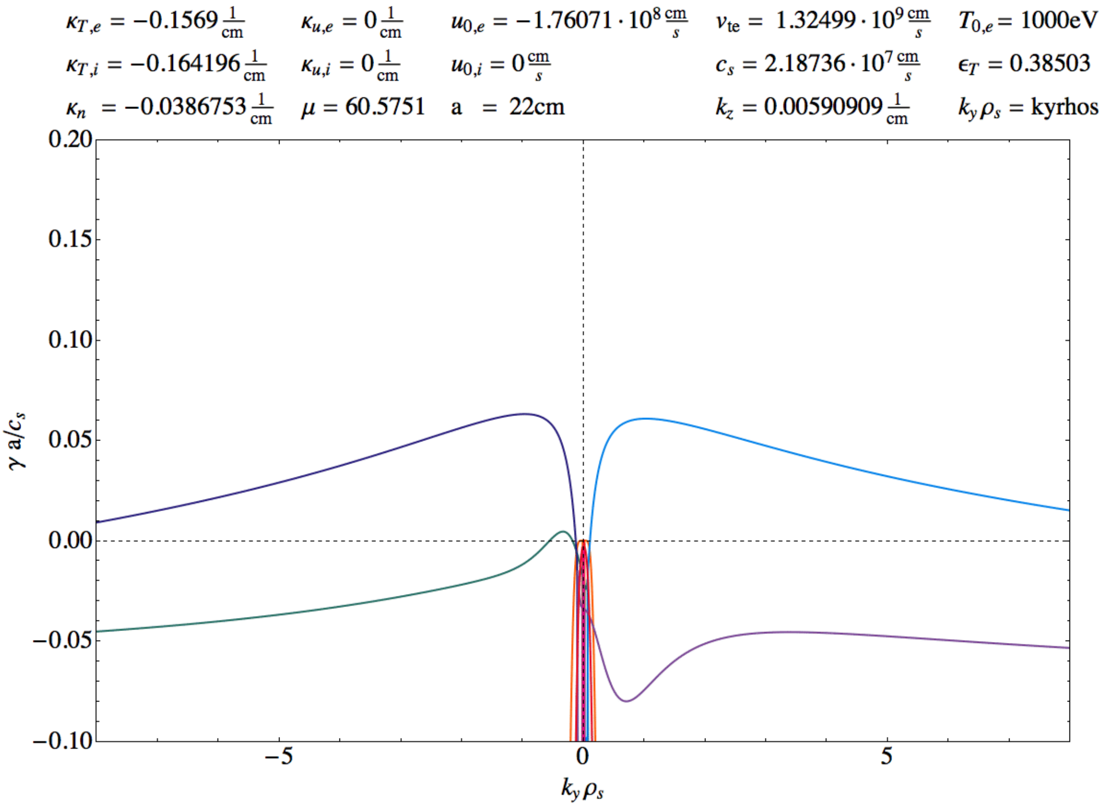

Figure 5.17: Growth rate versus $k_y\rho_s$ with $\eta_i \approx 4.25$, $\eta_e \approx 4.06$, $u_{0,e} \approx -8c_s$. - Comparing with figure A.10, the growth rate is symmetric regarding simultaneous change of $k_y\rho_s$ and $u_{0,e}$.

Comparing figure 5.17 with figure A.10 shows the symmetry of the growth rate regarding simultaneous sign change of $k_y\rho_s$ and $u_{0,e}$. Therefore, the current-driven drift wave at negative $u_{0,e}$ is identical to that for positive $u_{0,e}$, but it has a reversed sign of k_y. Since ω is invariant under simultaneous sign change of L_n and

k_y, the same results for drift waves are reached with a positive density gradient $\kappa_n = d_x n/n$ and negative values of $k_y \rho_s$, leading to a negative v_{de}, but resulting again in a positive $\omega_{*e} = k_y v_{de}$.

5.1.1 Comparison between Fluid and Kinetic Ions

In section 3.2.2, the dispersion relation for drift waves, modeled with simplified kinetic electrons and fluid ions, was calculated. As previously discussed, both growth rate and frequency are only calculated automatically if $\omega = \omega_r + i\gamma$ meets the condition $|\omega| < 0.05\, k_z v_{te}$, ensuring the adequacy of the fluid model. In section 3.4 the agreement of the dispersion relation, based on fluid ions and simplified kinetic electrons, with analytic approximation of the growth rate was shown.

For fluid equations to be valid, the ions are assumed to be cold as compared to the electrons $T_i \ll T_e$. In the Alcator C-Mod parameter range, which is examined in this thesis, the two models show partly related behavior, although the kinetic ions show more details.

5.1.2 The “very fast” electron mode

When considering the kinetic ion response with the four pole approximation, which is a third-order polynomial $P_3(\zeta)$, divided by a fourth order polynomial $P_4(\zeta)$, one gets

$$\begin{aligned} R_s =& -\tilde{n}_i \frac{T_{i0}}{n_0 e \tilde{\Phi}} \\ =& 1 + \eta_i \zeta_* \zeta + \left[\zeta + \zeta^* \left(1 - \frac{\eta_i}{2} - \eta_i \zeta^2\right)\right] \frac{P_3(\zeta)}{P_4(\zeta)} \; . \end{aligned}$$

For the case of adiabatic electrons, the dispersion relation becomes after multiplication with the denominator of Z

$$-\frac{T_{i0}}{T_{e0}}P_4(\zeta) = P_4(\zeta) + \eta_i\zeta_*\zeta P_4(\zeta) + \left[\zeta + \zeta^*\left(1 - \frac{\eta_i}{2} - \eta\zeta^2\right)\right]P_3(\zeta)\ .$$

This equation contains ζ^5, resulting in the expectation of 5 solutions. As discussed in section 3.3, it turns out that there exist just 4 solutions, since the coefficients of the highest order in each polynomial are the same (3.35), canceling out the fifth solution.

However, we found when calling the corresponding function in Mathematica for a density gradient $\kappa_n \approx 3.9 \cdot 10^{-8}$ 1/cm , an ion temperature gradient $\kappa_{Ti} \approx 0.16$ 1/cm , $T_{0,e} = 1000$ eV , $k_y\rho_s = 0.6$ and $k_z = 0.01$ 1/cm , the following 5th order equation:

$$\begin{aligned} 0 =& (2.57071 \cdot 10^{22} + 7.93536 \cdot 10^{22} i) + (1.03103 \cdot 10^{17} - 1.47297 \cdot 10^{17} i)\omega \\ & -(4.60029 \cdot 10^{11} - 390659.i)\omega^2 + (0.50758 + 769649.i)\omega^3 \\ & +(1. + 3.357562189496173 \cdot 10^{-15} i)\omega^4 + 5.123233321382795 \cdot 10^{-20}\omega^5\ . \end{aligned}$$

By solving this equation, the very small coefficient of the ω^5-term results in a very fast mode, $\omega \sim 10^{19}$:

$$\begin{aligned} &\{\omega \to -1.95189 \cdot 10^{19} + 704113.\ i\}, \{\omega \to -657601. - 79889.8\ i\}, \\ &\{\omega \to -146772. - 491084.\ i\}, \{\omega \to 330202. + 211204.\ i\}, \\ &\{\omega \to 474171. - 409879.\ i\}\ . \end{aligned}$$

Fortunately it was found that internal rounding issues resulting in 10^{-20} instead of 0, caused this non-physical additional mode. The code was modified in such a way that an exact cancellation was preserved, thus yielding $0 \cdot \omega^5$ and eliminating this additional mode.

5.2 Diffusion Studies

To evaluate the particle transport, the calculated growth rates are used for diffusion studies based on the mixing length approximation discussed in section 2.6.2,

$$D_{mix} \sim \frac{\gamma}{k_y^2} \ .$$

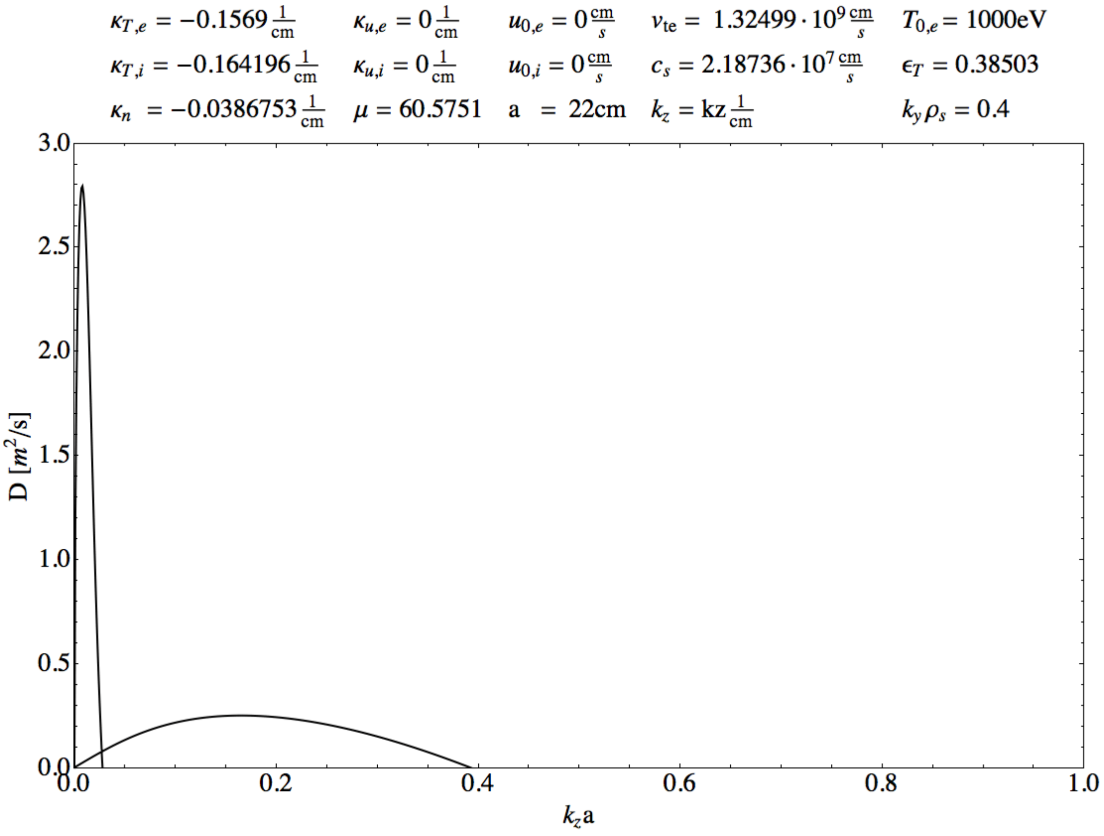

Figure 5.18: Diffusivity versus $k_z a$ with $\eta_i \approx 4.25$, $\eta_e \approx 4.06$, $u_{0,e} = 0$. - For small k_z, there is a high diffusion. However, this region can be neglected due to magnetic shearing reasons.

As depicted in figure 5.18, there is a high mode for small values of k_z. This mode is assumed to be irrelevant due to magnetic shearing reasons. All calculations in this thesis assumed a plane plasma slab model, which does not include magnetic shearing. However, in a more realistic geometry the direction of the magnetic field changes, which in a simple sheared slab model can be represented by

$$\hat{\mathbf{b}} = \frac{\mathbf{B}}{B} = \hat{\mathbf{z}} + \hat{\mathbf{y}}\frac{x}{L_s} \; .$$

Until now, since $\hat{\mathbf{b}} = \hat{\mathbf{z}}$, k_z was the vector parallel to the magnetic field. In a simple toroidal model however,

$$k_{\|} = \hat{\mathbf{b}} \cdot \mathbf{k} = k_z + \frac{x}{L_s} k_y \; .$$

Long wavelength modes with $k_{\|} < 1/qR$ can extend into the good curvature region of a tokamak, where they experience damping effects. Therefore, long wavelength modes are not expected to be as important in full toroidal geometry. Furthermore, modes with too small values of $k_y \rho_s$ will be so extended radially as to be very sensitive to stabilizing effects of profile variation and sheared flows. Therefore the diffusion study will be restricted to modes in the range of $k_y \rho_s \in (0.05, 2)$ for the perpendicular wave number and $k_z a \in (a/(2qR), 2) \approx (0.03531, 2)$ for the parallel wave number.

Figure 5.19 shows the diffusivity D versus the normalized perpendicular wave number $k_y \rho_s$ for $u_{0,e} = 0$. Three dimensional plots of D_{mix} versus parallel and perpendicular wave number are shown in figures 5.20 and B.1.

The experimental level of the thermal diffusivity of electrons is $1\mathrm{m}^2/\mathrm{s} \le \chi_e \le 2\mathrm{m}^2/\mathrm{s}$ and for the ions $0.3\mathrm{m}^2/\mathrm{s} \le \chi_i \le 0.4\mathrm{m}^2/\mathrm{s}$, as pictured in figure 5.21 [33]. The diffusivities found in this thesis, for example in figure 5.20, are with $D_{mix} < 2$ in approximately the right range.

An electron current of $u_{0,e} > 7.16 c_s$ gives rise to an additional growing mode, as shown in section 5.1. For $u_{0,e} = 8.04947 c_s$ this extra mode results in a maximum diffusion of $(0.25, 0.0415\,\mathrm{m}^2\mathrm{s}^{-1})$, as depicted in figure 5.22. The maximum

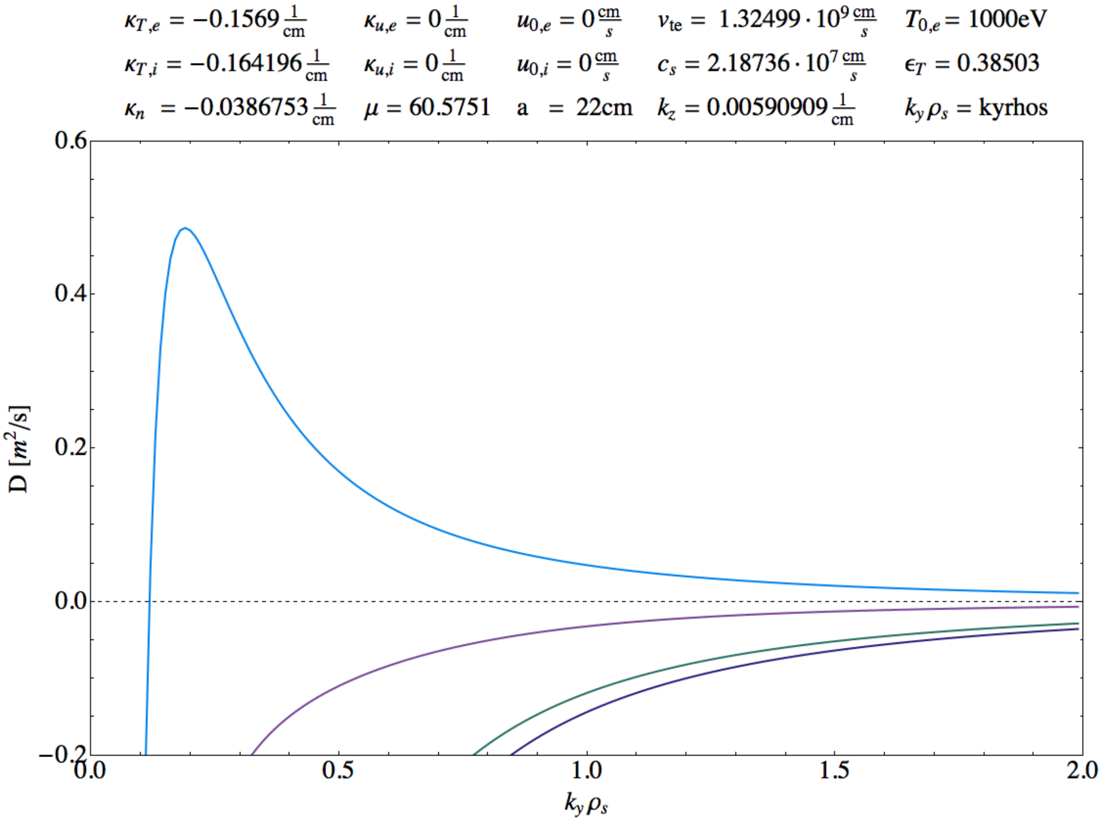

Figure 5.19: Diffusivity versus $k_y\rho_s$ with $\eta_i \approx 4.25$, $\eta_e \approx 4.06$, $u_{0,e} = 0$. - The diffusivity for $k_z a = 0.13$ has a maximum at $(0.19, 0.486\,\mathrm{m^2 s^{-1}})$. Figure 5.18 shows the diffusivity for the same parameters in parallel wavelength direction and 5.20 in three dimensions.

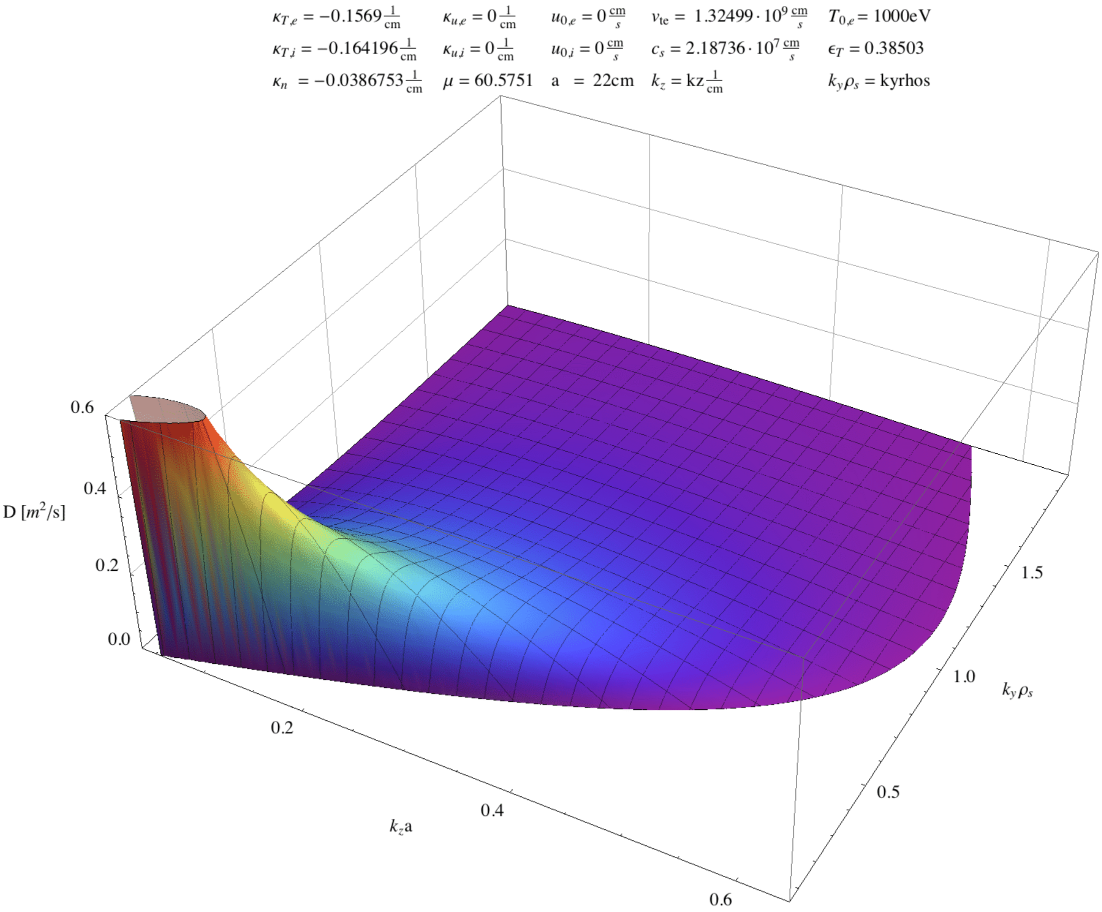

Figure 5.20: Diffusivity versus $k_z a$ and $k_y \rho_s$ with $\eta_i \approx 4.25$, $\eta_e \approx 4.06$, $u_{0,e} = 0$. - The three-dimensional plot clarifies the existence of one maximum in the considered range. The smaller parallel and perpendicular wave numbers become, the greater the diffusivity becomes.

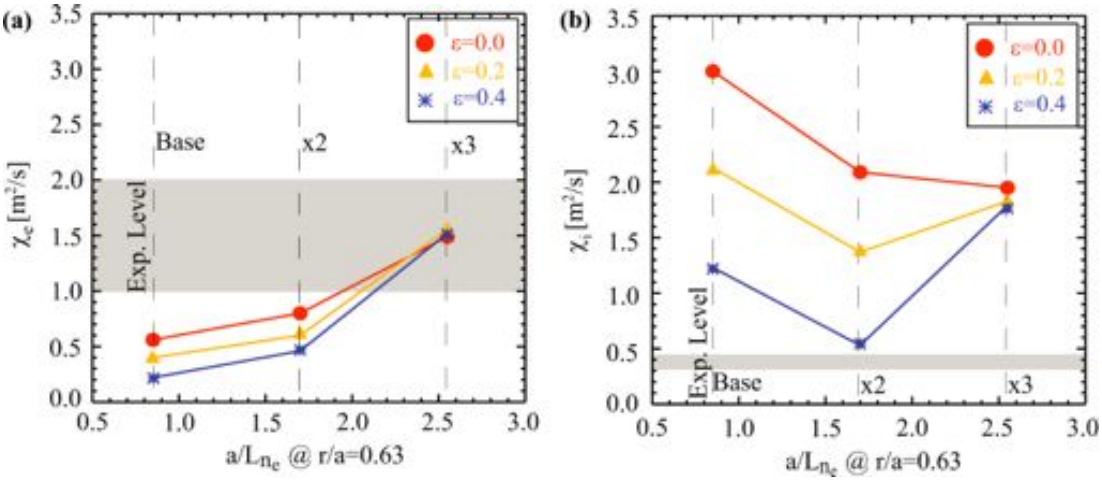

Figure 5.21: Thermal diffusivities - The shadowed regions correnspond to the experimental level. This plots show the impact of the reduction factor of a/L_{Ti}, ϵ. The thermal diffusivities χ_e and χ_i are averaged over $r/a \in [0.4, 0.6]$ (taken from Ref. [33]).

diffusion caused by the η_i-mode is $(0.19, 0.4899\,\mathrm{m^2s^{-1}})$ for $k_z a = 0.13$. The diffusivity caused by the current-driven drift wave is visible in the three-dimensional plots, figures B.2 and B.3, however, a higher electron current clarifies.

To illustrate the influence of a higher electron drift current on the diffusivity, $u_{0,e} = 12c_s$ is considered. The maximum diffusion caused by the current-driven drift wave is $(0.15, 0.2812\,\mathrm{m^2s^{-1}})$, which is only by a factor of 0.56 smaller than the maximum diffusion caused by the ion temperature gradient, $(0.19, 0.4994\,\mathrm{m^2s^{-1}})$, as depicted in figure 5.23.

In the three-dimensional plots, figures 5.24 and B.4, the influence of the drift wave driven by $u_{0,e} = 12c_s$ is obvious.

Without the strongly damping effect of the electron temperature gradient, the maximum diffusivity driven by the current-driven drift wave, $(0.15, 0.4575\,\mathrm{m^2s^{-1}})$, is even almost as high as the diffusivity caused by the η_i-mode, $(0.20, 0.5067\,\mathrm{m^2s^{-1}})$, as illustrated in figure 5.25.

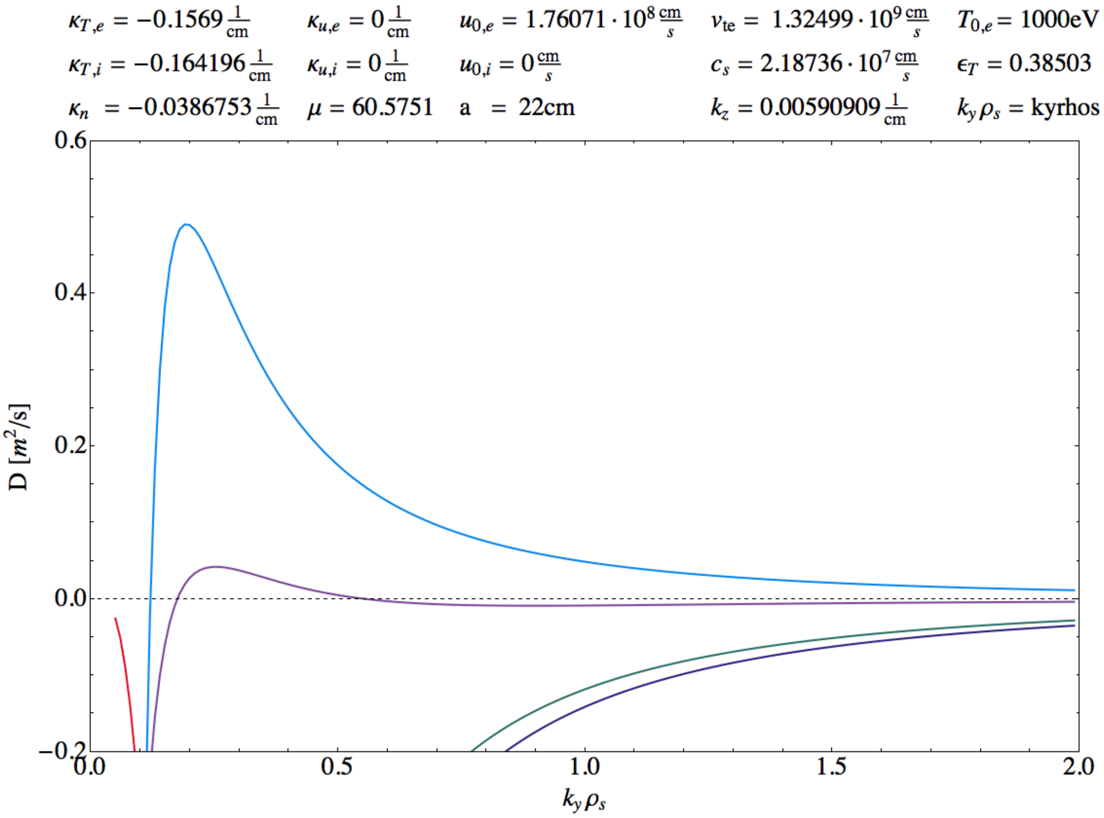

Figure 5.22: Diffusivity versus $k_y\rho_s$ with $\eta_i \approx 4.25$, $\eta_e \approx 4.06$, $u_{0,e} \approx 8c_s$. - The current-driven drift wave diffusion for a positive electron current of $u_{0,e} \approx 8c_s$, depicted in purple, results in a maximum of $(0.25, 0.0415\,\mathrm{m^2s^{-1}})$, which is a factor of 0.085 of the maximum resulting from the ion-temperature driven mode, $(0.19, 0.4899\,\mathrm{m^2s^{-1}})$, which is depicted in blue.

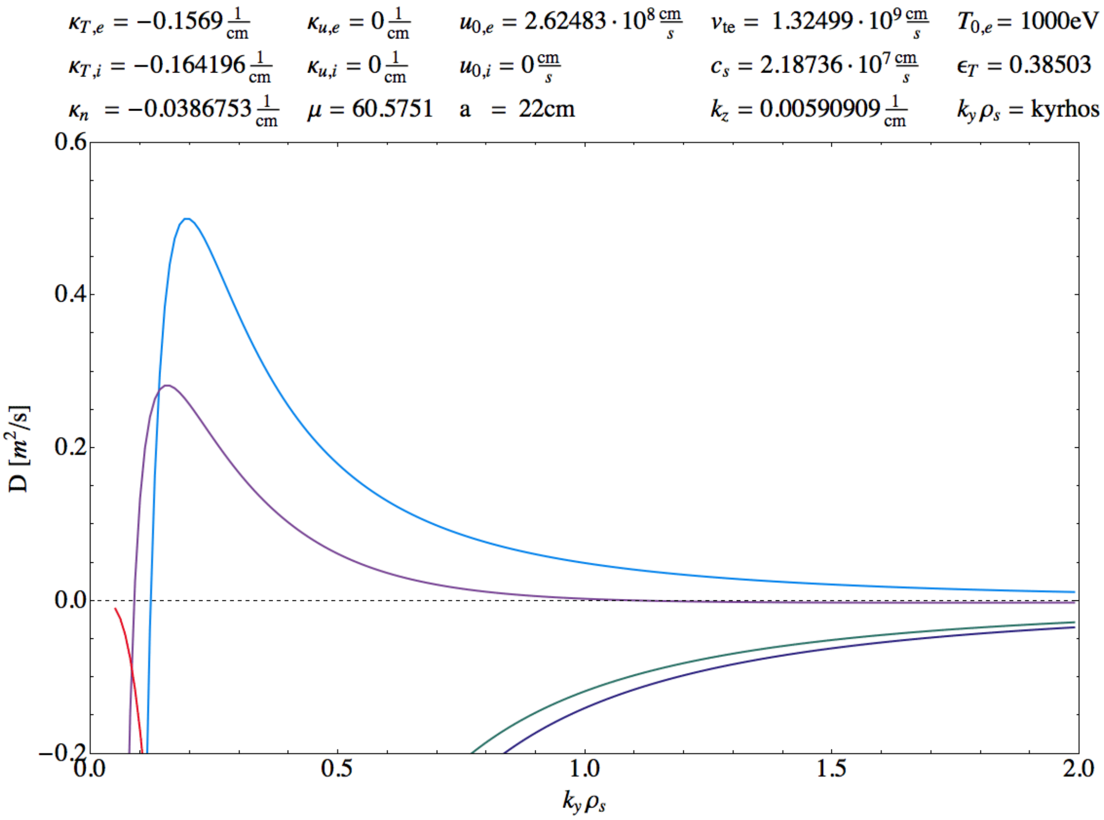

Figure 5.23: Diffusivity versus $k_y\rho_s$ with $\eta_i \approx 4.25$, $\eta_e \approx 4.06$, $u_{0,e} \approx 12c_s$. - The maximum diffusion caused by the current-driven drift wave with $u_{0,e} = 12c_s$ is $(0.15, 0.2812\,\mathrm{m}^2\mathrm{s}^{-1})$, which is only by a factor of 0.56 smaller than the maximum diffusion caused by the ion temperature gradient, $(0.19, 0.4994\,\mathrm{m}^2\mathrm{s}^{-1})$.

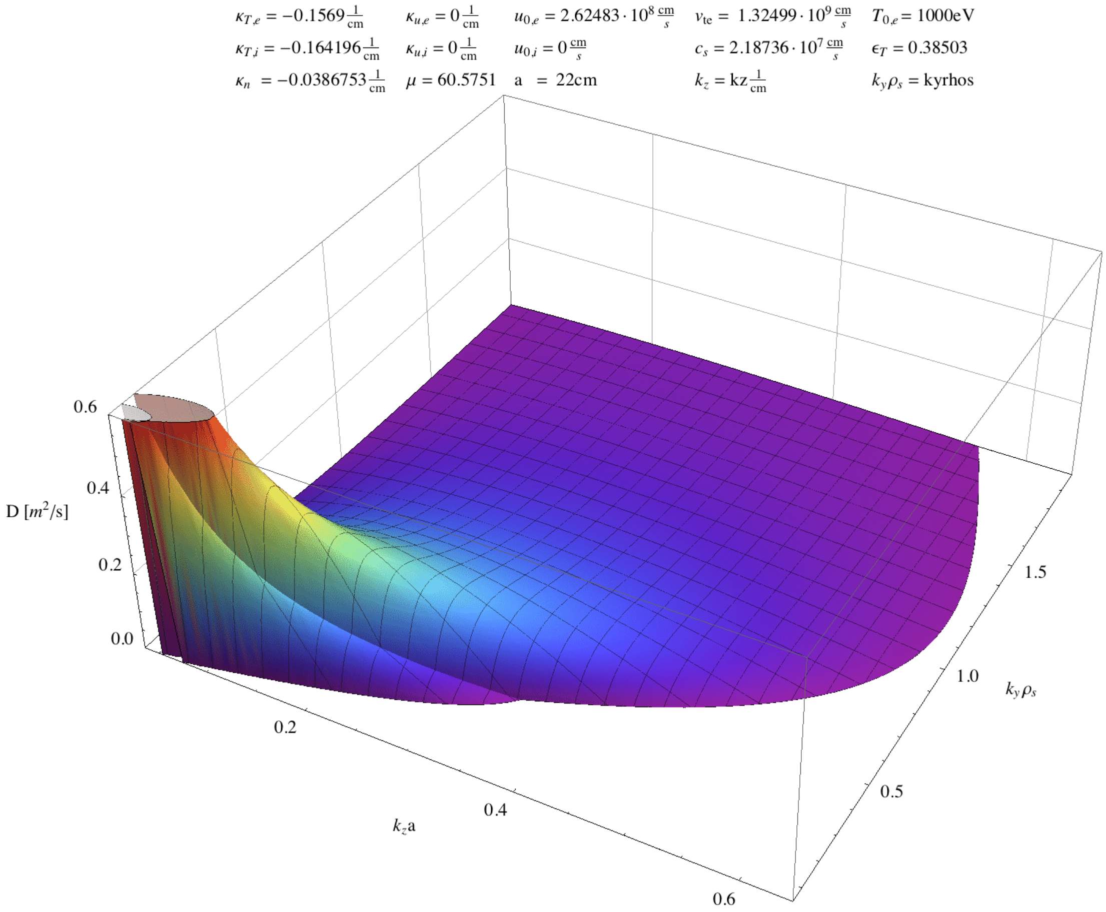

Figure 5.24: Diffusivity versus $k_z a$ and $k_y \rho_s$ with $\eta_i \approx 4.25$, $\eta_e \approx 4.06$, $u_{0,e} \approx 12$. - The three-dimensional view shows the two ridges, one resulting from the η_i-mode and the other one driven by the electron drift current. Figure 5.20, which has the same parameters but no electron current, shows the temperature-gradient driven diffusion separately.

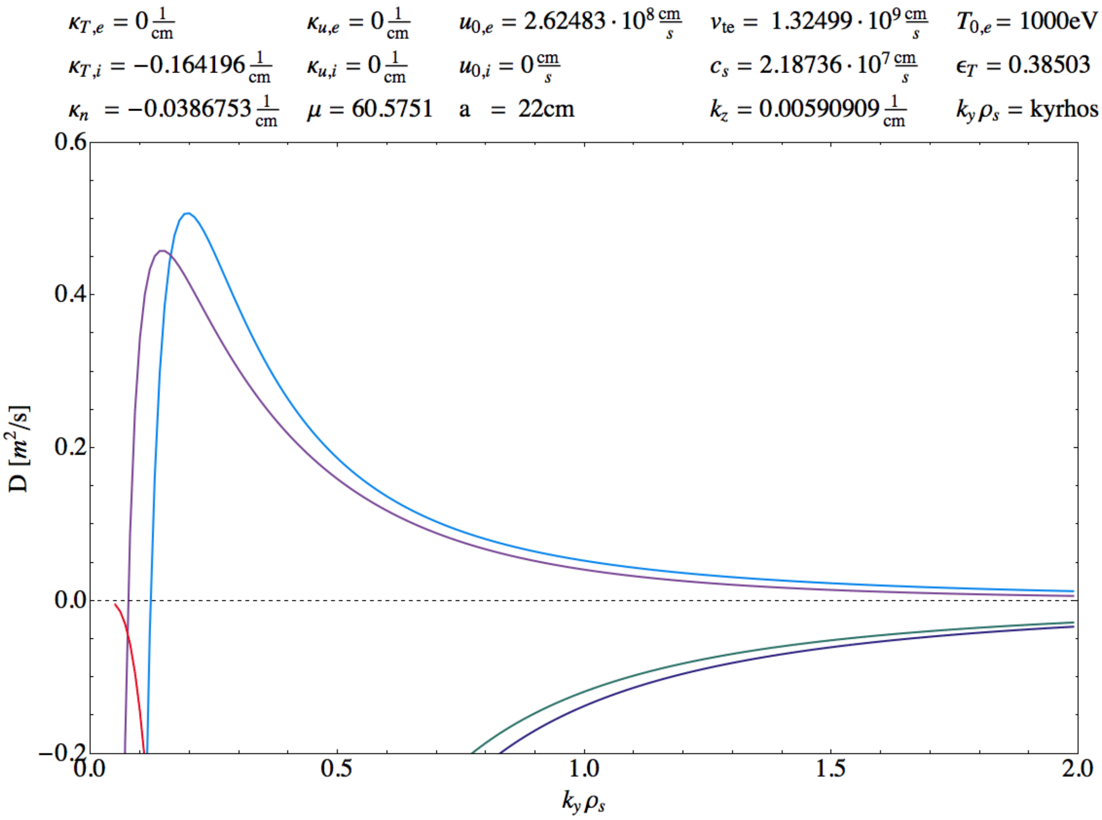

Figure 5.25: Diffusivity versus $k_y\rho_s$ with $\eta_i \approx 4.25$, $\eta_e = 0$, $u_{0,e} \approx 12c_s$. - Without the damping effect of the electron temperature gradient the maximum diffusivity driven by the current-driven drift wave, $(0.15, 0.4575\ \mathrm{m}^2\mathrm{s}^{-1})$, is 0.9 times as high as the maximum diffusion caused by the η_i-mode, $(0.20, 0.5067\ \mathrm{m}^2\mathrm{s}^{-1})$.

6

Summary and Conclusion

Following, the results of this work will be summarized, and new ideas for future work will be given.

6.1 Summary

Within this thesis, the impact of current-driven drift waves (CDDWs) and microturbulence in fusion energy devices was studied. After the derivation of two models, which describe drift waves and include electron currents, both were analyzed: the first model was studied analytically and the second, after the development of a program in Mathematica, numerically.

6.1.1 Models and analytic discussion

In chapter 3, different models for drift waves were developed and analyzed. First, the mechanism of drift waves and the requirements for instability were discussed. Subsequently, different models for describing drift waves were derived. Starting with adiabatic electrons and fluid ions, the drift wave velocity was derived. The

Hasegawa-Mima equation and the $i\delta$-model showed the inclusion of instabilities as well as the importance of ion polarization effects.

In section 3.2.2, the response of kinetic electrons to a small density disturbance was derived. For all considerations, a plane-plasma-slab geometry and electrostatics were assumed. In the equilibrium Maxwellian distribution function, the gradients of density and temperature in the $\hat{\mathbf{x}}$-direction, as well as a parallel current were considered. Finally, the electron response was achieved by applying the drift kinetic equation to the slab model. This drift wave model was closed by the quasi-neutrality condition and included fluid ions and kinetic electrons.

The second model describes both electrons and ions kinetically. Since in the derivation of the kinetic response, terms of the order of the ion polarization drift were neglected, an additional ion polarization density was provided. As finite-temperature ions should be included in the model, FLR-effects were absorbed by additional factors. By including these effects, the quasi-neutrality condition became:

$$\frac{\tilde{R}_e}{1+k_\perp^2\rho_e^2} = \frac{\tilde{R}_i}{1+k_\perp^2\rho_i^2}\frac{T_{0,e}}{T_{0,i}} + \frac{k_\perp^2\rho_s^2}{1+k_\perp^2\rho_i^2} \ .$$

The plasma dispersion function Z was approximated by a four-pole approximation, leading to 8 modes. In section 3.4, an analytic discussion on the basis of the first model, containing cold fluid ions and simplified drift-kinetic electrons, was provided. An influence of an electron current on the drift wave instability was predicted consistent with previous theories: a higher electron current leads to a higher growth rate, considered for positive $k_y\rho_s$ and k_z.

6.1.2 Drift parameter

In standard gyrokinetic derivations, which are expansions in $\rho_* = \rho/a$, the drift parameter

$$\frac{v_{drift}}{c_s} \sim \frac{\rho_*}{\beta}\frac{8a}{Rq} \ ,$$

is very small and therefore negligible compared to other modes in most cases. However, for larger ρ_* and small β, this parameter could become > 1. For a low density C-Mod case (table 3.1, $B = 5.2$T, $T_{0,e} = 1$keV, $a = 22$cm) we showed in section 3.3

$$\frac{u_{\|0}}{c_s} \approx 2.09279 \ .$$

This value is based on a model that contains magnetic shearing and non-circularity:

$$\frac{u_{\|0}}{c_s} = \frac{1}{nec_s}\frac{c}{2\pi}\frac{B_T}{qR}\left[1 - \frac{\hat{s}}{2} + \frac{\kappa^2 s_\kappa}{1+\kappa^2}\right]\frac{1+\kappa^2}{2\kappa} \ .$$

In the large aspect ratio circular limit the drift parameter is $u_{\|0}/c_s \approx 1.34612$, but a neglect of the magnetic shear parameter $\hat{s} = 0$ while allowing non-circularity leads to a drift parameter of

$$\frac{u_{\|0}}{c_s} \approx 8.05 \ ,$$

which is about four times higher than the original value including the shear parameter.

While this shows some of the sensitivity of the approximation on the included parameters, due to uncertainties in the values of $\hat{s}$ and other shaping effects, such as the Shafranov shift, even larger values of the drift parameter than $u_{\|0}/c_s \approx 8$ are possible. The location in the plasma could be another factor: closer to the plasma center, where the magnetic shear is much lower, the drift parameter may be larger. Also, in other experiments or considering lower densities, the CDDW may become more important.

Even if the parallel electron drift current is not high enough in most parts of the plasma, it is possible that MHD instabilities drive large local current densities at resonant surfaces. These currents might generate CDDWs as secondary instabilities. As shown in Ref. [26], even damped modes can contribute to nonlinear turbulent flux. Therefore, a marginally damped CDDW could generate a relevant diffusion.

6.1.3 Numeric discussion

To study CDDWs in more detail, a program based on Mathematica was developed, as described in chapter 4. The analytically derived response of kinetic ions and electrons could be verified. The program includes different dispersion relations: the previously mentioned kinetic-electron-fluid-ion-model and the kinetic-electron-kinetic-ion-model. Three- and four-pole approximations for Z are provided and growth rates can be entered manually, in order to compare an approximation with the provided models. The program includes the ability to plot growth rates, frequencies and the mixing-length diffusion and exports the results automatically in the filesystem, according to the chosen physical parameters.

While the programming was not strictly focused on minimizing runtime, automation of the application flow as well as the supply of interfaces for future development were stressed. This program was used for the numerical study of CDDWs, the results of which were provided in chapter 5. All studies were based on Alcator C-Mod parameters (see table 3.1) and used kinetic electrons and ions. The analytic prediction could be verified: a CDDW was found in the appropriate parameter range.

An ion-temperature driven mode could be identified and the influence of an electron-temperature gradient determined. Independently from these temperature gradients, the electron current drives an additional mode unstable. Symmetries of the growth rate, depending on the sign of $k_y \rho_s$ and the electron current, were shown.

Based on the mixing length approximation, diffusion caused by the CDDW was investigated and it was found that the diffusion can be in the order of magnitude of the experiments in some parameter regimes. For the baseline parameters in the C-Mod experiment, where $u_{0,e}/c_s \approx 2$, the CDDW is slightly damped in the local slab limit investigated in this thesis, and it is possible that the CDDW is not very important. However, there are uncertainties in various experimental parameters that could make the CDDW more important.

The CDDW diffusion was found to be more than $\sim 10\%$ of the mixing-length diffusion caused by ITG modes, if the drift parameter is $u_{0,e}/c_s \approx 8$ and higher, which could result for various reasons discussed in the previous section. Also, the relative importance of the CDDW compared to the ITG mode could increase if the actual ion temperature gradient is smaller than the present estimate. In the experiments this thesis is referring to, the ion temperature gradient was not directly measured and, as shown in figure 12 of Ref. [33], if the assumed ion temperature gradient was reduced by 30%, ITG turbulence was significantly reduced. The CDDW also depends on the electron temperature and density gradients, so 30% differences in those quantities from the apparent measurements could also give rise to a significant enhancement of the CDDW. In any case, there are probably other experiments, particularly at lower density or in smaller tokamaks, where the CDDW may be important. The inclusion of CDDWs in nonlinear gyrokinetic simulation codes should be taken into consideration for these parameters.

6.2 Future Work

In order to get more precise results, the developed Mathematica program could be extended in future work. Instead of a plane slab-model, a local model describing toroidally curved magnetic fields and trapped-electron effects could be considered. This could lead to deeper insight into the behavior of the CDDW. Since the program provides support for the additional consideration of a current gradient, in future work $\eta_u \neq 0$-cases can be studied.

Finally, it would be useful to add the parallel drift velocity from equilibrium currents to nonlinear gyrokinetic codes, as fully nonlinear calculations are needed to definitively investigate the importance of CDDWs. Although they might be unimportant in many plasma regimes, particularly in future larger machines and at higher plasma pressure, CDDWs could be important in understanding some existing experiments in smaller machines at low density.

In addition to extending the program, other parameter regimes could be studied to more precisely determine the range in which CDDWs are not negligible. This could be useful to exclude definitively the possibility of their impact on ITER or other future magnetic confinement fusion devices.

The idea leading to this thesis was based on a work of Lin et al. [33], where a study of CDDWs was proposed, as well as the examination of shorter wavelength turbulence in the range of $k_\theta \rho_s > 4$. While the study of CDDWs was clearly the main focus of this thesis, the consideration of shorter wavelength turbulence in the form of GYRO-simulations was started as well and will be continued in future work.

Bibliography

[1] JET, 2009. Available from: `http://www.micinn.es/stfls/MICINN/Investigacion/IMAGENES/4_Diagramadelprincipiotokamak(imagenJET).jpg` [cited 12/06/2011]. 27

[2] M. Abramowitz and I. A. Stegun. Modified Bessel functions I and K. In *Handbook of Mathematical Functions*, page 374 f. National Bureau of Standards, 1972. Available from: `http://people.math.sfu.ca/~cbm/aands/page_375.htm`. 56

[3] T. J. M. Boyd and J. J. Sanderson. Inhomogeneous magnetic field. In *The physics of plasmas*, chapter 2.4, page 19 ff. Cambridge University Press, 2003. Available from: `http://books.google.com/books?id=bAmqvuGTUJ4C`. 22

[4] T. J. M. Boyd and J. J. Sanderson. Introduction. In *The physics of plasmas*, chapter 1, page 1 ff. Cambridge University Press, 2003. Available from: `http://books.google.com/books?id=bAmqvuGTUJ4C`. 8

[5] P. Bradshaw. Possible origin of Prandtl's mixing-length theory. *Nature*, 249:135, 1974. Available from: `http://www.nature.com/nature/journal/v249/n5453/pdf/249135b0.pdf`. 33

[6] C. Brandt. *Active Control of Drift Wave Turbulence.* PhD thesis, 2009. Available from: `http://ub-ed.ub.uni-greifswald.de/opus/volltexte/2009/609/`. 37, 38, 39, 40

[7] F. Cap. Verteilungsfunktion im Phasenraum. In *Lehrbuch der Plasmaphysik und Magnetohydrodynamik*, chapter 4.1, page 62 ff. Springer, 1994. Available from: `http://books.google.com/books?id=prN8v5hc0sAC`. 23, 24

[8] F. F. Chen. Resistive Overstabilities and Anomalous "Diffusion". *Phys. Fluids*, 8(5):912–919, 1965. Available from: `http://www.ee.ucla.edu/~ffchen/Archive/Chen035.pdf`. 36

[9] W. D. Dorland. The Gyrokinetic-Poisson System. In *Gyrofluid Models of Plasma Turbulence*, chapter 2.1, page 18 ff. 1993. Available from: `http://w3.pppl.gov/~hammett/gyrofluid/papers/1993/dorland-thesis.pdf`. 56

[10] DPG. Trägheitseinschluss. Available from: `http://www.dpg-physik.de/dpg/gliederung/fv/p/info/pix/Pellet.jpg` [cited 12/05/2011]. 9

[11] DPG. Kraftwerk, 2011. Available from: `http://www.dpg-physik.de/dpg/gliederung/fv/p/info/pix/Kraftwerk.jpg` [cited 12/04/2011]. 5

[12] A. Einstein. Über die von der molekularkinetischen Theorie der Wärme geforderte Bewegung von in ruhenden Flüssigkeiten suspendierten Teilchen. *Annalen der Physik*, 322(8):549–560, 1905. Available from: `http://dx.doi.org/10.1002/andp.19053220806`, `doi:10.1002/andp.19053220806`. 31

[13] R. F. Ellis and E. Marden-Marshall. Comparison of local and nonlocal theories of the collisional drift instability. *Phys. Fluids*, 22(11):2137–

2139, 1979. Available from: `http://link.aip.org/link/doi/10.1063/1.862506`, `doi:10.1063/1.862506`. 40

[14] N. J. Fisch. Theory of current drive in plasmas. *Reviews of Modern Physics*, 59(1):175–234, 1987. Available from: `http://rmp.aps.org/pdf/RMP/v59/i1/p175_1`. 29

[15] J. P. Freidberg. The non-circular cross section tokamak. In *Plasma Physics and Fusion Energy*, chapter 13.7.4, page 398 ff. Cambridge University Press, 2007. Available from: `http://books.google.com/books?id=Vyoe88GEVz4C`. 28

[16] J. P. Freidberg. The spherical tokamak. In *Plasma Physics and Fusion Energy*, chapter 13.7.5, page 411 ff. Cambridge University Press, 2007. Available from: `http://books.google.com/books?id=Vyoe88GEVz4C`. 29

[17] C. Gardiner. Brownian Motion. In *Handbook of Stochastik Methods*, chapter 1.2.1, page 2 ff. Springer, 1997. 31

[18] R. J. Goldston and P. H. Rutherford. “Collisionless” drift waves. In *Plasma Physics*, chapter 26.3, page 457. Taylor & Francis Group, 1995. 62

[19] R. J. Goldston and P. H. Rutherford. Momentum balance equation. In *Introduction to Plasma Physics*, chapter 6.2, page 86 ff. Taylor & Francis Group, 1995. 25

[20] R. J. Goldston and P. H. Rutherford. Particle drifts in non-uniform magnetic fields. In *Plasma Physics*, chapter 3, page 29 ff. Taylor & Francis Group, 1995. 22

[21] R. J. Goldston and P. H. Rutherford. The drift-kinetic equation and kinetic drift waves. In *Introduction to Plasma Physics*, chapter 26, page 449 ff. Taylor & Francis Group, 1995. 49

[22] M. Greenwald, R. Boivin, P. Bonoli, and Others. Studies of EDA H-mode in Alcator C-Mod. *Plasma Physics and Controlled Fusion*, 42:A263, 2000. Available from: `http://stacks.iop.org/0741-3335/42/i=5A/a=331`. 61

[23] G. W. Hammett. Fluid Moment Models for Landau Damping with Application to the Ion-Temperature-Gradient Instability. *Physical Review Letters, Volume 64, No 25*, 1990. 57, 71

[24] G. W. Hammett. Private discussion, 2011. 34, 42

[25] A. Hasegawa and K. Mima. Pseudo-three-dimensional turbulence in magnetized nonuniform plasma. *Phys. Fluids*, 21(1):87, 1978. `doi:10.1063/1.862083`. 45

[26] D. Hatch, P. Terry, F. Jenko, F. Merz, and W. Nevins. Saturation of Gyrokinetic Turbulence through Damped Eigenmodes. *Physical Review Letters*, 106(11):1–4, Mar. 2011. Available from: `http://link.aps.org/doi/10.1103/PhysRevLett.106.115003`, `doi:10.1103/PhysRevLett.106.115003`. 126

[27] W. Horton. Drift waves and transport. *Rev. Mod. Phys.*, 71(3):735–778, Apr. 1999. Available from: `http://link.aps.org/doi/10.1103/RevModPhys.71.735`, `doi:10.1103/RevModPhys.71.735`. 34, 37, 46

[28] M. Kotschenreuther, W. Dorland, M. a. Beer, and G. W. Hammett. Quantitative predictions of tokamak energy confinement from first-principles simu-

lations with kinetic effects. *Physics of Plasmas*, 2(6):2381–2389, 1995. Available from: `http://link.aip.org/link/?PHP/2/2381/1`, `doi:10.1063/1.871261`. 34

[29] J. A. Krommes. The Gyrokinetic Description of Microturbulence in Magnetized Plasmas. *Annu. Rev. Fluid Mech.*, 44:175–201, 2012. Available from: `http://www.annualreviews.org/doi/abs/10.1146/annurev-fluid-120710-101223`, `doi:10.1146/annurev-fluid-120710-101223`. 47

[30] I. Langmuir. Oscillations in ionized gases. *Proceedings of the National Academy of Sciences*, 14:627–637, 1928. Available from: `http://www.pnas.org/content/14/8/627`. 1

[31] J. D. Lawson. Some Criteria for a Power Producing Thermonuclear Reactor. *Proceedings of the Physical Society. Section B*, 70(6):6–10, Jan. 1957. Available from: `http://stacks.iop.org/0370-1301/70/i=1/a=303`, `doi:10.1088/0370-1301/70/1/303`. 6

[32] W. W. Lee. Gyrokinetic approach in particle simulation. *Phys. Fluids*, 26(2):556, 1983. Available from: `http://link.aip.org/link/doi/10.1063/1.864140`, `doi:10.1063/1.864140`. 45

[33] L. Lin, M. Porkolab, E. M. Edlund, J. C. Rost, M. Greenwald, N. Tsujii, J. Candy, R. E. Waltz, and D. R. Mikkelsen. Studies of turbulence and transport in Alcator C-Mod ohmic plasmas with phase contrast imaging and comparisons with gyrokinetic simulations. *Plasma Physics and Controlled Fusion*, 51(6):065006, June 2009. Available from: `http://stacks.iop.org/`

`0741-3335/51/i=6/a=065006`, `doi:10.1088/0741-3335/51/6/065006`. 9, 10, 11, 60, 67, 93, 115, 118, 127, 128

[34] N. Mahdizadeh. Microinstabilities in a magnetically confined plasma. In *Investigation of Three-Dimensional Turbulent Structures in the Torsatron TJ-K*, chapter 2.3, page 10 ff. 2007. Available from: `http://elib.uni-stuttgart.de/opus/volltexte/2007/2984/`. 41

[35] Max-Planck-Institut für Plasmaphysik. Ignition conditions. Available from: `http://www.ipp.mpg.de/ippcms/eng/images/pic/images_bereiche/allgemein/380x265/zuendbedingung.gif` [cited 12/05/2011]. 7

[36] Max-Planck-Institut für Plasmaphysik. Wendelstein 7-X. Available from: `http://www.ipp.mpg.de/ippcms/eng/images/pic/images_bereiche/w7x/380x265/grafik_stellarator_2.gif` [cited 02/12/2011]. 30

[37] Max Planck Institute for Gravitational Physics. Einstein online. Available from: `http://www.einstein-online.info/spotlights/binding_energy#daten` [cited 12/05/2011]. 3

[38] F. Merz and F. Jenko. Nonlinear Saturation of Trapped Electron Modes via Perpendicular Particle Diffusion. *Phys. Rev. Lett.*, 100(3):2–5, Jan. 2008. Available from: `http://link.aps.org/doi/10.1103/PhysRevLett.100.035005`, `doi:10.1103/PhysRevLett.100.035005`. 34

[39] V. Naulin and K. H. Spatschek. Nonlinear drift-wave structures and their influence on particle transport. *Phys. Rev. E*, 55(5):5883–5893, May 1997. Available from: `http://link.aps.org/doi/10.1103/PhysRevE.55.5883`, `doi:10.1103/PhysRevE.55.5883`. 33

[40] A. Piel. The Energy Source of Stars. In *Plasma Physics: An Introduction to Laboratory, Space and Fusion Plasmas*, chapter 1.2.1, page 4 f. Springer, 2010. Available from: `http://books.google.com/books?id=wW1Q4Qz5hcwC`. 2

[41] B. Scott. The nonlinear drift wave instability and its role in tokamak edge turbulence. *New Journal of Physics*, 4:52, July 2002. Available from: `http://stacks.iop.org/1367-2630/4/i=1/a=352`, `doi:10.1088/1367-2630/4/1/352`. 38

[42] D. R. Smith. NSTX schematic. Available from: `http://homepages.cae.wisc.edu/~drsmith/images/nstx_schematic.jpg` [cited 02/12/2011]. 29

[43] S. A. Smith. Model Equations. In *Dissipative Closures for Statistical Moments, Fluid Moments, and Subgrid Scales in Plasma Turbulence*, chapter 5.1, page 80 ff. 1997. Available from: `http://w3.pppl.gov/~hammett/sasmith/thesis.html`. 45

[44] W. M. Stacey. *Fusion: An Introduction to the Physics and Technology of Magnetic Confinement Fusion*. Physics textbook. Wiley-VCH, 2010. Available from: `http://books.google.com/books?id=__mc3_ff9qYC`. 4

[45] T. H. Stix. Highlights in Early Stellarator Research at Princeton. *J. Plasma Fusion Res.*, 1:3–8, 1998. Available from: `http://www.jspf.or.jp/JPFRS/PDF/Vol1/jpfrs1998_01-003.pdf`. 30

[46] D. P. Stotler, W. T. Reiersen, and G. Bateman. ASPECT: an advanced specified-profile evaluation code for tokamaks. *Comp. Phys. Comm.*, 81:261–291, 1994. Available from: `http://dx.doi.org/10.1016/0010-4655(94)90124-4`. 60

[47] U. Stroth. Die Driftwelle. In *Plasmaphysik - Phänomene, Grundlagen, Anwendungen*, chapter 15.3, page 436 ff. Vieweg+Teubner Verlag, 2011. Available from: `http://books.google.com/books?id=p6xcX_I33kMC`. 39, 48

[48] U. Stroth. Herleitung der Flüssigkeitsgleichungen. In *Plasmaphysik - Phänomene, Grundlagen, Anwendungen*, chapter 7.4, page 217 ff. Vieweg+Teubner Verlag, 2011. Available from: `http://books.google.com/books?id=p6xcX_I33kMC`. 25

[49] U. Stroth. Lineare Instabilitäten. In *Plasmaphysik - Phänomene, Grundlagen, Anwendungen*, chapter 15.2.3, page 431. Vieweg+Teubner Verlag, 2011. Available from: `http://books.google.com/books?id=p6xcX_I33kMC`. 33

[50] U. Stroth. Turbulenter Transport. In *Plasmaphysik - Phänomene, Grundlagen, Anwendungen*, chapter 15, page 413. Vieweg+Teubner Verlag, 2011. Available from: `http://books.google.com/books?id=p6xcX_I33kMC`. 31

[51] R. E. Waltz, G. M. Staebler, W. Dorland, G. W. Hammett, M. Kotschenreuther, and J. Konings. A gyro-Landau-fluid transport model. *Physics of Plasmas*, 4(7):2482, 1997. Available from: `http://link.aip.org/link/?PHP/4/2482/1`, `doi:10.1063/1.872228`. 34

Appendix A

Growth Rates Studies

This section contains additional figures for the study of the influence of a current on the growth rates of drift waves, provided in section 5.

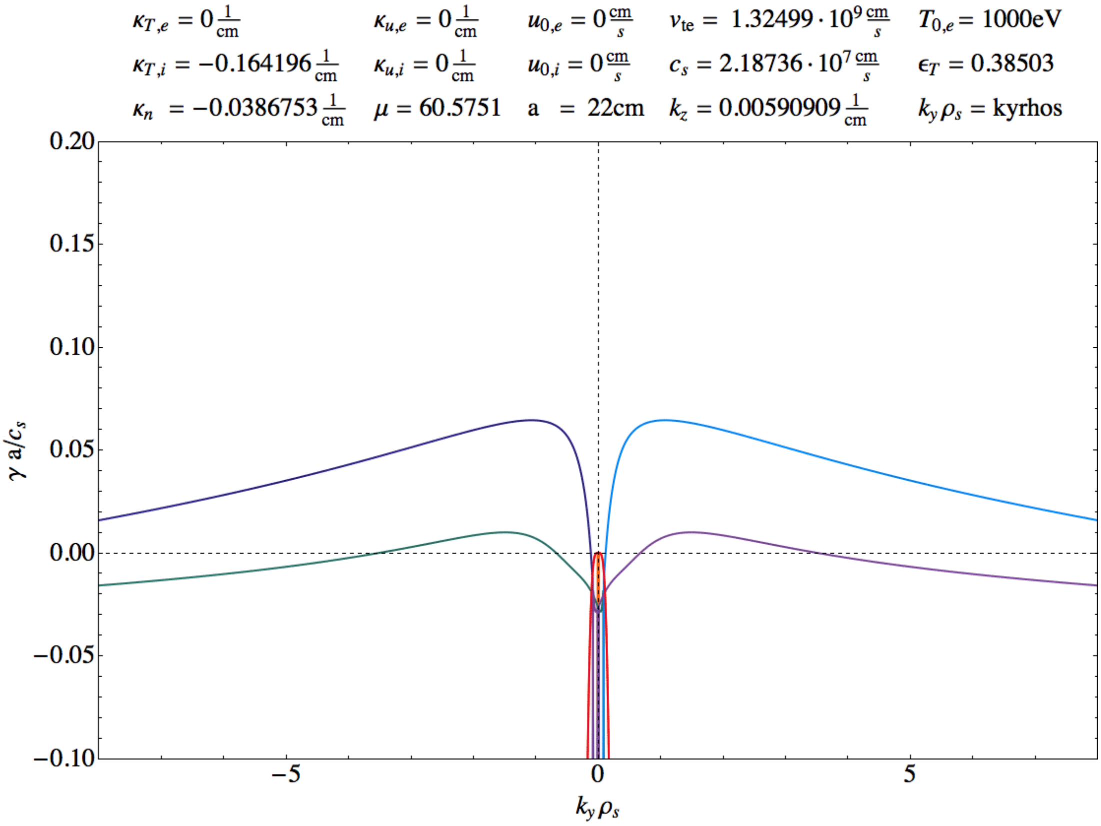

Figure A.1: Growth rate versus $k_y\rho_s$ with $\eta_i \approx 4.25$, $\eta_e = 0$, $u_{0,e} = 0$. - Corresponding to figure 5.3, this plot shows the axial symmetry, which is preserved for a density gradient and additional electron- and/or ion temperature gradients.

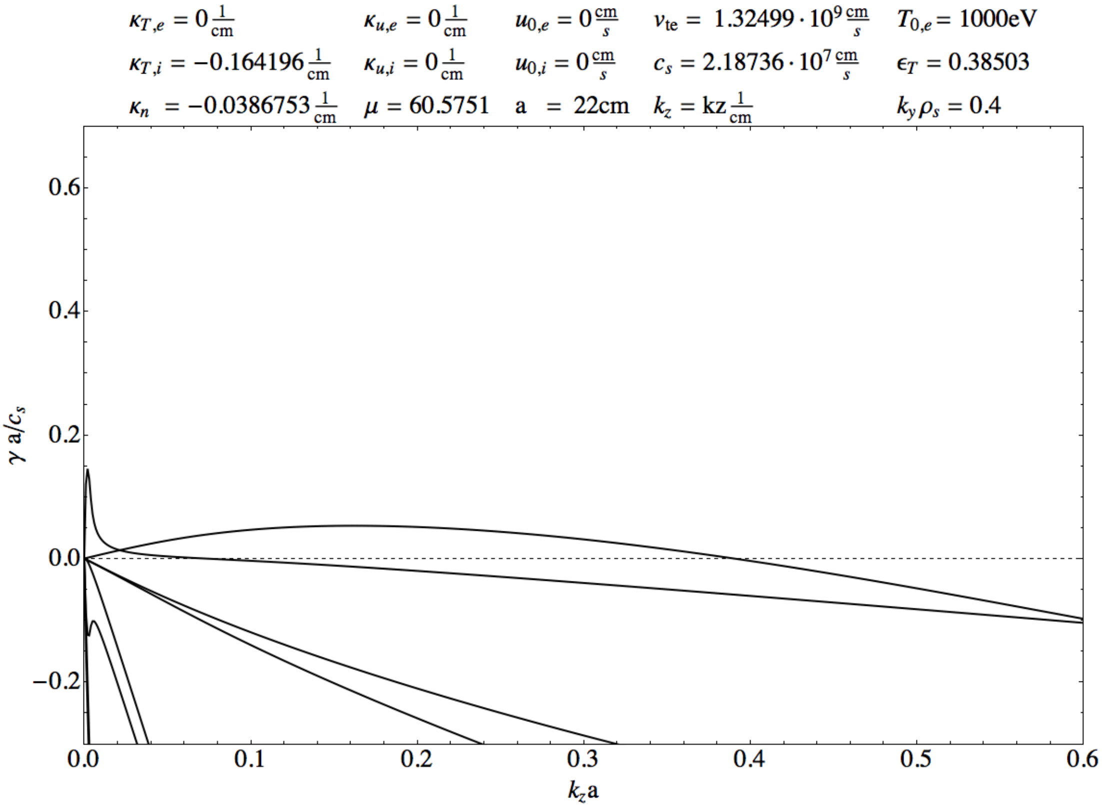

Figure A.2: Growth rate versus k_za with $\eta_i \approx 4.25$, $\eta_e = 0$, $u_{0,e} = 0$. - The ion temperature gradient gives rise to an additional unstable mode. This plot shows corresponding to figure A.1 the parallel wave number direction.

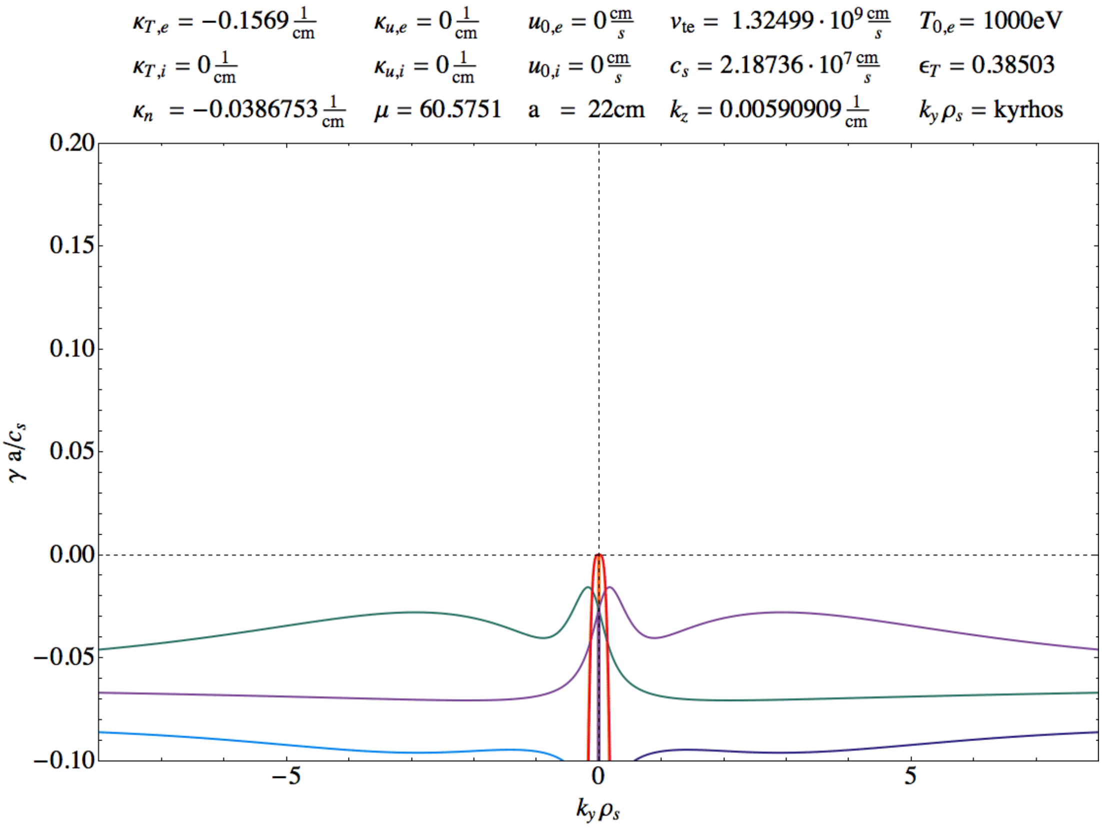

Figure A.3: Growth rate versus $k_y\rho_s$ with $\eta_i = 0$, $\eta_e \approx 4.06$, $u_{0,e} = 0$. - Corresponding to figure 5.4, the growth rate is axial symmetric for $\pm k_y\rho_s$. In figure A.4 the growth rate versus the parallel wavenumber is illustrated for this set of parameters.

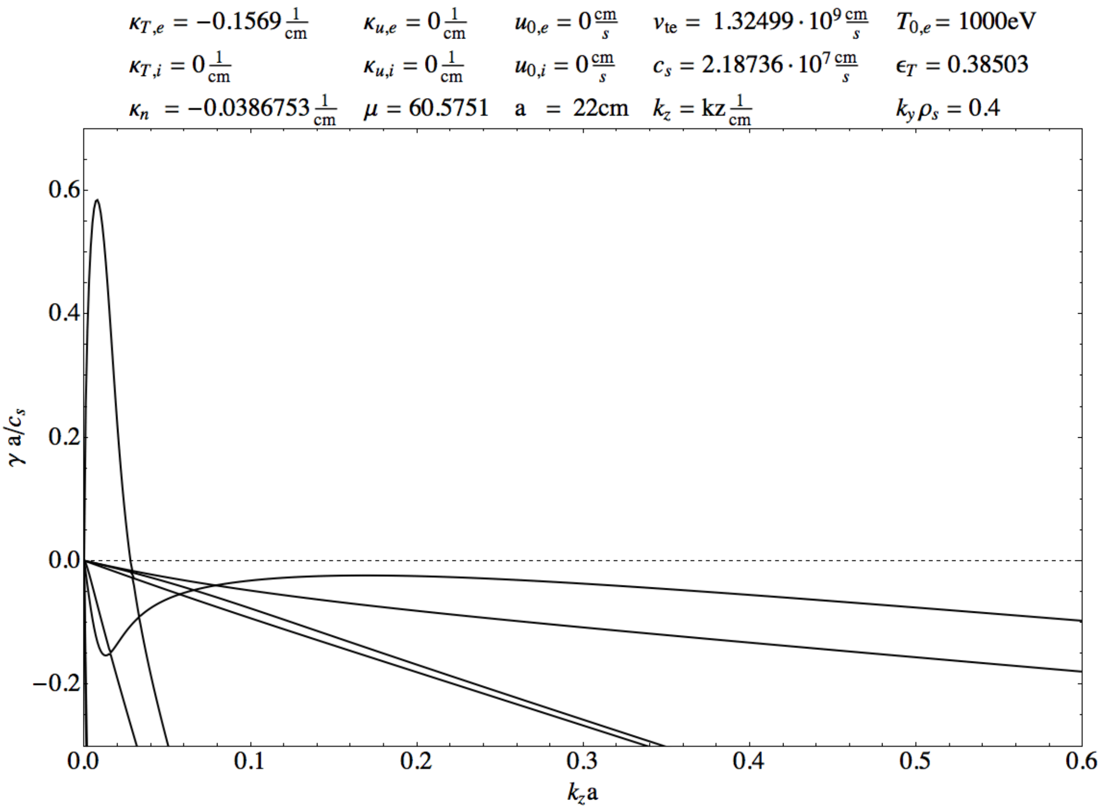

Figure A.4: Growth rate versus $k_z a$ with $\eta_i = 0$, $\eta_e \approx 4.06$, $u_{0,e} = 0$. - The electron temperature gradient with $\eta_e = 4.05685$ causes a damping of the mode. This figure corresponds to figures 5.4 and A.3, that show the perpendicular wave number direction.

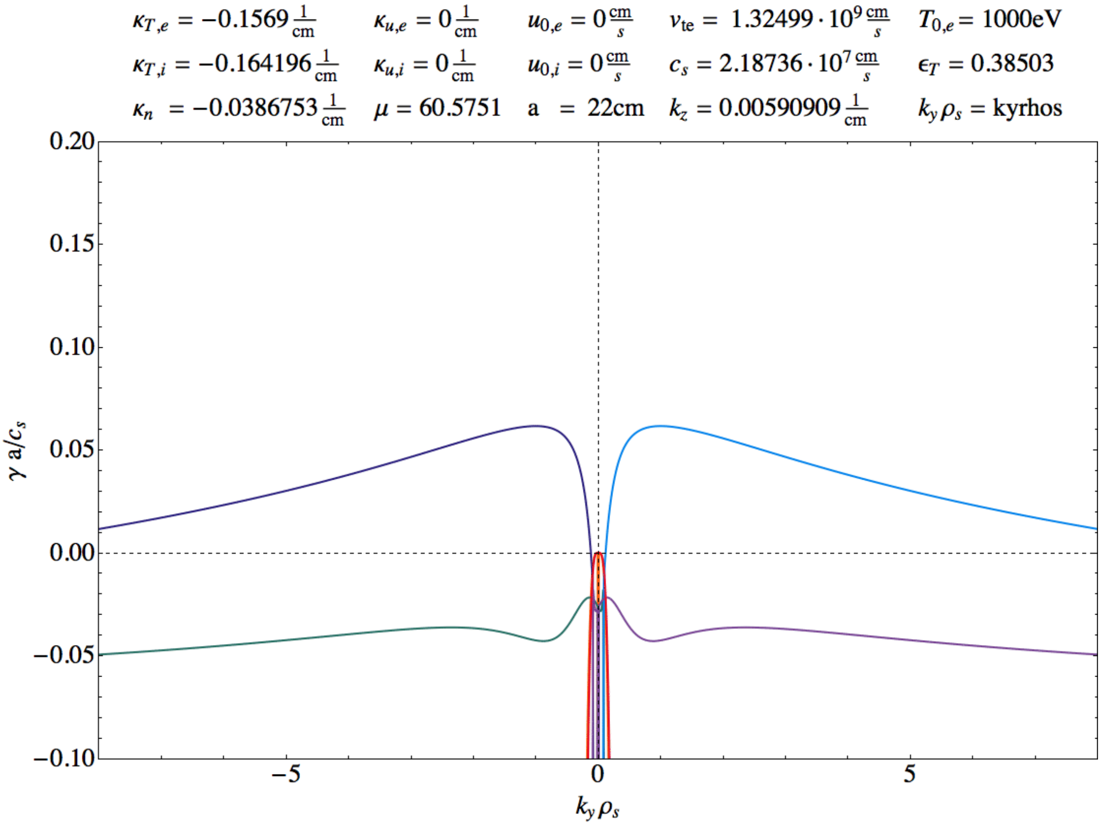

Figure A.5: Growth rate versus $k_y\rho_s$ with $\eta_i \approx 4.25$, $\eta_e \approx 4.06$, $u_{0,e} = 0$. - The growth rate is axially symmetric for a gradient of ion and electron temperature. The parallel wavenumber direction is shown in figure A.6 and three-dimensional plots in figures A.7 and 5.6.

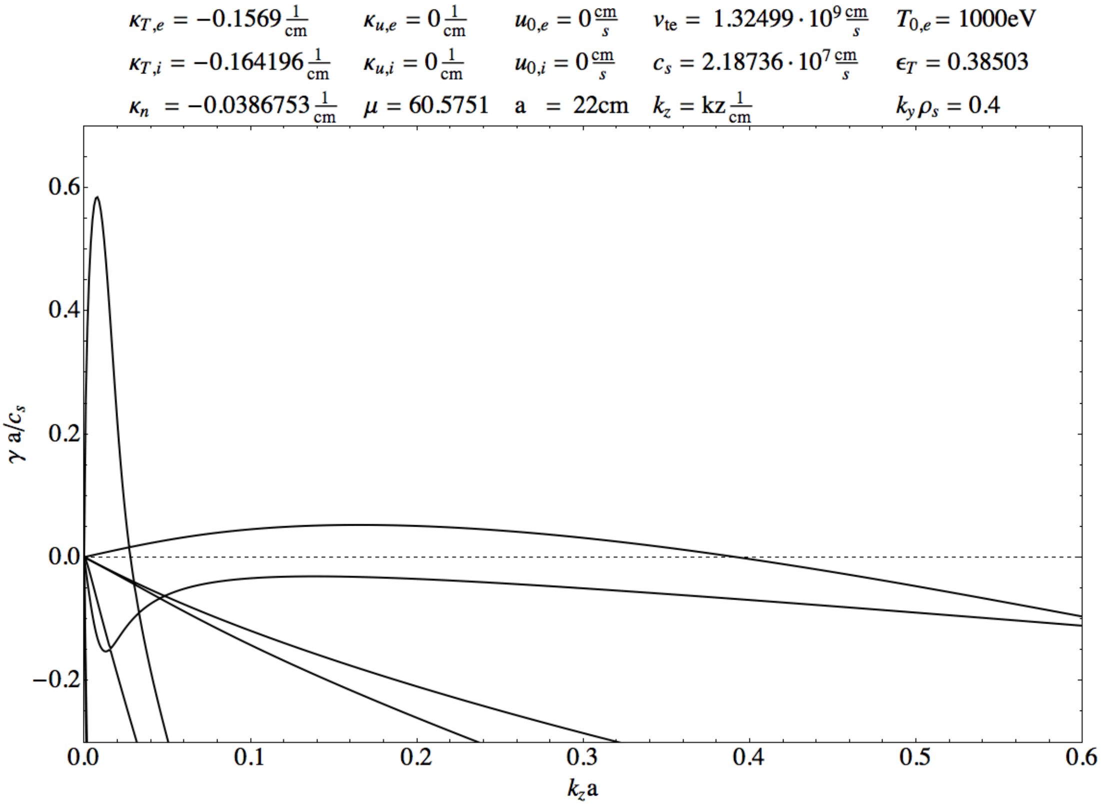

Figure A.6: Growth rate versus $k_z a$ with $\eta_i \approx 4.25$, $\eta_e \approx 4.06$, $u_{0,e} = 0$. - Corresponding to figure 5.5 and A.5, this plot shows the behavior in the parallel wavelength direction.

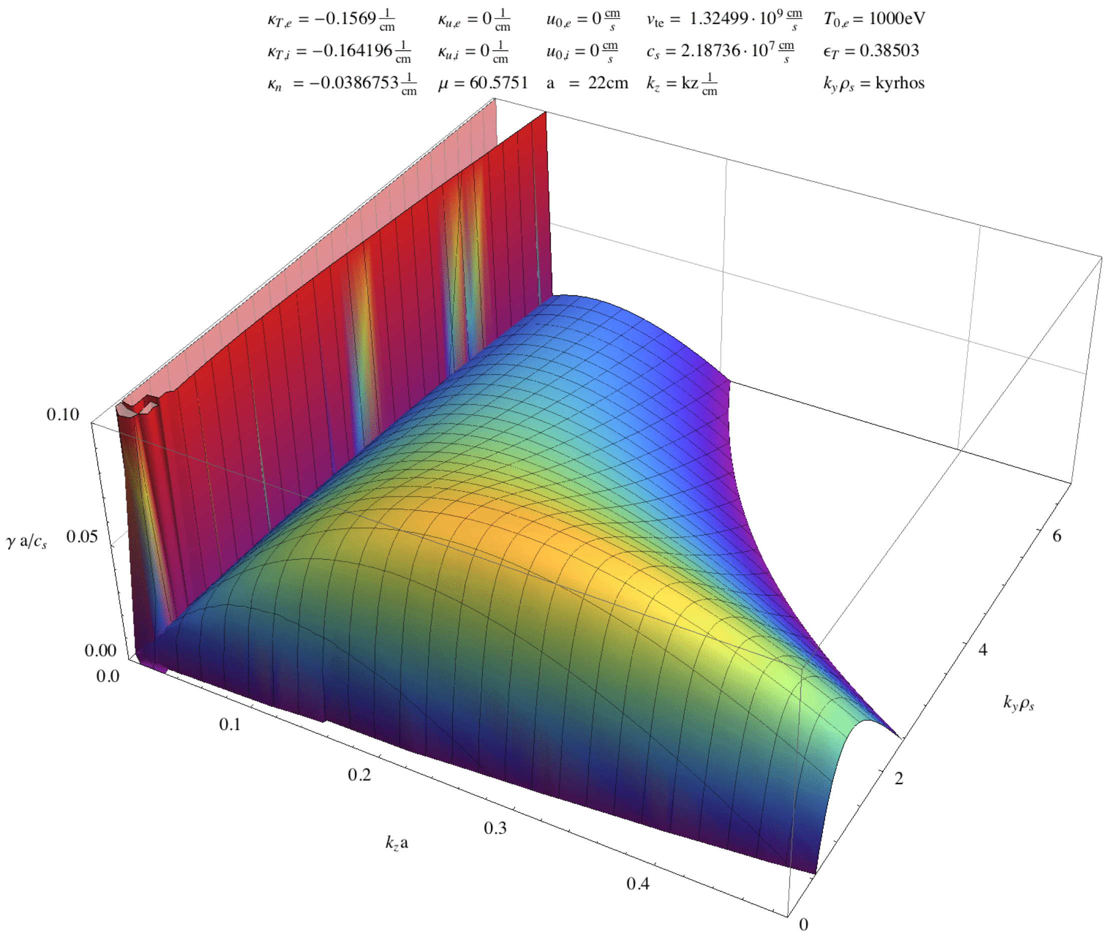

Figure A.7: Growth rate versus $k_z a$ and $k_y \rho_s$ with $\eta_i \approx 4.25$, $\eta_e \approx 4.06$, $u_{0,e} = 0$. - This plot is a detail of figure 5.6.

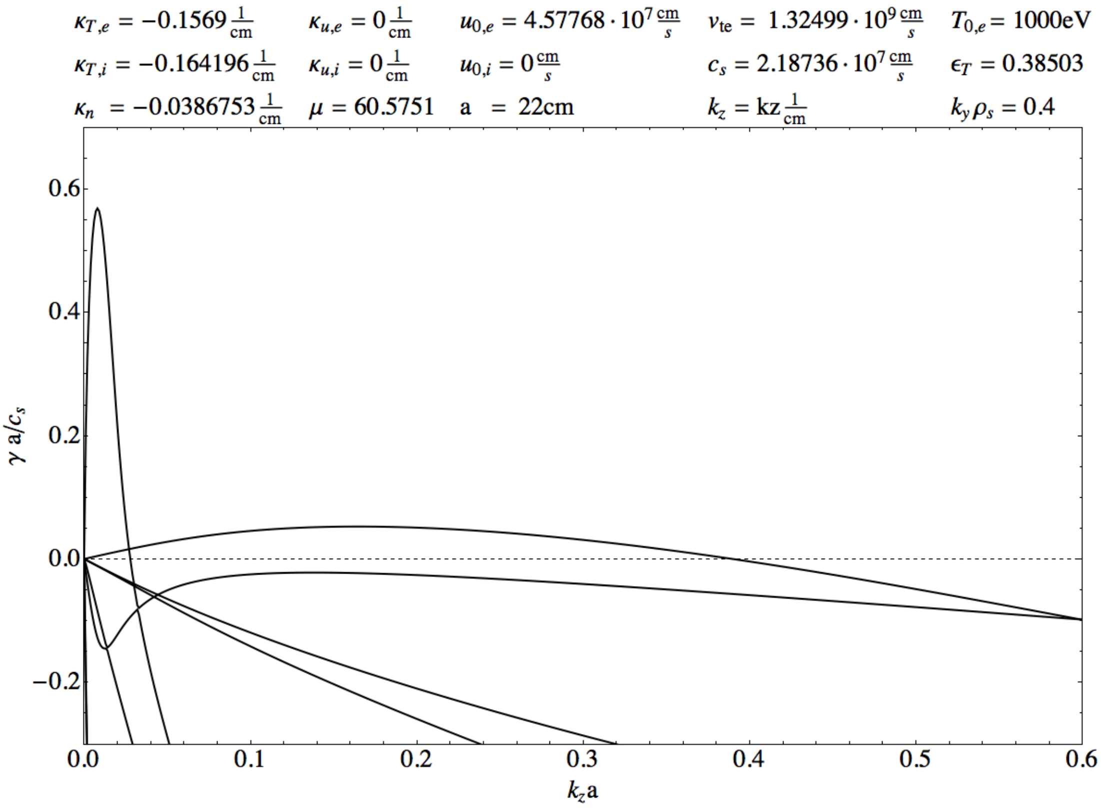

Figure A.8: Growth rate versus $k_z a$ with $\eta_i \approx 4.25$, $\eta_e \approx 4.06$, $u_{0,e} \approx 2c_s$. - This plot corresponds to figure 5.7, showing the parallel wave number direction.

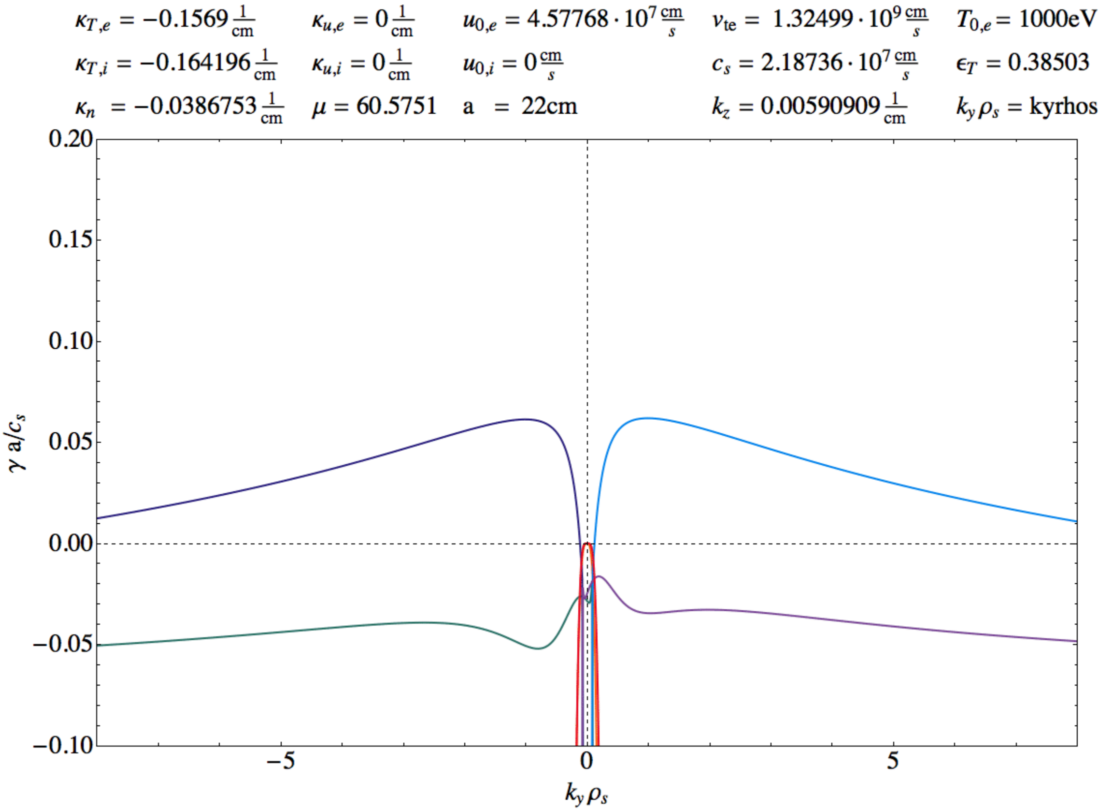

Figure A.9: Growth rate versus $k_y\rho_s$ with $\eta_i \approx 4.25$, $\eta_e \approx 4.06$, $u_{0,e} \approx 2c_s$. - Comparing with for example figure A.5, the additional electron current, $u_{0,e} \approx 2c_s$, illustrated in purple, breaks the symmetry in $k_y\rho_s$. This figure corresponds to figure 5.7, extended to negative $k_y\rho_s$.

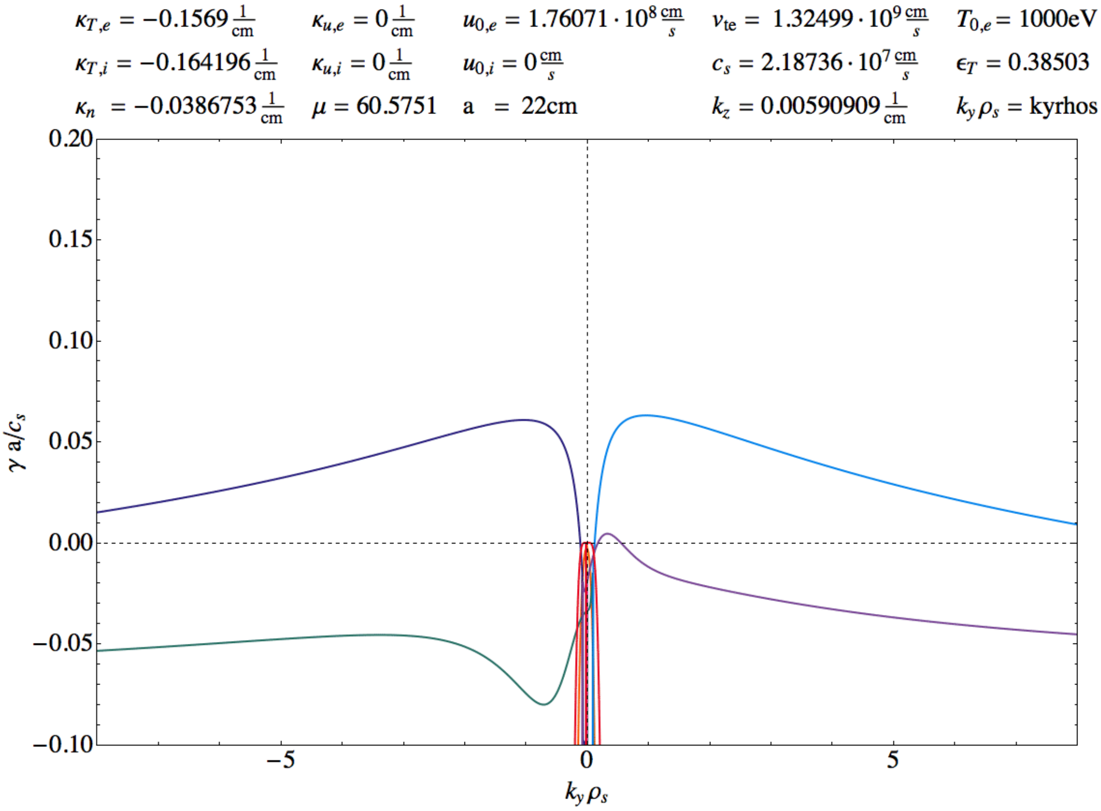

Figure A.10: Growth rate versus $k_y\rho_s$ with $\eta_i \approx 4.25$, $\eta_e \approx 4.06$, $u_{0,e} \approx 8c_s$. - An electron drift current of $u_{0,e} \approx 8c_s$ drives the electron drift wave mode unstable. The maxima are at $(0.96, 0.063)$ for the η_i-mode (blue) and at $(0.33, 0.0045)$ for the electron-current-driven mode (purple). This figure corresponds to figure 5.8, extended to negative $k_y\rho_s$.

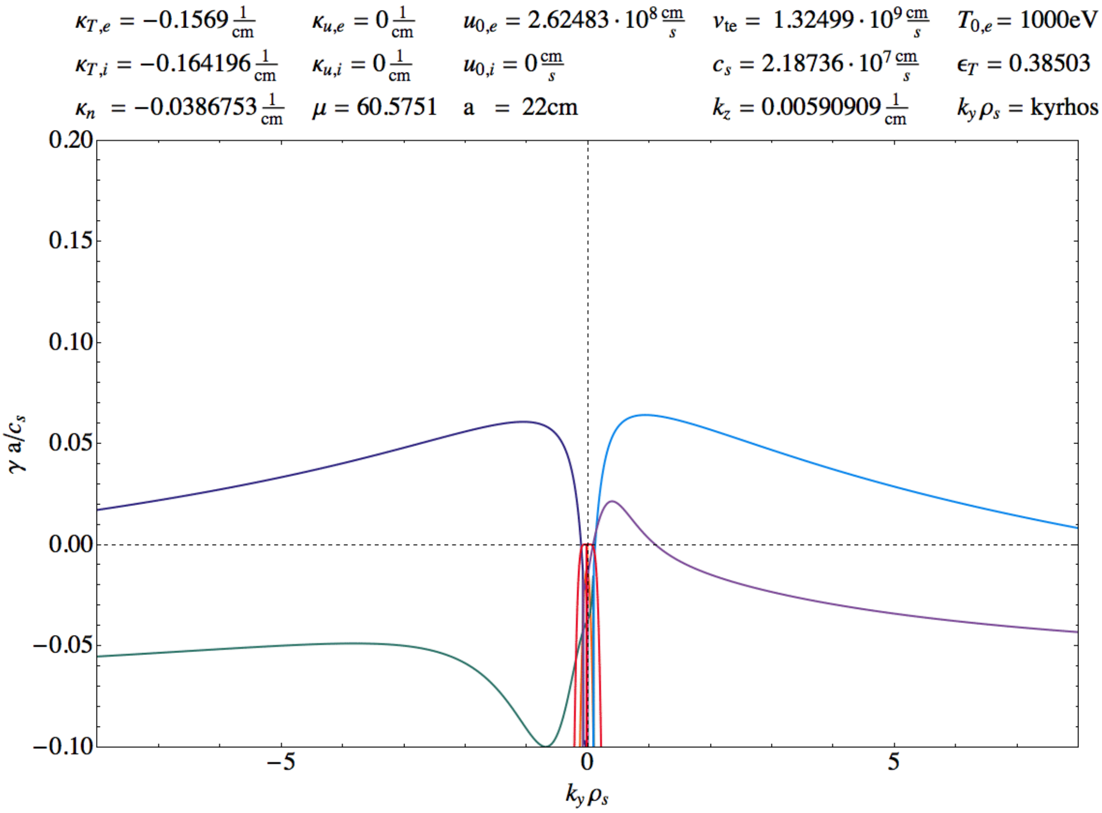

Figure A.11: Growth rate versus $k_y\rho_s$ with $\eta_i \approx 4.25$, $\eta_e \approx 4.06$, $u_{0,e} \approx 12c_s$. - An electron drift current of $u_{0,e} \approx 12c_s$ raises the current-driven drift wave to $(0.4, 0.021)$, which is only by a factor of 0.33 smaller than the maximum of the η_i-mode, $(0.94, 0.064)$. This figure corresponds to figure 5.9, extended to negative $k_y\rho_s$.

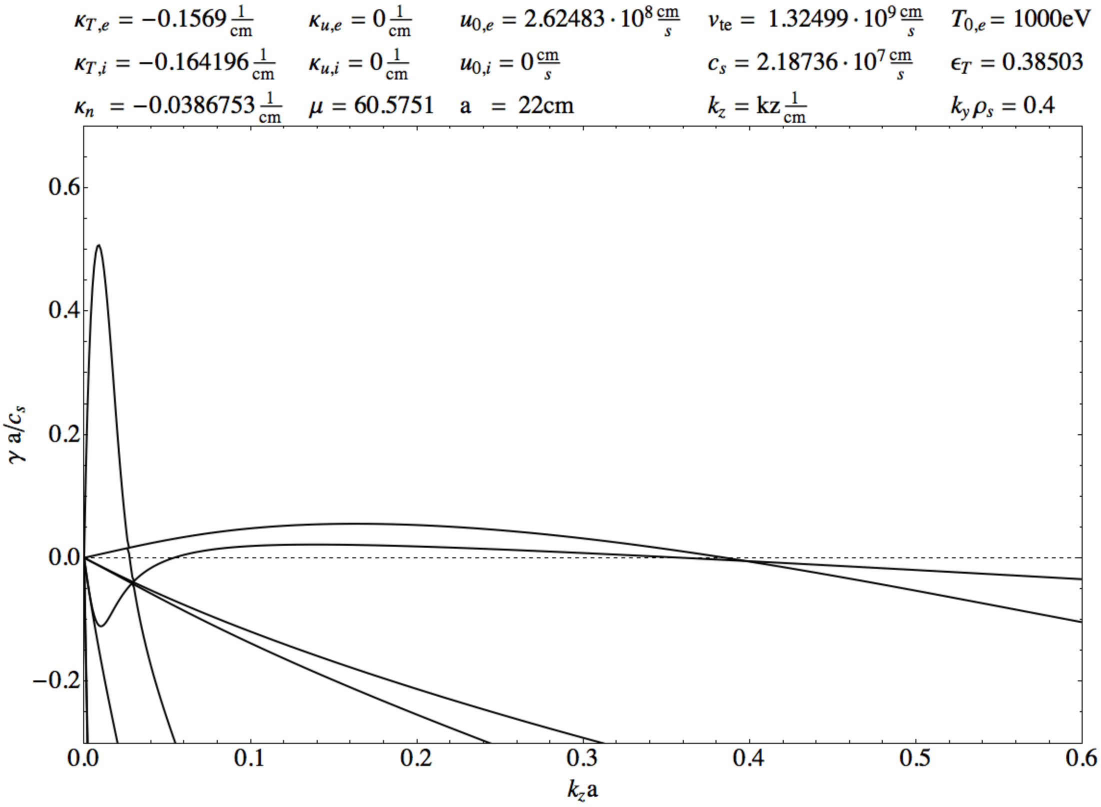

Figure A.12: Growth rate versus $k_z a$ with $\eta_i \approx 4.25$, $\eta_e \approx 4.06$, $u_{0,e} \approx 12 c_s$. - This plot corresponds to figure A.11, showing the parallel wave number direction.

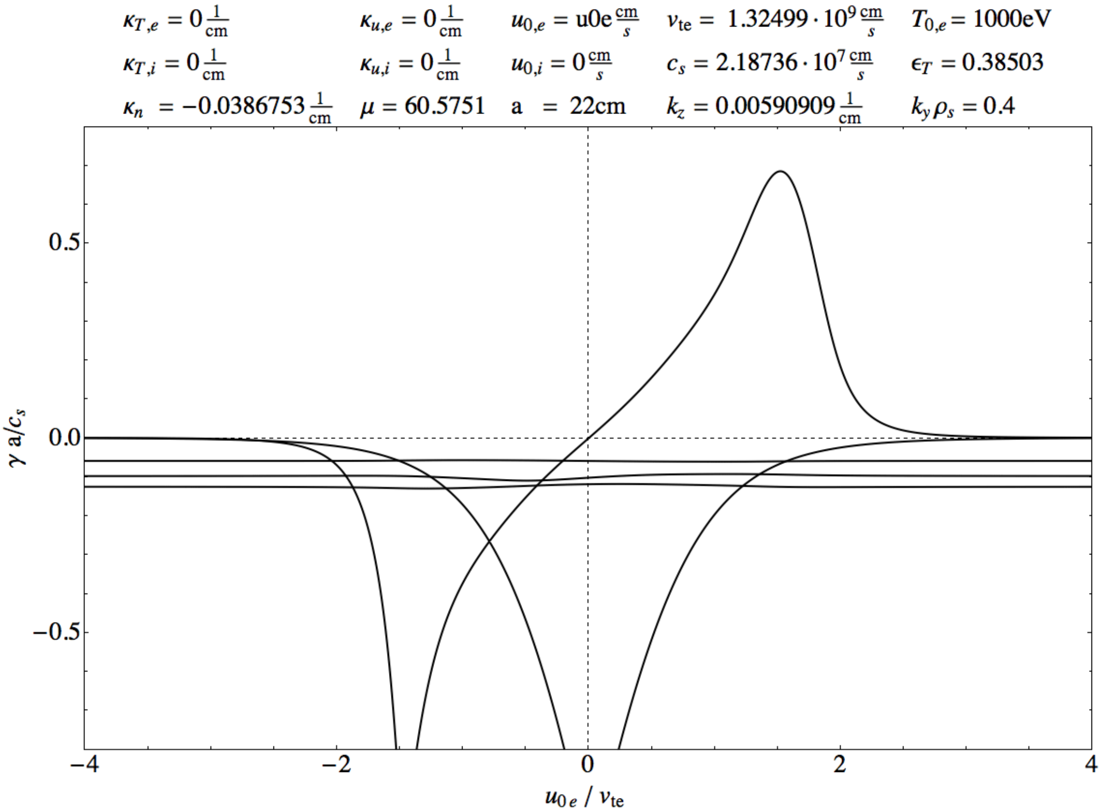

Figure A.13: Growth rate versus $u_{0,e}/v_{te}$ with $\eta_i = 0$, $\eta_e = 0$, $k_z a = 0.13$, $k_y \rho_s = 0.4$. - The only growing mode for this particular set of parameters belongs to the current-driven drift wave.

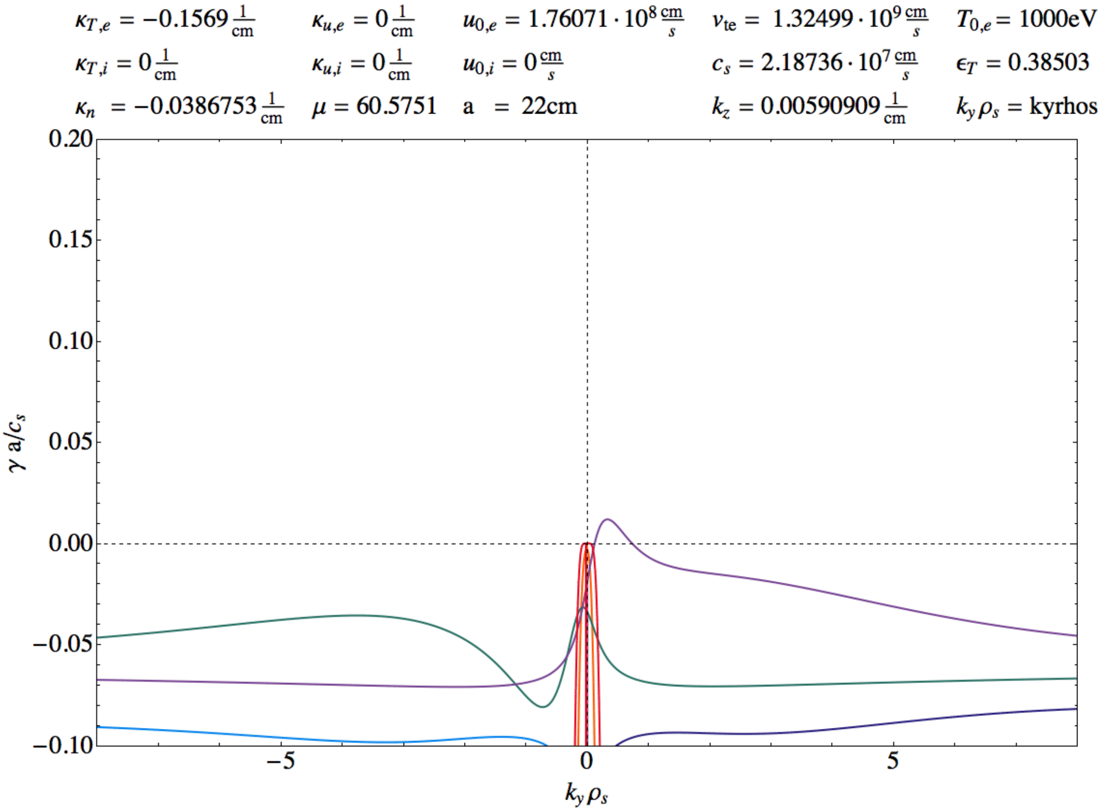

Figure A.14: Growth rate versus $k_y\rho_s$ with $\eta_i = 0$, $\eta_e \approx 4.06$, $u_{0,e} \approx 8c_s$. - This figure corresponds to figure 5.13, extended to negative $k_y\rho_s$.

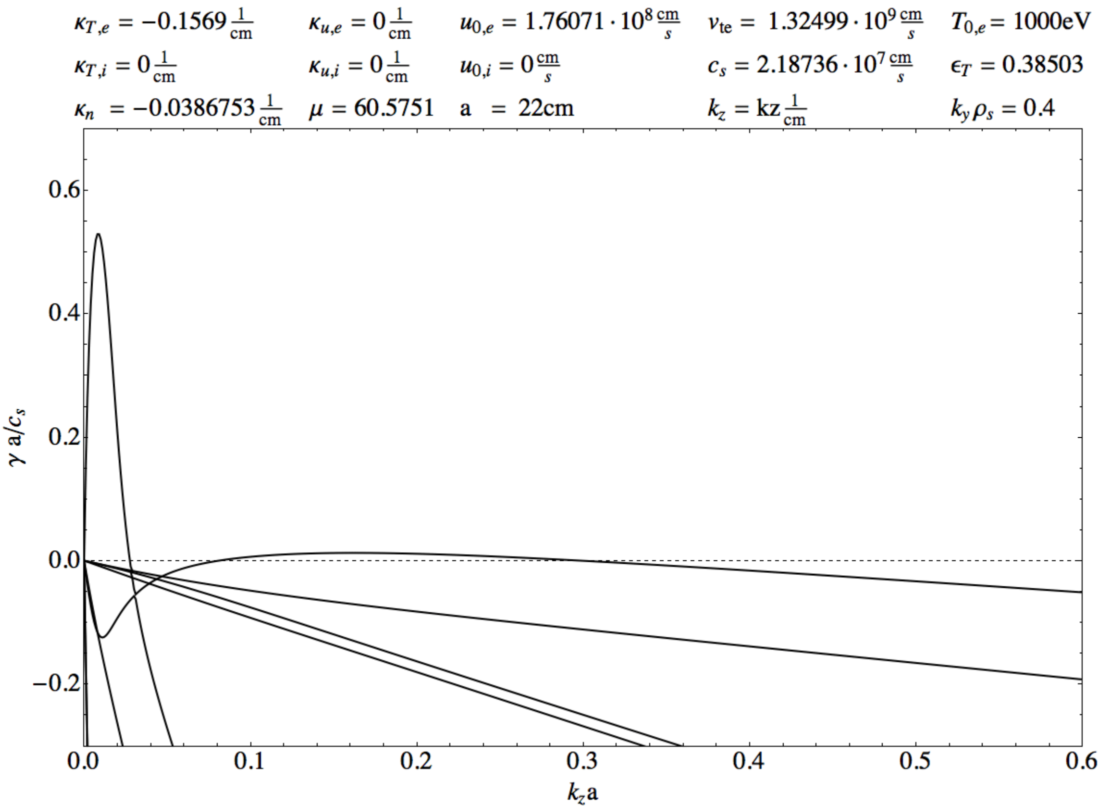

Figure A.15: Growth rate versus $k_z a$ with $\eta_i = 0$, $\eta_e \approx 4.06$, $u_{0,e} \approx 8c_s$. - This figure illustrates the parallel wave number direction corresponding to figures 5.13 and A.14, that show the growth rate against the perpendicular wave number direction.

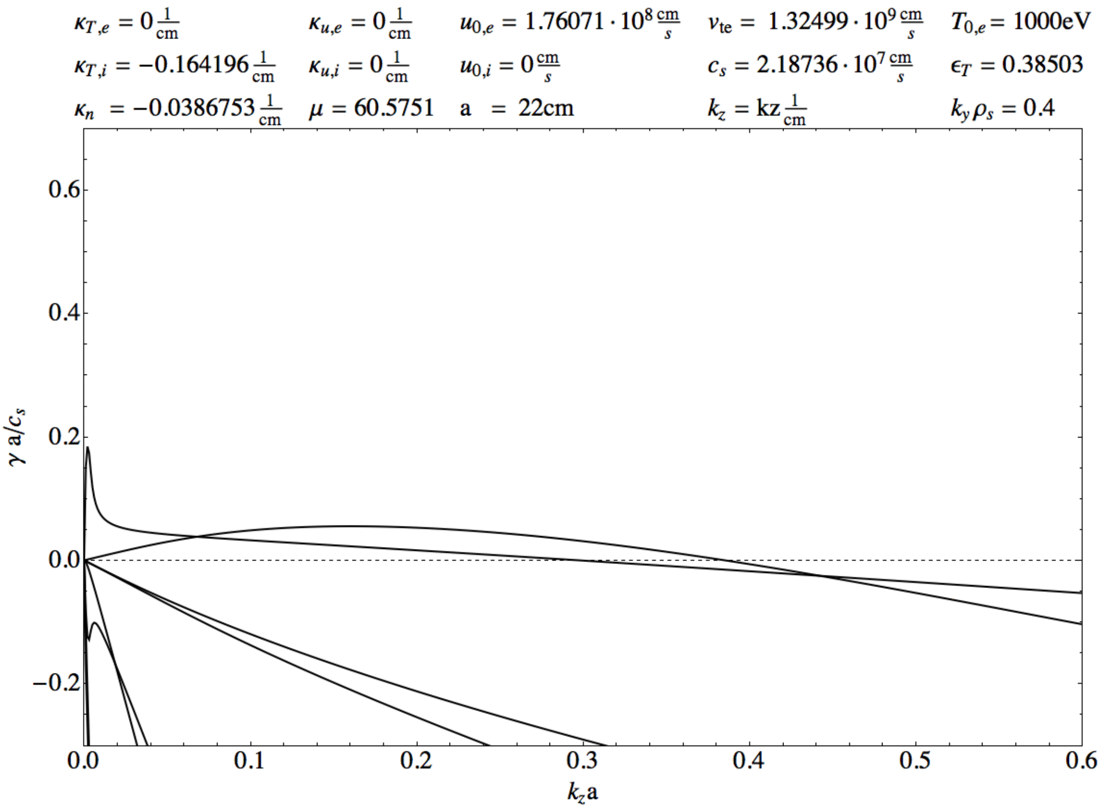

Figure A.16: Growth rate versus $k_z a$ with $\eta_i \approx 4.25$, $\eta_e = 0$, $u_{0,e} \approx 8c_s$. - Without the damping effects of the electron temperature gradient, the current-driven drift wave becomes significant for a specific parameter regime. This figure corresponds to figure 5.14 that illustrates the perpendicular wavenumber direction.

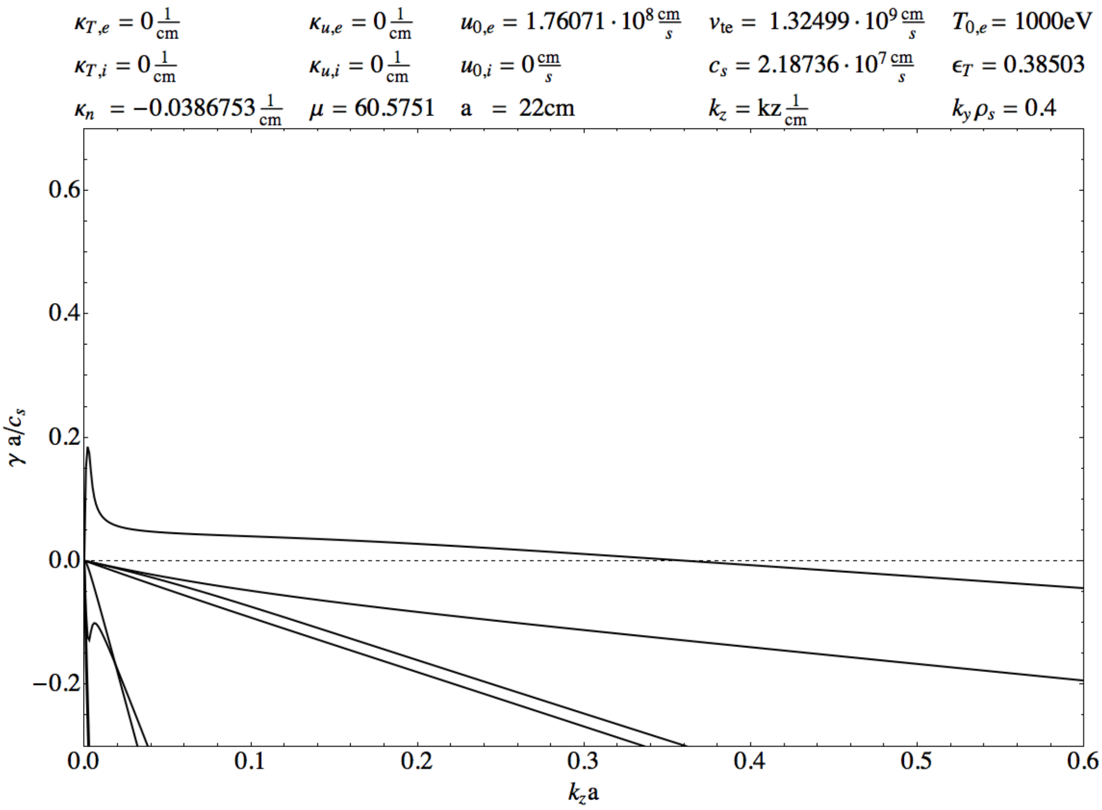

Figure A.17: Growth rate versus $k_z a$ with $\eta_i = 0$, $\eta_e = 0$, $u_{0,e} \approx 8c_s$. - The current-driven drift wave can be unstable at $k_z > 0$ for $k_y \rho_s = 0.4$ and positive electron currents. Figure 5.16 shows the the same mode in perpendicular wave number direction.

Appendix B

Diffusion Studies

The following figures supplement the diffusion studies of chapter 4. Plots of the mixing-length diffusivity versus other variables and in other ranges are provided.

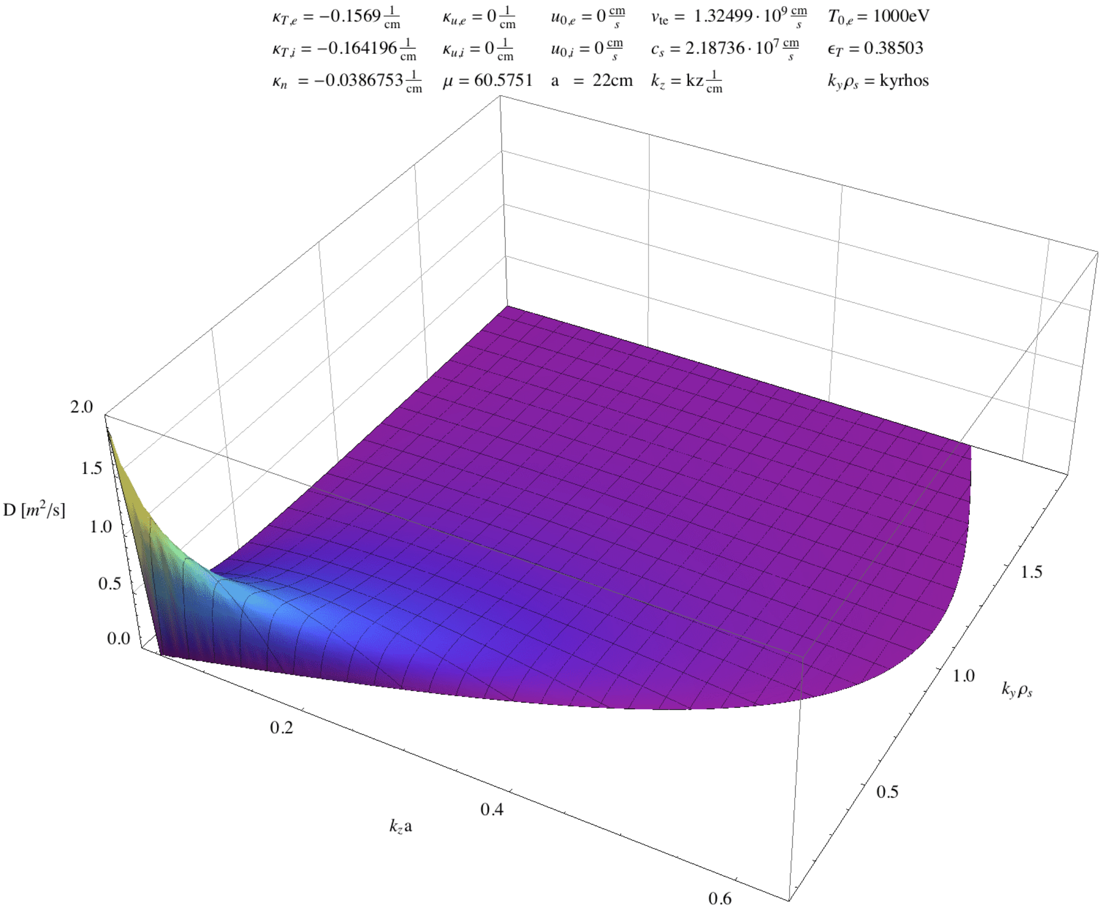

Figure B.1: Diffusivity versus $k_z a$ and $k_y \rho_s$ with $\eta_i \approx 4.25$, $\eta_e \approx 4.06$, $u_{0,e} = 0$. - Figure 5.19 shows a detail of this plot.

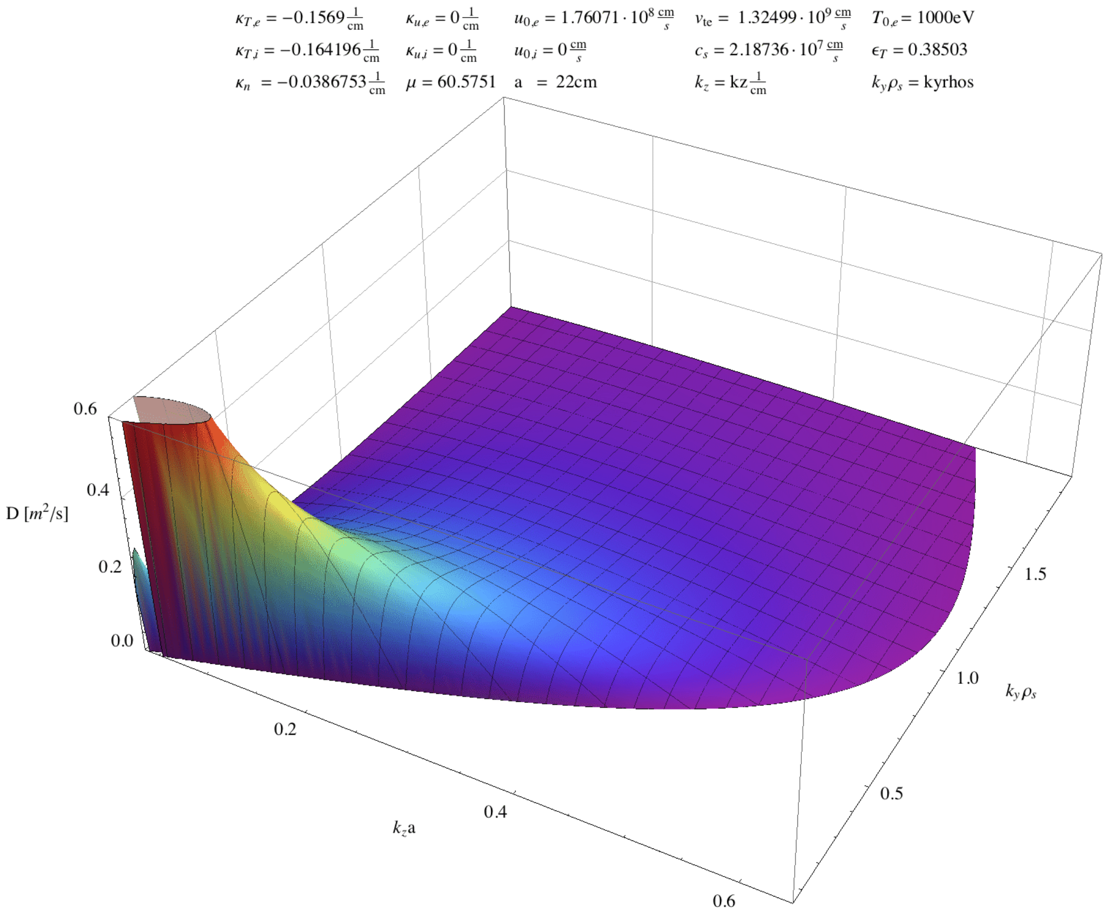

Figure B.2: Diffusivity versus $k_z a$ and $k_y \rho_s$ with $\eta_i \approx 4.25$, $\eta_e \approx 4.06$, $u_{0,e} \approx 8c_s$. - With an additional positive electron current of $u_{0,e} \approx 8c_s$, two ridges are observable. The higher one is caused by the ion temperature gradient instability, which is visible in figure B.1, and the other diffusivity ridge (visible at low k_z) is generated by the current-driven drift wave.

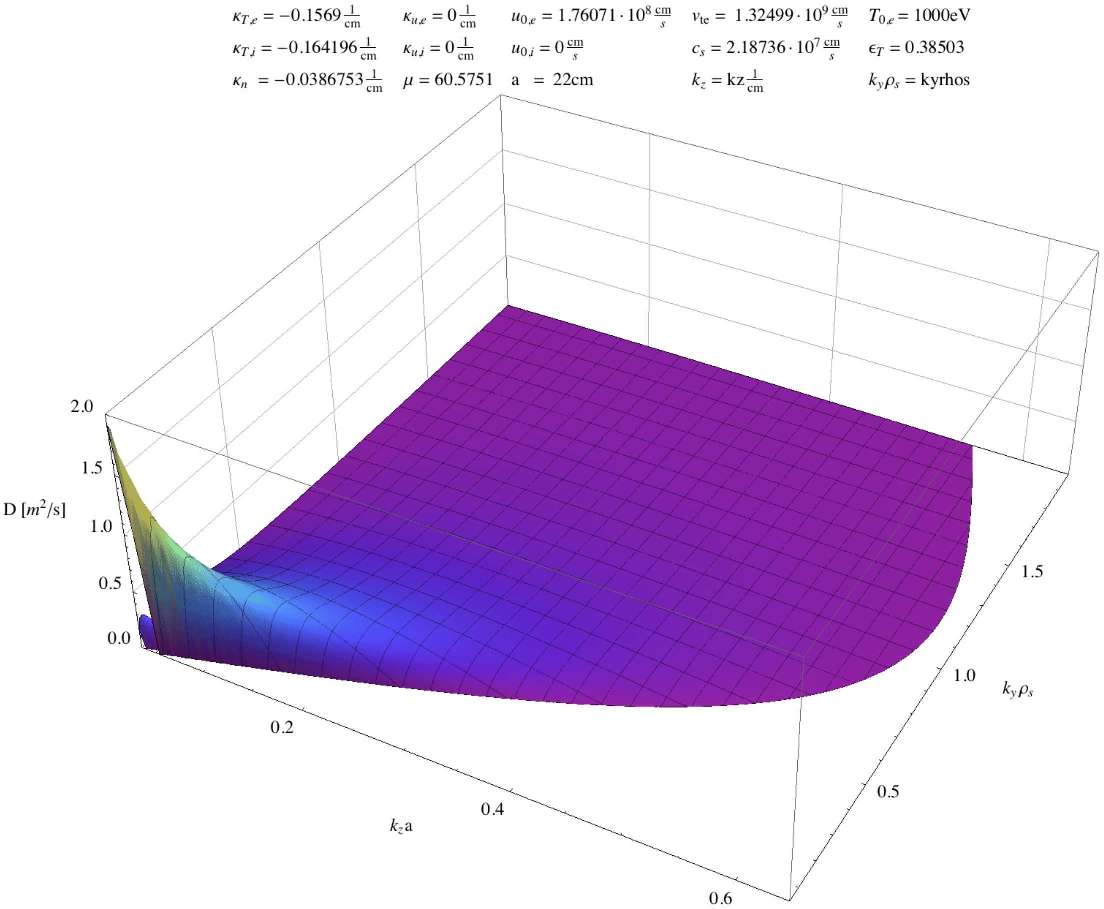

Figure B.3: Diffusivity versus $k_z a$ and $k_y \rho_s$ with $\eta_i \approx 4.25$, $\eta_e \approx 4.06$, $u_{0,e} \approx 8c_s$. - The higher maximum is caused by the ion temperature gradient instability, which is visible in figure B.1, and the other diffusivity ridge (visible at low k_z) is generated by the current-driven drift wave. A detail of this plot is depicted in figure B.2.

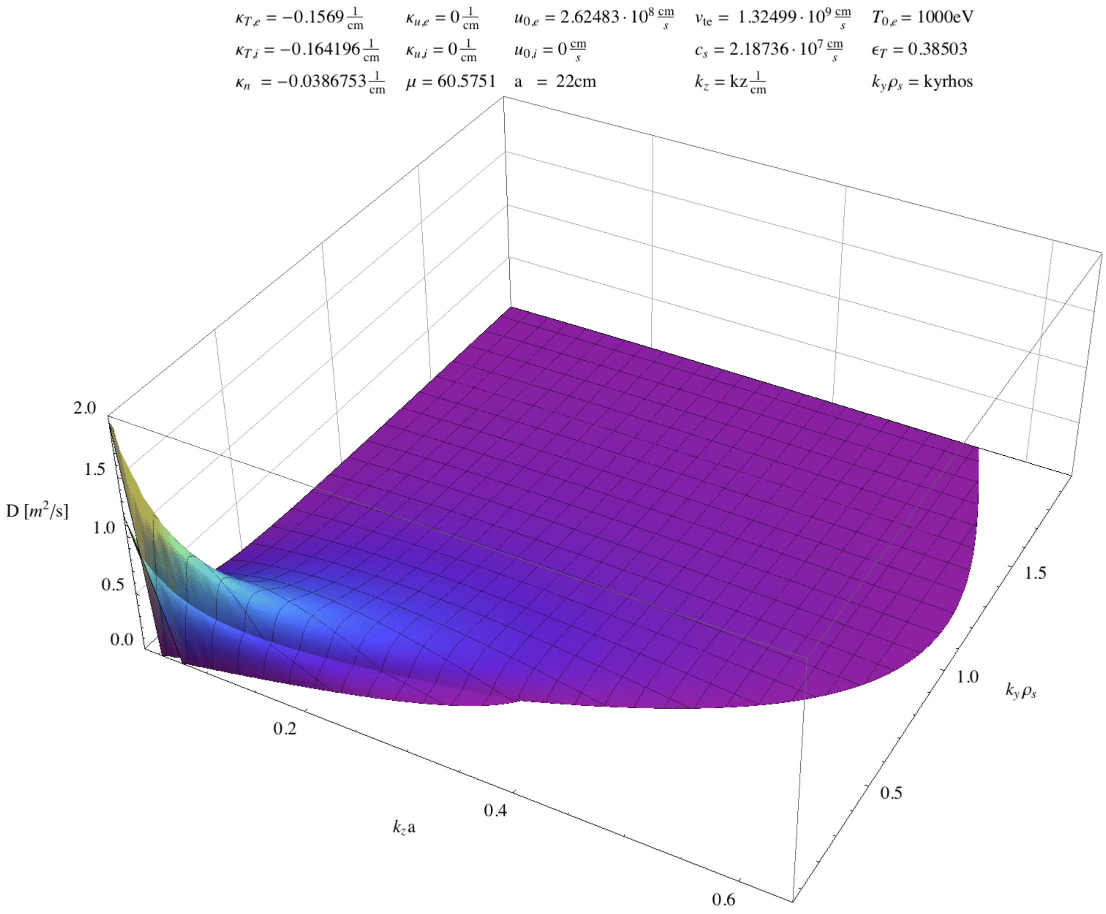

Figure B.4: Diffusivity versus k_za and $k_y\rho_s$ with $\eta_i \approx 4.25$, $\eta_e \approx 4.06$, $u_{0,e} \approx 12c_s$. - The three-dimensional view shows the two ridges, one resulting from the η_i-mode and the other one driven by the electron drift current. Figure B.1, which has the same parameters but no electron current, shows the temperature-gradient driven diffusion separately. A detail of this plot is illustrated in figure 5.24.

Declaration

I herewith declare that I have produced this paper without the prohibited assistance of third parties and without making use of aids other than those specified; notions taken over directly or indirectly from other sources have been identified as such. This paper has not previously been presented in identical or similar form to any other German or foreign examination board.

The thesis work was conducted from 02/2011 to 01/2012 under the supervision of Prof. Gregory W. Hammett at Princeton Plasma Physics Laboratory.

Nadine Kremer

Princeton, January 2012